

Electrochemical Development of Cathode for Metal Supported-Solid Oxide Fuel Cells

by

Abdallahman FayeZ Alharbi

A thesis
presented to the University of Waterloo
in fulfillment of the
thesis requirement for the degree of
Master of Applied Science
in
Chemical Engineering

Waterloo, Ontario, Canada, 2020

©Abdallahman FayeZ Alharbi 2020

AUTHORS DECLARATION

I hereby declare that I am the sole author of this thesis. This is a true copy of the thesis, including any required final revisions, as accepted by my examiners.

I understand that my thesis may be made electronically available to the public.

ABSTRACT

In comparison to conventional generation systems, the use of Solid Oxide Fuel Cells (SOFCs) provides higher electrical efficiency and lower carbon emissions. Furthermore, contrary to other fuel cell types, SOFC is considered fuel flexible as it can use a variety of fuels, such as hydrogen, alcohol, natural gas and other hydrocarbons or syngas. Nevertheless, SOFCs is expensive in terms of fabrication cost, as it is made essentially of advanced ceramic materials because of its high operating temperature (600-900°C). Much effort has been devoted to reduce cost, one possibility being the use of metal-supported solid oxide fuel cell (MS-SOFC). Cost reduction with MS-SOFC takes place because cheaper metal materials can replace some ceramic ones. Indeed, in MS-SOFC, the supporting structure is made of porous metal, on which are deposited thin ceramic layers for the anode, electrolyte and cathode. In traditional SOFC, one of those ceramic layers (typically the anode) is made thicker to support the whole assembly. Besides cost, there are other important advantages in using MS-SOFCs as they possess high oxidation resistance, mechanical stability and tolerance to redox cycles. On the other hand, there are important challenges in the fabrication of MS-SOFC as very high temperatures are involved to make dense electrolyte, which normally is done in air, but not in the present case to avoid extensive oxidation of the metal at those high temperatures (above 1200°C). Another constraint is that the coefficient of thermal expansion (CTE) of the porous metal support must match the CTE of the ceramic materials, such as yttrium stabilized zirconia (YSZ), typically used as electrolyte. The fabrication method considered in this work is tape casting of different layers followed by co-sintering (under reducing atmosphere). In this thesis, SS-430 L and YSZ have been used as metal support and electrolyte, respectively. However, the main focus of this study is on the cathode, for which two different types of cathode material/preparation were considered: 1) ex-situ sintering of a printed stand-alone cathode layer and 2) infiltration of cathode materials on a cathode scaffold. For the first type, $\text{La}_{0.58}\text{Sr}_{0.4}\text{Co}_{0.2}\text{Fe}_{0.8}\text{O}_{3-\delta}$ mixed with Gadolinium Doped Ceria (LSFC-GDC) was used as cathode materials. For the second type, Samarium Barium Strontium Cobalt oxide (SBSCo) was infiltrated in the cathode scaffold. Cell performance was evaluated through IV curve, power density, and electrochemical impedance spectroscopy. The cell with printed stand-alone cathode showed very poor

performance in terms of Maximum Power Density (MPD) (less than 5 mW/cm²), associated with very high polarization resistance. In comparison with printed stand-alone cathode structure, the cell with the cathode scaffold showed much better performance in terms of Maximum Power Density (MPD) (140 mW/cm²) , but more tuning is still required to make it comparable to state-of-the-art SOFC.

Acknowledgments

First, I would like to thank Allah (The God) for his limitless help and guidance for giving an me Waterloo of University the at student a be to opportunity. Thereafter, I would like to thank all the possible thesis this made who people.

First, I would like to thank my supervisor (Professor Eric Croiset) my complete to me helped who guidance and advice me giving by thesis. Then, Dr. who Toor Sannantaught me a lot about SOFC materials and how to prepare cells, and with whom I had many fruitful discussions. Furthermore, I would like to thank Professor Mark Pritzker who taught me about electrochemistry. Then, I would like to thank my parents and my wife who fully supported study my throughout me. would also I their shared who colleagues and friends my thank to likeknowledge with me and constantly encouraged me.

Finally, I would like to sincerely thank my employer Corporation Conversion Water Saline(SWCC) and Cultural Arabian Saudi administrator scholarship myBureau (SACB) in Canada for giving me a chance to pursue my Master's degree by fully funding me during my study.

Table of Contents

AUTHORS DECLARATION.....	ii
ABSTRACT	iii
Acknowledgments.....	v
List of Figures	x
List of Tables	xvii
Nomenclature.....	xix
Chapter 1 Introduction.....	1
1.1 Fundamental of Fuel Cells	2
1.1.1 Working Principle of a Fuel Cell.....	2
1.1.2 Types of Fuel Cell.....	7
1.2 Basics of Solid Oxide Fuel Cells and its Application	9
1.3 Challenges	12
1.4 Thesis Organization	17
Chapter 2 Literature Review	18
2.1 Metal Supported Solid Oxide Fuel Cells	18
2.2 The Selection of Metal Supported Cell Materials	19
2.2.1 The Choice of Metal Support	19
2.2.2 Choice of Anode Materials	23

2.2.3 The Choice of Electrolyte	33
2.2.3.1 Yttria Stabilized Zirconia (YSZ).....	34
2.2.3.2 Doped Ceria.....	36
2.2.3.3 Scandia Yttria Stabilized Zirconia (ScYSZ).....	38
2.2.3.4 Strontium-and Magnesium Doped Lanthanum Gallate (LSGM).....	38
2.2.4 The Choice of Cathode.....	38
2.2.4.1 Cathode Sintering.....	40
2.2.4.1.1 In-Situ Sintering.....	41
2.2.4.1.2 Ex-Situ Sintering.....	42
2.2.4.2 Cathode Infiltration.....	43
Chapter 3 Experimental Methodology and Equipment	48
3.1 Experimental Approach, and Devices and Methods Used for MS-SOFC.....	48
3.1.1 Tape Caster.....	49
3.1.2 Co-Sintering	50
3.1.3 X-ray Diffraction.....	50
3.1.4 Scanning Electron Microscopy.....	51
3.1.5 Electrochemical Testing.....	51
3.1.5.1 Assembly for MS-SOFCs.....	51
3.1.5.2 Electrochemical Impedance Spectroscopy.....	54
3.2 Experimental Procedure.....	56

3.2.1 Selection of Half MS-SOFC Materials.....	57
3.2.2 Configurations of Half-cell Structures.....	57
3.2.3 Slurry Preparation for Tape Casting of Half MS-SOFC.....	58
3.2.3.1 Slurry for Metal Supported Layer.....	58
3.2.3.2 Slurry for Ceramic Layers.....	59
3.2.4 Tape Casting and Co-Sintering Procedure for Half MS-SOFC Cell.....	61
3.2.4.1 Tape Casting.....	61
3.2.4.2 Co-Sintering.....	62
3.2.5 Anode and Cathode Infiltration Procedures.....	63
3.2.5.1 Anode Infiltration.....	63
3.2.5.2 Cathode Infiltration.....	65
3.2.6 Cathode Deposition and Ex-Situ Sintering for Deposition Cathode.....	66
Chapter 4 Results and Discussion	68
4.1 Fabrication and Performance of MS-SOFC with Stand-alone Cathode Layer.....	69
4.1.1 Fabrication of full MS-SOFC Cell with Stand- alone Cathode Layer.....	69
4.1.2 Electrochemical Performance of full MS-SOFC Cell with Stand Alone Cathode Layer	72
4.2 Fabrication and Performance of MS-SOFC with Cathode Scaffold Layer.....	79
4.2.1 Fabrication of full MS-SOFC Cell with Cathode Scaffold Layer.....	79
4.2.2 Electrochemical Performance of full MS-SOFC Cell with Cathode Scaffold.....	82

Chapter 5 Conclusion and Recommendations.....	92
5.1 Conclusions.....	92
5.2 Recommendations.....	93
5.2.1 For Porous Cathode Scaffold Structure.....	93
5.2.2 For Stand Alone Cathode Structure.....	93
References	94
APPENDIX.....	110
Air, Argon and Hydrogen Calibration used in this study	110

List of Figures

Figure 1.1: Ideal and Actual Fuel Cell Voltage/Current Characteristics [5]	6
Figure 1.2: Schematic of a Solid Oxide Fuel Cell.....	10
Figure 1.3: The Co-generation system [14]	11
Figure 1.4: Material limitation for SOFC [8].....	12
Figure 1.5: SEM BSE image of a large vertical electrolyte crack in a fresh fractured anode-supported SOFC after redox cycling [36].....	13
Figure 1.6: Schematic Diagram of Different SOFC Configurations [12].....	14
Figure 2.1: Schematic Phase Diagram for Cr-Ni-Fe System [64].....	20
Figure 2.2: EDAX/SEM composite image of cross-section of MS-SOFC produced by plasma spray processing after 1500 H operation at 800°C (Left: Ni distribution in red, Right: Fe distribution in blue) [60].....	24
Figure 2.3: Electrolyte and anode microstructure of (a) Cell sintered at 1400°C in H ₂ and (b) Cell sintered at high temperature in air and then reduced at 800°C in H ₂ . [1,85].....	25
Figure 2.4: (a) Microstructure of the cell fabricated at LBNL by cosintering before the catalyst infiltration, and the microstructure of anode after Ni infiltration (b)once and (c)5 times [41,86].....	25
Figure 2.5: Impedance spectra of the single MS-SOFC before and after the 12h measurement at 750°C [51].....	26

Figure 2.6: Current-voltage and current-power characteristics of a single metal- supported cell employing a Ni/GDC cermet anode[91].....	27
Figure 2.7: SEM images of the a MS-SOFC, b LSFSc-YSZ cathode, c Ni-430L anode [95].....	28
Figure 2.8: I–P–V characteristics for MS-SOFC [95].....	28
Figure 2.9: Impedance spectra at open circuits for MS-SOFC [95].....	29
Figure 2.10: Electrochemical characteristics of the single cell measured at 650–800°C: a I–P–V characteristics, b Impedance spectra [96].....	29
Figure 2.11: Stability of the single cell with used infiltrated SDC-430L as anode catalyst measured at 650°C [12]	30
Figure 2.12: I-P-V characteristics for infiltrated Ni-SDC-430L used in MS-SOFC [96]....	30
Figure 2.13: Impedance spectra for infiltrated Ni-SDC-430L used in MS-SOFC [95].....	31
Figure 2.14: SEM image of MS-SOFC with Ni-SDC as the functional anode. (ao) before cell operation and (a1) picture after cell operation of 175 hours at 700°C [98].	31
Figure 2.15: (a) Polarization curves and (b) Electrochemical impedance spectra of the Ru:GDC and the Ni:GDC infiltrated MS-SOFCs [102].	32
Figure 2.16: Open circuit voltage (OCV) and the power density (p) of different generations of cells tested under redox cycling Generation1 Generation 2 Generation3 [43]	35
Figure 2.17: Performance of MS-SOFC with YSZ electrolyte obtained by co-sintering [86]	36
Figure 2.18: Theoretical open circuit voltage (Eth) and measured open circuit voltage V OCV over 450–600°C [123].	37
Figure 2.19: comparison of OCV of cells with bi-layered ScSZ-SDC as electrolyte (OCV1) and cell with only SDC as electrolyte (OCV2); b) comparison of MPD of cell with bi-layered ScSZ-SDC as electrolyte (MPD1) and cell with just SDC as electrolyte (MPD2) [117]......	38

Figure 2.20: ASRs of in-situ SBSCO cathode measured at various temperatures (650, 700 and 750°C) over 1000 hours[134].....	41
Figure 2.21: I/V-curves and resulting power density of an MSC with ex-situ sintered LSCF cathode at different operating temperature [141].....	43
Figure 2.22: the polarization resistance for different loading percentage of infiltrated LSFSc [97].....	44
Figure 2.23: Polarization of LSC-SSZ, LSCF-SSZ and SBSC-SSZ at 700°C [145].....	44
Figure 2.24: I-P-V characteristics, b Impedance spectra at different operating temperature from 550 to 700°C [148].....	45
Figure 3.1 : Tape caster and doctor blade	49
Figure 3.2 : SOFC Testing Station.....	52
Figure 3.3: The test assembly with gas manifold inside the fumehood.....	53
Figure3.4: (A) Nyquist diagram and (B) Bode diagram of a SOFC [11,157,158].....	55
Figure 3.5 : Equivalent circuit used in the present work	56
Figure 3.6 : Cell structure 1: Stand-alone cathode layer. Cell structure 2: Porous infiltrated cathode scaffold.....	58
Figure 3.7 : Scavenger, counter weight and thermo block.....	62
Figure 3.8: A schematic of the Ni-SDC anode fabricated through infiltration.....	65

Figure 4.1 : Figure 4.1: (a) Cell structure 1: Stand-alone cathode layer. (b) Cell structure 2: Porous infiltrated cathode scaffold.....	68
Figure 4.2 – SEM micrograph of fresh structure 1 cell, with cathode transition.....	71
Figure 4.3: Polarization and power density for a cell with cathode stand-alone layer. 50% H ₂ (balance Argon), Cell temperature ~800°C (furnace temperature of 750°C). With cathode transition layer.....	72
Figure 4.4 – Spent cell with cathode stand-alone layer. 50% H ₂ (balance argon), cell temperature ~800°C (furnace temperature of 750°C). With cathode transition layer. a) SEM micrograph; b) EDX results for the region indicated by the red square in a).....	73
Figure 4.5: Polarization and power density for a cell with cathode stand-alone layer. 40% H ₂ (balance Argon), Cell temperature ~784°C (furnace temperature of 750°C). Without cathode transition layer.....	74
Figure 4.6: Nyquist plot a cell with cathode stand-alone layer. 50% H ₂ (balance Argon), Cell temperature ~784°C (furnace temperature of 750°C). Without cathode transition layer.....	74
Figure 4.7: Polarization and power density plot for a cell with cathode stand-alone layer. 33% H ₂ (balance Argon), Cell temperature ~773°C (furnace temperature of 750°C). Without cathode transition layer. New cathode sintering profile.....	75
Figure 4.8: Nyquist plot a cell with cathode stand-alone layer. 33% H ₂ (balance Argon), Cell temperature ~773°C (furnace temperature of 750°C). Without cathode transition layer. New cathode sintering profile.....	76

Figure 4.9 – SEM micrograph for cell with cathode stand-alone layer. 33% H₂ (balance argon), cell temperature ~773°C (furnace temperature of 750°C). Without cathode transition layer. New cathode sintering profile.....76

Figure 4.10: Polarization and power density plot for a cell with cathode stand-alone layer. 38% H₂ (balance Argon), Cell temperature ~773°C (furnace temperature of 750°C). With cathode transition layer and new cathode sintering profile.....76

Figure 4.11: Nyquist plot a cell with cathode stand-alone layer. 38% H₂ (balance Argon), Cell temperature ~773°C (furnace temperature of 750°C). With cathode transition layer and new cathode sintering profile.....77

Figure 4.12 – Additional stand-alone cathode layer cell structures; a) more graded MS layer to anode transition layer, b) Cell co-sintered for 5 hours, c) Cell co-sintered for 4 hours....
.....78

Figure 4.13 – SEM micrograph of fresh cell with cathode scaffold (structure 2).....81

Figure 4.14 – EDX results for a) electrolyte region; b) cathode scaffold region; c) anode transition region.....82

Figure 4.15: Polarization and power density plot for a cell with cathode scaffold. 40% H₂ (balance Argon), Cell temperature ~773°C (furnace temperature of 750°C). Cell according to cell 2 in Table2.1.....83

Figure 4.16: Nyquist plot a cell with cathode scaffold. 40% H₂ (balance Argon), Cell temperature ~773°C (furnace temperature of 750°C). Cathode scaffold made of porous YSZ (according to Cell 2 in Table2.1).....83

Figure 4.17 – SEM micrograph for spent cell with cathode scaffold. 40% H₂ (balance argon), cell temperature ~775°C (furnace temperature of 750°C). Cathode scaffold made of porous YSZ (according to Cell 2 in Table 2.1).....84

Figure 4.18 – Picture of cell with cathode scaffold with different amounts of SDC after co-sintering; a) 50% SDC/50% YSZ with infiltrated cathode, b) 10% SDC/90% YSZ with infiltrated cathode, and c) 5% SDC/95% YSZ after co-sintering.....82

Figure 4.19 – Polarization and power density plot for a cell with cathode scaffold. 38% H₂ (balance Argon), Cell temperature ~774°C (furnace temperature of 750°C). Cathode scaffold made of porous 25%SDC/75%YSZ.....85

Figure 4.20 – Nyquist plot a cell with cathode scaffold. 38% H₂ (balance Argon), Cell temperature ~774°C (furnace temperature of 750°C). Cathode scaffold made of porous25%SDC/75%YSZ.....86

Figure 4.21 – Spent cell with cathode scaffold. 38% H₂ (balance argon), cell temperature ~774°C (furnace temperature of 750°C). Cathode scaffold made of porous 25%SDC/75%YSZ. a) SEM micrograph; b) EDX results for electrolyte region; c) EDX results for cathode scaffold region; d) EDX results for anode transition results.....88

Figure 4.22. Cell with prolonged sintering time; a) 4 hours sintering and 72.7wt% YSZ in electrolyte slurry, b) 5 hours sintering and 75wt% YSZ in electrolyte slurry.....89

Figure 4.23 – Polarization and power density plot for a cell with cathode scaffold. 29% H₂ (balance Argon), Cell temperature ~771°C (furnace temperature of 750°C). Cell according to cell 2 in Table 2.1, except sintered for 5 hours (and 75% YSZ in electrolyte slurry).....90

Figure 4.24 – Nyquist plot a cell with cathode scaffold. 29% H₂ (balance Argon), Cell temperature ~771°C (furnace temperature of 750°C). Cell according to cell 2 in Table 2.1, except sintered for 5 hours (and 75% YSZ in electrolyte slurry).....90

Figure 4.25 – SEM micrograph of the spent cell with cathode scaffold. 29% H₂ (balance argon), cell temperature ~771°C, sintered for 5 hours at 1325°C.....91

List of Tables

Table 1.1: The Overall Reactions for Fuel Cell Reactions and their Corresponding Nernst Equations [5].....	3
Table 1.2: Summary of Major Differences of the Fuel Cell Types [5,6].	8
Table 1.3: Advantages and disadvantages of a different SOFC configuration [12]	15
Table 2.1: The comparison between metal alloys [41,63]	20
Table 2.2: Components of stainless steels utilized in metal support for SOFC [32,66,67]....	21
Table 2.3: Thickness and leak rate values of different generations of plasma sprayed 8YSZ [43].....	35
Table 2.4: ASR for different LSCrM cathodes calculated using ASR plots at 900°C [6,139].....	40
Table 2.5: Brief summary of cathode literature review[49, 133, 136, 143,148]	46
Table 3.1 – Temperature profile to heat up the test setup to the desired temperature (here 750°C) and to cool down at the end of the experiment.....	54
Table 3.2 :. Composition of slurry for metal support	58
Table 3.3: Composition of the ceramic preliminary slurry	59
Table 3.4:. Base powder slurry for transition, porous layers and electrolyte layers	60
Table 3.5: The tape casting thickness of cell slurry.....	61
Table 3.6: Co-sintering temperature profile for half MS-SOFC.	63

Table 3.7: Anode composition used for anode infiltration	64
Table 3.8: Cathode solution composition and SBSCo composition.....	66
Table 3.9: Old ex-situ sintering temperature profile used for scan printed LSCF cathode on YSZ dense electrolyte.....	66
Table 3.10: New ex-situ sintering temperature profile used for scan printed LSCF cathode on YSZ dense electrolyte.....	67
Table 4.1: Resulting half-cell depending on different fabrication process parameters.....	70
Table 4.2: Resulting half-cell with cathode scaffold depending on different fabrication process parameters.....	80

Nomenclature

Roman Symbols

A	Surface Area (m^2)
C_B	Bulk concentration
C_C	Surface Concentration
D	Diffusion coefficient of the reacting species ($\text{m}^2 \cdot \text{s}$)
E°	Ideal standard potential (V)
E	Cell Potential (V)
E_r	Reversible Cell Potential (V)
E_a	Activation Energy (J/mol)
F	Faraday's Constant ($96487\text{C} \cdot \text{mol}^{-1}$)
ΔG	Change in Gibbs Free Energy ($\text{J} \cdot \text{mol}^{-1}$)
Δh	Enthalpy Change (J/mol)
I	Current (Amp)
I	Current Density ($\text{Amps} \cdot \text{cm}^{-2}$)
l	Sample thickness (cm)
n	Moles of electrons per mole of fuel
n_r	Second Law Efficiency
q	Heat generated or absorbed (J)
R_{ee}	Electrode-Electrolyte Interface Resistance (Ω)
R_{gb}	Grain Boundary Resistance (Ω)
R_{gi}	Grain Interior Resistance (Ω)
R_T	Total Resistance (Ω)
s	Entropy ($\text{J} \cdot \text{K}^{-1}$)
T	Temperature (K)
R	Gas constant ($8.314\text{J} \cdot \text{K}^{-1} \cdot \text{mol}^{-1}$)
P_{H_2}	Hydrogen partial pressure (Atm)

P_{H_2O}	Water partial pressure (Atm)
P_{O_2}	Oxygen partial pressure (Atm)
P_{CO_2}	Carbon dioxide partial pressure (Atm)
t	Time (min)
w	work done (J)
W_{max}	Maximum work done (J)
Z	Impedance (Ω)
$Re Z$	<i>Real</i> Impedance (Ω)
$Im Z$	Imaginary Impedance (Ω)

Greek Symbols

δ_s	Entropy Generated
δw	Work Done (J)
$\varphi_{c,r}$	Reversible Cathode Potential
$\varphi_{a,r}$	Reversible Anode Potential
φ_c	Cathode Potential
φ_a	Anode Polarization
δ	Thickness of the diffusion layer (cm)
σ	Total conductivity S/m
σ_o	Oxygen conductivity S/m
σ_e	Electron conductivity S/m

Abbreviations

AFC	Alkaline Fuel Cell
AFL	Anode Functional Layer
ASC	Anode Supported Cell

ASR	Area Specific Resistance
BSCF	$\text{Ba}_{0.5}\text{Sr}_{0.5}\text{Co}_{0.8}\text{Fe}_{0.2}\text{O}_{3-d}$
CGO	Cerium Gadolinium Oxide
CSC	Cathode Supported Cell
CTE	Co-efficient of Thermal Expansion
DBL	Diffusion Barrier Layer
DTU	Danish Technological University
EDS	Energy Dispersive X-Ray Spectroscopy
EIS	Electrical Impedance Spectroscopy
ESB	$(\text{Bi}_2\text{O}_3)_{0.7}(\text{Er}_2\text{O}_3)_{0.3} - \text{Ag}$
ESC	Electrolyte Supported Cell
FC	Fuel Cell
GDC	Gadolinium Doped Ceria
LBNL	Lawrence Berkeley National Laboratory
RO	Reverse Osmosis

GT	Standard gas turbine
HRSG	Heat recovery steam generator
MED	Multiple-effect distillation
LSGM	$\text{La}_{0.8}\text{Sr}_{0.2}\text{Ga}_{0.8}\text{Mg}_{0.2}\text{O}_{3-\delta}$
LSFNT	$\text{La}_{0.4}\text{Sr}_{0.4}\text{Fe}_{0.03}\text{Ni}_{0.03}\text{Ti}_{0.94}\text{O}_3$
LSFC	$\text{La}_{0.58}\text{Sr}_{0.4}\text{Co}_{0.2}\text{Fe}_{0.8}\text{O}_{3-\delta}$
LSCrM	$\text{La}_{0.8}\text{Sr}_{0.2}\text{Cr}_{1-x}\text{Mn}_x\text{O}_{3-\delta}$
LSCM	$\text{La}_{0.8}\text{Sr}_{0.2}\text{Co}_{1-x}\text{Mn}_x\text{O}_{3-\delta}$
LBSM	$(\text{La}_{0.74}\text{Bi}_{0.10}\text{Sr}_{0.16})\text{MnO}_3$
LSC	$(\text{La}_{0.6}\text{Sr}_{0.4})_{0.99}\text{CoO}_{3-\delta}$
MCFC	Molten Carbonate Fuel Cell
MIEC	Mixed Ionic Electronic Conductor
MSC	Maximum Power Density
MSC	Metal Supported Cell
MS-SOFC	Metal Supported-Solid Oxide Fuel Cell

PSD	Plasma Spray Deposition
PVD	Physical Vapor Deposition
PLD	Pulsed Laser Deposition
SEM	Scanning Electron Microscopy
SOFC	Solid Oxide Fuel Cell
SS	Stainless-Steel
TPB	Triple Phase Boundary
XRD	X-Ray Diffraction
SFMO	$\text{Sr}_2\text{Fe}_{1.5}\text{Mo}_{0.5}\text{O}_{6-d}$
SBSC50	$\text{SmBa}_{0.5}\text{Sr}_{0.5}\text{Co}_{2.0}\text{O}_{5+d}$
PEM-FC	Polymer Electrolyte Membrane-Fuel Cell
OCV	Open Circuit Voltage
SSZ	$(\text{ZrO}_2)_{0.89}(\text{Sc}_2\text{O}_3)_{0.1}(\text{CeO}_2)_{0.01}$

SSC	$\text{Sm}_{0.5}\text{Sr}_{0.5}\text{CoO}_3$
(PrO _x)	Praseo-Dymium Oxide
LSFSc	$\text{La}_{0.6}\text{Sr}_{0.4}\text{Fe}_{0.9}\text{Sc}_{0.1}\text{O}_{3-\delta}$

Chapter 1 Introduction

In the past century, electric power has been generated by combustion of fossil fuel which presents some disadvantages, for example low conversion efficiency, and emission of greenhouse gasses [1]. The demand for electric power has also considerably increased from 9,886 to 26,642 TWh between 1985 and 2018, that is an increase of 169% [2]. This demand has been mostly catered for by the use of thermal power generation, which inherently has a low efficiency, the mean efficiency value of conventional thermal power generation plant being 41% (LHV) worldwide [3]. It is worth mentioning that since 2001 every year has marked a high in Earth surface temperature compared to last 138 years [4].

Because of the issues mentioned above, global research is being driven into the development of green energy technologies which also exhibit higher efficiencies. One such technology of interest is fuel cells known for their greener nature and higher inherent efficiency than conventional thermal power units. In these devices chemical energy of a fuel is directly converted to electrical energy, bypassing energy conversion losses associated with thermal power generation.

There are several types of fuel cells and one of the most commercialized types suffer from fuel inflexibility. For instance, in the case of Proton Exchange Membrane – Fuel Cells (PEM-FCs) the fuel is hydrogen gas. A transition to using this type of FC requires planning and development of hydrogen infrastructure. However, Solid Oxide Fuel Cells (SOFCs), another type, is promising in terms of fuel flexibility, as it can operate not only with hydrogen, but also with renewable natural gas and biogas. In addition, internal reforming can occur when SOFCs is used as fuel cell devices, thus opening the possibility of internal reforming of more practical carbon containing fuels.

Another feature is operation at high temperature which increases the efficiency of the fuel cell unit (55%) [6]. These benefits have made SOFCs a prime candidate for research and development.

1.1 Fundamentals of Fuel Cells

The premise of fuel cells (FC) technology is to convert chemical energy of fuel directly to electrical energy using electrochemical charge transfer reactions and conduction of electrons through an external circuit. This inherently makes FCs more efficient than thermal power generation technologies. Primary FC technologies are:

1. Proton Exchange Membrane Fuel Cell (PEM-FC).
2. Alkaline Fuel Cell (AFC).
3. Direct Methanol Fuel Cell (DMFC).
4. Phosphoric Acid Fuel Cell (PAFC).
5. Molten Carbonate Fuel Cell (MCFC).
6. Solid Oxide Fuel Cell (SOFC).

A fuel cell consists of three main parts which are anode, electrolyte, and cathode. All of them have particular functions; the anode and cathode facilitate electrochemical oxidation and reduction of fuel and oxidant, respectively, and the electrolyte transports charges, in the form of ions between anode and cathode. The type of charge transported through the electrolyte depends on the type of FC. Since there are no energy transformation steps the FC is inherently more efficient than thermal power generation devices.

1.1.1 Working Principle of a Fuel Cell

As mentioned earlier the anode and cathode are responsible for the oxidation and reduction reactions, respectively. Reactions taking place at the two electrodes are termed half-cell reactions and the combination of them provide the overall fuel cell reaction. Fuel cells with their associated half-cell reactions are listed in Table 1.1 below.

Table 1.1: Overall Reactions for fuel cell reactions and their corresponding Nernst equation [5]

Fuel Cell	Anode Reaction	Cathode Reaction	Cell Reactions	Nernst Equation
Polymer Electrolyte and Phosphoric Acid	$H_2 \rightarrow 2H^+ + 2e^-$	$1/2O_2 + 2H^+ + 2e^- \rightarrow H_2O$	$H_2 + 1/2O_2 \rightarrow H_2O$	$E = E^0 + (RT/2F) \ln [P_{H_2}/P_{H_2O}] + (RT/2F) \ln [P_{O_2}^{1/2}]$
Alkaline	$H_2 + 2OH^- \rightarrow 2H_2O + 2e^-$	$1/2O_2 + H_2O + 2e^- \rightarrow 2(OH)^-$	$H_2 + 1/2O_2 \rightarrow H_2O$	$E = E^0 + (RT/2F) \ln [P_{H_2}/P_{H_2O}] + (RT/2F) \ln [P_{O_2}^{1/2}]$
Molten Carbonate	$H_2 + CO_3^{2-} \rightarrow 2H_2O + 2CO + CO_3^{2-} \rightarrow 2CO_2 + 2e^-$	$1/2O_2 + CO_2 + 2e^- \rightarrow CO_3^{2-}$	$CO + 1/2O_2 \rightarrow CO_2$ $H_2 + 1/2O_2 \rightarrow H_2O$	$E = E^0 + (RT/2F) \ln [P_{CO}/P_{CO_2}] + (RT/2F) \ln [P_{O_2}^{1/2}]$ $E = E^0 + (RT/2F) \ln [P_{H_2}/P_{H_2O}] + (RT/2F) \ln [P_{O_2}^{1/2}]$
Solid Oxide	$H_2 + O^{2-} \rightarrow H_2O + 2e^-$ $CO + O^{2-} \rightarrow CO_2 + 2e^-$ $CH_4 + 4O^{2-} \rightarrow 2H_2O + CO_2 + 8e^-$	$1/2O_2 + 2e^- \rightarrow O^{2-}$	$CH_4 + 2O_2 \rightarrow 2H_2O + CO_2$ $H_2 + 1/2O_2 \rightarrow H_2O$ $CO + 1/2O_2 \rightarrow CO_2$	$E = E^0 + (RT/8F) \ln [P_{CH_4}/P_{H_2O}^2 P_{CO_2}] + (RT/8F) \ln [P_{O_2}^2]$ $E = E^0 + (RT/2F) \ln [P_{H_2}/P_{H_2O}] + (RT/2F) \ln [P_{O_2}^{1/2}]$ $E = E^0 + (RT/2F) \ln [P_{CO}/P_{CO_2}] + (RT/2F) \ln [P_{O_2}^{1/2}]$

Note:

CO_3^{2-} - carbonate ion H_2 - hydrogen OH^- - hydroxyl ion

CO - carbon monoxide e^- - electron H_2O - water

CO_2 - carbon dioxide H^+ - hydrogen ion O_2 - oxygen

The above equations, known as Nernst equation, give a relationship between the ideal standard potential (E^0) and the ideal equilibrium potential (E) at different temperatures and different partial pressures of reactants and product.

Different FCs operate at different temperatures which is dependent on the electrolyte conduction and catalyst activity. SOFCs have a normal operating temperature range of 600-900°C. The performance of a FC is dependent on the kinetics and thermodynamic principles governing that

particular cell.

An important metric, the maximum available work, can be calculated from the first and second law of thermodynamics. Essentially, the Gibbs free energy can be used as the available work which is dependent on the heat absorbed or generated (q) and work done by the system (δw), as defined in Equations 1.1 and 1.2.

$$q = T \Delta S - T \delta s \quad (1.1)$$

$$\delta w = -\Delta G - T \delta s \quad (1.2)$$

where T is the absolute temperature of the system, ΔS is change of the entropy of the system, δs is the irreversible change of entropy, and ΔG is the change in Gibbs free energy. If the generation of entropy is equal to zero, the maximum electrical work done can be calculated under reversible condition. Work done under reversible condition, although not attainable in real conditions, can act as a reference to estimate the performance of a fuel cell. Equation 1.3 expresses the correlation between the maximum work being equal to the change of Gibbs free energy when the irreversibility of the system is taken as zero.

$$W_{\max} = -\Delta G \quad (1.3)$$

Since fuel cells are an electrochemical power generation device, the maximum work is expressed in terms of electric potential, E , in volts, as follows.

$$E = \frac{\delta w}{nF} \quad (1.4)$$

where E is the cell potential difference between cathode and anode or the electric potential of the cell, δw is the work done, n is the number of moles of electrons given or utilized per mole of fuel or reactant and F is Faraday's constant ($F = 96487 \text{ C/ mole electrons}$). In Equation 1.5 the maximum cell potential, E_{\max} , can be expressed as

$$E_{\max} = \frac{W_{\max}}{nF} = \frac{-\Delta G}{nF} \quad (1.5)$$

The second law of thermodynamics restricts fuel cell to a maximum efficiency achievable under reversible condition. Equation 1.6 shows the second law efficiency of a fuel cell.

$$\eta_r = \frac{\Delta g}{\Delta h} \quad (1.6)$$

where Δh and Δg are the change in enthalpy and Gibbs free energy, respectively, which both are function of temperature. Increasing the temperature leads to an increase in entropy which decreases the efficiency.

Along with thermodynamics of fuel cells, kinetics are equally important. Through a kinetics studies, insights into actual operation and associated losses can be gained. In a fuel cell the electrochemical reactions occur at the anode and cathode and both electrodes have their own electrode potential. In Equation 1.7 the overall cell potential can be correlated as the difference between the cathode and the anode potentials

$$E_r = \varphi_{c,r} - \varphi_{a,r} \quad (1.7)$$

where $\varphi_{c,r}$ is the reversible cathode potential and $\varphi_{a,r}$ is the reversible anode potential, E_r is the overall reversible cell potential. Under irreversible conditions, the overall cell potential can be calculated using Equation 1.8.

$$E = \varphi_c - \varphi_a \quad (1.8)$$

where φ_c is the actual cathode potential and φ_a is the actual anode potential. By subtracting Eqs. 1.7 from Eqs. 1.8 the overpotential can be determined, as shown in Equation 1.9

$$\eta = E_r - E \quad (1.9)$$

The cathode and anode overpotentials can be determined by using Equations 1.7-1.9. When a load is applied to the cell, or current is extracted from the cell, the anode potential increases and the cathode potential decreases. This is translated to an overall decrease in the cell potential, reflective of the amount of load or current extracted through the cell.

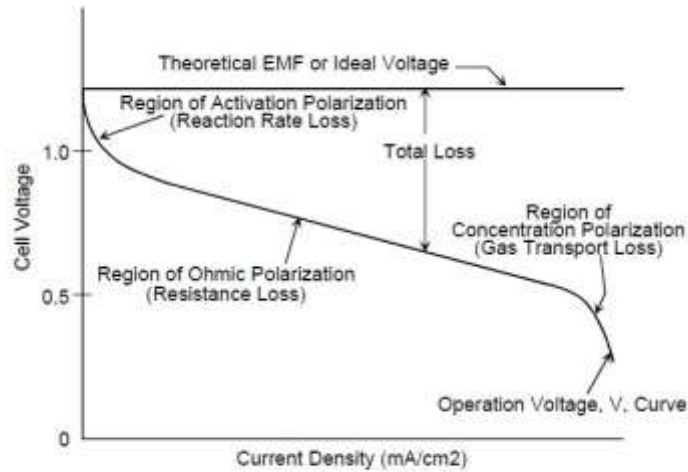


Figure 1.1: Ideal and Actual Fuel Cell Voltage/Current Characteristic [5]

Figure 1.1 displays cell voltage versus current density and the different operational zones. The first operational zone, the low current density zone, depicts activation polarization. This potential loss is associated with activation of electrochemical reactions taking place at the electrodes. The activation barriers of these reactions is in turn dependent on the reaction kinetics and the activity of the electrocatalyst. [5,6].

In contrast, the second zone shows the ohmic overpotential which represents the potential losses incurred due to resistance to transport of charge in the system. This can comprise resistance to ions travelling through the electrolyte and electrons travelling through current collectors and interconnects. The ohmic resistance is dependent on the materials used, cell geometry and temperature [5].

The last operational zone, at high current density, represents the concentration polarization which occurs because of mass transfer limitations. When the load is high and the reactants cannot get to the active sites in time, the cell potential reduces drastically. The current density where potential decreases to zero is limiting current density.

1.1.2 Types of Fuel Cell

Essentially all fuel cells have the same working principle; the difference comes in the type of charge, positive or negative, transported through the electrolyte. Similarly, the operating temperature is also dependent on the chosen electrolyte. Fuel cell types are listed below in terms of electrolyte types and operating temperature.

1. Solid Oxide Fuel Cells (SOFC):

In this type, solid ceramic nonporous rare earth metal oxide are used as electrolyte such as yttrium stabilized zirconia oxide and doped ceria to transport negative charged oxygen ions towards the anode. The use of ceramic materials demands a high operating temperature in the range of 600-1000°C to attain enough ionic conductivity.

2. Molten Carbonate Fuel Cells (MCFC)

In this type, alkali carbonates or a mixture thereof, such as lithium and potassium carbonates, are used as electrolyte to transfer negative carbonate ions. For adequate conductivity high operating temperatures close to 650°C are used.

3. Proton Exchange Membrane Fuel Cell (PEMFC)

In this type, ion exchange polymer membrane such as fluorinated sulfonic acid polymer is used as electrolyte to transfer positive charge hydrogen ion instead of negative charge. The operating temperature is low for PEMFC, in the range of 60 to 80°C.

4. Phosphoric Acid Fuel Cells (PAFC)

Phosphoric acid is used as electrolyte in this type of fuel cell to transfer protons into the electrolyte. Phosphoric acid is used as the electrolyte due to its higher stability compared to other electrolytes. The operating temperature for PAFC is in the range of 150 to 220°C.

5. Alkaline Fuel Cells (AFC)

Alkaline solution is used as electrolyte in this type. In this case negative hydroxyl ions transfer into electrolyte. Potassium hydroxide (KOH) electrolyte is the most common selection. The operating temperature depends on the concentration of potassium hydroxide, for example if it is high concentration, the operating temperature is high in the range of 100-250°C.

Since SOFC is capable of transporting negative oxygen ions they do not have the limitation of using hydrogen as a fuel allowing it to be more fuel flexible. Table 1.2 shows a further comparison of fuel cell types in terms of electrolyte type, operating temperature and efficiency.

Other than fuel flexibility, SOFC also has a higher distributed system level efficiency. This Table 1.2: Summary of Major Differences of the Fuel Cell Types [5, 6]

	PEMFC	PAFC	MCFC	SOFC
Type of Electrolyte	H ⁺ ions (with anions bound in polymer membrane)	H ⁺ ions (H ₃ PO ₄ solutions)	CO ₃ ²⁻ ion (typically molten LiKaCO ₃ eutectics)	O ²⁻ ions (Stabilized ceramic matrix with free oxide ions)
Common electrolyte	Solid polymer membrane	Liquid phosphoric acid in lithium aluminum oxide matrix	Solution of lithium, sodium, and/or potassium carbonates soaked in a ceramic matrix	Solid ceramic, Ytria stabilized zirconia (YSZ), Doped Ceria
Electrodes	Carbon	Carbon	Nickel and Nickel Oxide	Perovskite /metal cermet
Catalyst	Platinum	Platinum	Electrode material	Electrode material
Interconnect	Carbon or metal	Graphite	Stainless steel or Nickel	Nickel, ceramic, or steel
Internal reforming	No	No	Yes, good temperature match	Yes, good temperature match
Operating Temperature	40 – 80°C	205°C	650°C	600 – 1000°C
Charge Carrier	H ⁺	H ⁺	CO ₃ ²⁻	O ²⁻
External Re-former for hydrocarbon fuels	Yes	Yes	No, for some fuels	No, for some fuels and cell designs
External shift Conversion of CO to hydrogen	Yes, plus purification to remove trace CO	Yes	No	No
Oxidant	Air to O ₂	Air to enriched air	Air	Air

Prime Cell Components	Carbon-based	Graphite based	Stainless-based	Ceramic
(Distributed Generation) DG system level efficiency (%HHV)	25 to 35%	35 to 45%	40 to 50%	45 to 55%

makes SOFC a good choice of research both academically and industrially.

1.2 Basics of Solid Oxide Fuel Cells and its Application

In 1838, William Groove invented the first fuel cell which was referred to as the Groove Cell [7]. Since then, significant progress has been made in the field of fuel cells. Pertaining to SOFC, Gaugain, Nernst and Wanger had significant contributions. Solid electrolyte was discovered by Gaugain in 1853 [8], then in 1897 Nernst reported that ionic conductivity was improved by doping of zirconia with 15% yttrium [8]. Much later in 1943, Wagner discovered that oxygen ions travel through metal oxides via a vacancy hopping mechanism [9]. This led to a lot of research in oxygen conduction mechanism leading to a high number of patents being filed in the 1960-70s [10]. A lot of this work has been devoted to the discovery of non-porous solid ceramic materials, like yttrium stabilized zirconia (YSZ) and doped ceria, which show good oxygen ion conductivity at high temperatures, close to 1000 °C [11]. This oxygen conducting ceramic material when sandwiched between a solid anode and cathode forms a solid oxide fuel cell (SOFC).

SOFCs are termed solid because having all solid components. The requirement of sufficient conductivity from electrolyte demands high operating temperature, which leads to the possibility of internal reforming of carbon containing fuel, further enhancing the fuel flexibility of these types of cells [12, 13]. Figure 1.2 shows a schematic of a SOFC.

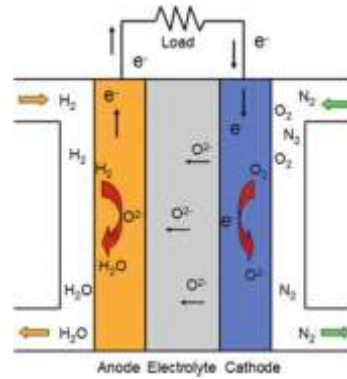
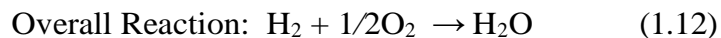
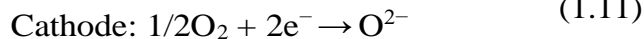
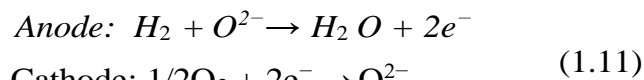


Figure 1.2: Schematic of a solid oxide fuel cell [12]

Fuel, for example in the form of hydrogen, gets to the triple phase boundary (TPB) at the anode, where it is electrochemically oxidized to form water while giving away electrons. These electrons pass through an outer circuit while travelling to the cathode. Oxidant in the form of air or oxygen diffuses into the cathode and reaches the TPB at the cathode-electrolyte interface, where the oxygen is electrochemically reduced, while taking the electrons coming from the outer circuit, forming oxygen negative ions. These negative oxygen ions travel through the electrolyte towards the anode where they react with hydrogen to form water. Hence half reactions take place at both electrodes that can be combined to form a global reaction. Equations 1.11 and 1.12 show the half-cell reactions and the global reaction when hydrogen is used as a fuel.



Higher efficiency, fuel flexibility and possibility of heat integration have made SOFC a possible choice for applications such as Auxiliary Power Unit (APU), Combined Heat and Power (CHP) systems, and large-scale power plants [12]. A promising application of SOFC is its application as a power source in desalination [14]. A techno-economic analysis of SOFC as a power source to desalinate seawater in Persian (Arabian) Gulf using reverse osmosis (RO) has shown that in comparison to a gas turbine powered system, a SOFC powered system shows a higher exergy efficiency of 29% [14]. There are numerous reports in literature focused on SOFC integrated thermal desalination [15-20], RO [21] and hybrid thermal-RO [22] systems. Hosseini et al. [16] have reported the exergy efficiencies of SOFC-GTs and SOFC- GTs integrated with heat recovery steam generator (HRSG)- multiple-effect distillation (MED), and these efficiencies

have been recorded as 55% and 64%, respectively. The fresh water production cost has been reduced from 2.5 to 1.9 USD/m³ when SOFC-(multi-stage flash) MSF has been integrated [14]. In comparison to standard gas turbine (GT) power which is 10 MW, SOFC coupled with gas turbine can improve power to 25 MW [14]. By integrating SOFC with GT organic Rankine cycle(ORC)-(Reverse Osmosis) RO system net annual cost can be saved; which would be around 8.2–21 million USD, for supported and unsupported water/gas prices, respectively [14]. However, there are some of problems found in SOFC integrated with GT which are stability issues, gas turbine (GT) pressure fluctuations limited operating pressure and complex controls [23-26]. In Figure1.3, a co-generation system is shown.

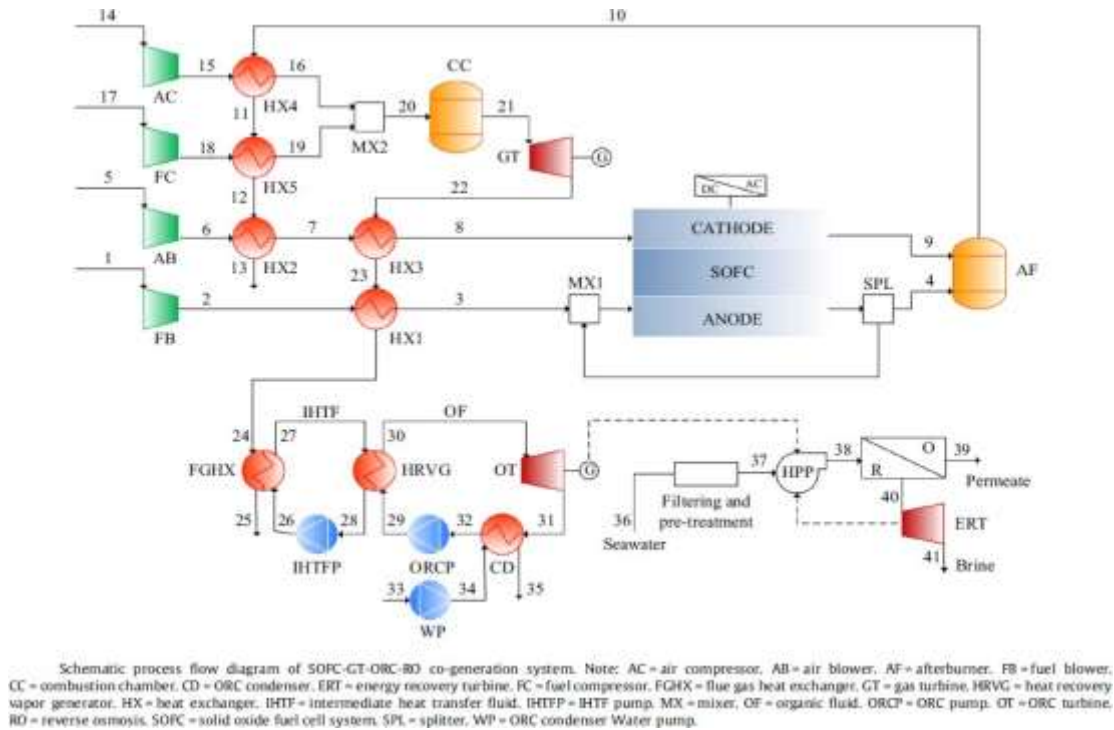


Figure 1.3: A co-generation system for water desalination [14]

Based on the thickness of cell components, anode, electrolyte and cathode, SOFC can be categorized into three different types. When the anode is left thicker compared to the other two components, the cell is generally labelled as Anode Supported Cell (ASC), a similar nomenclature is used for when electrolyte and cathode are left thicker. Generally, ASCs are more common because a thicker electrolyte leads to higher ohmic losses and a thicker cathode leads to higher cathode polarization losses, both being more important than anode polarization

losses. Even though very attractive, there are many challenges in the material, fabrication and life of a SOFC. These challenges are discussed in the next section.

1.3 Challenges

Most of the problems or challenges in SOFC can be categorized into two different categories:

Materials used: Since SOFC operate at high temperatures, it is easier for cell materials to interact. For instance, interaction of YSZ (common electrolyte material) with cobalt containing cathode has been regarded as a factor of degradation. Similarly, at high operating temperatures coarsening of nickel particles (anode catalyst) has also been reported.

Operation wear and tear: High operating temperature can lead to physical damage to the cell. For instance, during start up and shut down, a cell goes through a drastic thermal cycle. If not handled carefully this thermal cycle, based on material mismatch, can lead to warping and cracking of cell. Figure 1.4 gives a diagram outlining common cell materials and their associated issues.

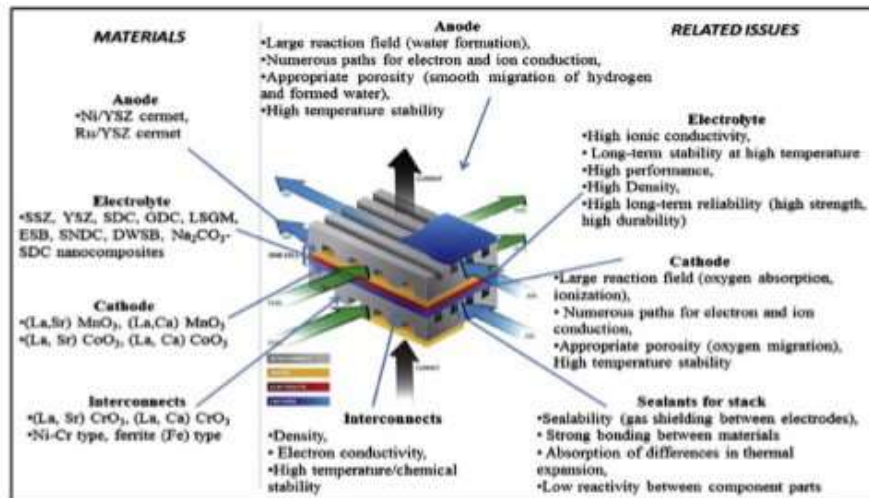
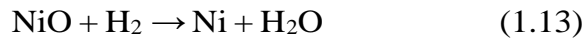


Figure 1.4: Material limitation for SOFC [8]

The anode mostly comprises reduced nickel oxide mixed with the electrolyte material (doped zirconia or doped ceria) [12, 31-33]. The choice of nickel is based on electronic conduction and catalytic activity towards methane reforming and electrochemical hydrogen reduction, even though the use of nickel presents several problems. Nickel particles diffuse and fuse together at

high temperatures, referred to as coarsening of particles [27-29]. Coarsening of particles can lead to reduction in Triple Phase Boundary (TPB), which in turn leads to cell performance degradation due to loss of active area [1, 11, 30]. Other than electrochemical performance loss due to reduction of TPB, changes in microstructure can also lead to physical strain and damage to the cell. Another reported problem is the redox cycling of nickel in case of fuel cut-off. In its original structure nickel is added as nickel oxide and goes through a reduction cycle prior to cell operation. In case of fuel cut-off, nickel can be oxidized to nickel oxide. The redox cycle reactions are shown in equations 1.13 and 1.14



This can lead to a thermal shock at the anode as there is a significant mismatch between reaction energy for the reduction and oxidation. The enthalpy of reduction reaction is -13 kJ.mol^{-1} , but the amount of enthalpy for the oxidation reaction is $-239.8 \text{ kJ.mol}^{-1}$ [34]. Furthermore, re-oxidizing nickel can lead to a volume change of 69% which can induce a substantial physical strain on the cell leading to physical damage [31,32, 34, 35]. Waldbilig et al. [36] have extensively studied the degradation of nickel-based anodes. Figure 1.5, shows microstructure of anode for an anode supported cell after redox cycling; the crack on the electrolyte is attributed to redox cycling.

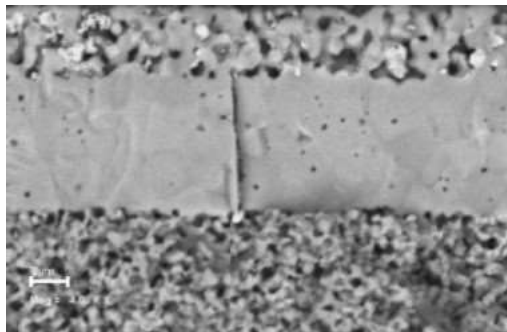


Figure 1.5: SEM BSE image of a large vertical electrolyte crack in a fresh fractured anode-supported SOFC after redox cycling. [36]

In literature, redox cycling is considered as a primary degradation mechanism of anode supported cells [35-39].

Another significant degradation mechanism is the thermal cycling of the cell. Since conventional cells are made of different ceramic materials that are layered, they do not have identical coefficients to thermal expansion and are brittle; as such, a quick heat-up and cool-down can lead to cell warping and cracking [31]. Continuous thermal cycling can also lead to permanent changes in the CTE of Ni/YSZ anode which can aggravate the physical strain that occurs during thermal cycling [31,40].

In the last 2 decades a lot of work has been devoted to a new generation of SOFC, also called the third generation SOFC. These cells have a thick and porous metal support in addition to the three primary components. These cells are commonly referred to as metal supported – solid oxide fuel cells (MS-SOFCs). Figure 1.6 shows schematics of anode supported – SOFC, cathode supported (CS) - SOFC and MS-SOFCs. Table 1.3 shows the advantages and disadvantages of these configurations.

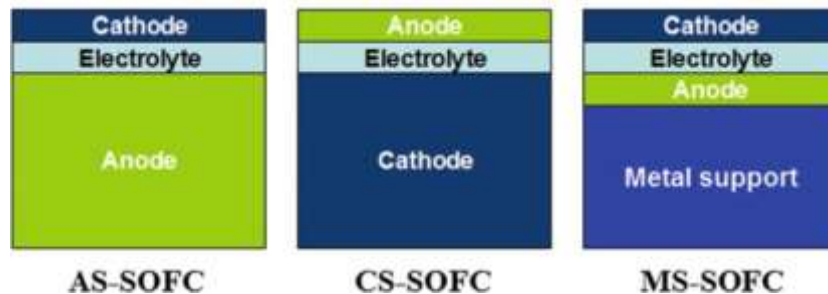


Figure 1.6: schematic diagram of different SOFC configurations [12].

Table 1.3: Advantages and disadvantages of a different SOFC configuration [12]

SOFC configurations	Advantages	Disadvantages
CS-SOFC	High redox stability of the anode	Low output power
AS-SOFC	Low operating temperature high output power	Low redox stability
MS-SOFC	Lower cost, high mechanical strength, excellent redox and thermal shock tolerance	Densification issue of the electrolyte, oxidation of the metal, Cr poisoning issue

The MS-SOFC architecture allows for thinner ceramic layers which can instill many benefits in the cell. The active materials are expensive in comparison to the metal support and hence having thinner layers for active components reduces the cell cost. Furthermore, the mechanical integrity of the cell is increased which comes through the metal support which is more resistant to physical strain and shock compared to brittle ceramic materials [13, 41].

Although this concept offers many advantages, it has been reported that fabrication of such cells can be challenging [13]. From different materials available, ferritic stainless steel has been utilized as a preferred choice by many researchers [6]. Even though work on MS-SOFC dates as far back as 1960s, when austenitic steel support was used with a zirconia electrolyte with a reported performance of 115 mW.cm^{-2} at $750 \text{ }^\circ\text{C}$ [42], it was only in the last two decades that significant progress was made. For a high performing cell, the electrolyte must be gas tight. This can be achieved through high temperature sintering or thermal deposition techniques like Pulsed Laser Deposition (PLD) or Plasma Spray Deposition (PSD). There are many reported advantages and disadvantages of thermal deposition techniques reported in the literature [41]. Essentially, in a thermal spray deposition method the electrolyte is deposited on a prefabricated metal support, which can have the advantage of adequate electrolyte density at lower temperature. However, it has been reported that ionic conductivity of sintered YSZ electrolyte is higher than that deposited through PSD [1, 43]. To compensate for the lower conductivity, cells with plasma spray deposited electrolyte are operated at higher temperature, 800°C , which can lead to oxidation of the metal support [1]. Another drawback of using thermal spray

deposition is the possibility of localized hot spots on the electrolyte surface which can lead to cell failure [44]. Thermal spray methods are also difficult to implement, in term of parameter tuning, and can also require large processing times. Hence the applicability of these is debatable. In comparison, co-sintering of metal support with electrolyte offers a solution. Essentially the electrolyte and metal support layers are casted in sheet form, press-laminated together and sintered together at high temperatures [6]. Using wet metallurgy and tape casting, a MS-SOFC with a fully sintered YSZ electrolyte, 10-20 micron in thickness, has been reported to be able to operate at lower temperatures (650-700°C) [1]. Even though a lot of literature has been published on the use of tape casting coupled with co-sintering for the fabrication of MS-SOFCs [45, 46], there are many challenges in using this processing route [1]. The components sintered together fall in different material categories, while the support is a metal, the active component is a metal oxide.

During firing at high temperature this material mismatch can lead to cracking, warping and delamination [32]. Similarly, the high sintering temperature requires a reducing atmosphere to avoid the oxidation of the metal support. However, the use of reducing atmosphere at high sintering temperature, higher than 1200°C, can lead to chemical changes in the cathode layer (if the cathode layer is co-sintered with the metal support and electrolyte) [1, 41]. This brings about a limitation both in choice of cathode materials and the processing route of these materials. Even after co-sintering of metal support and electrolyte in reducing atmosphere, the cathode will have to be sintered while protecting the metal support from excessive oxidation. As such, cathodes' sintering needs to be done at temperatures much lower than those conventionally used (higher than 1000°C) if sintered in air, or must be sintered in inert atmosphere when higher temperature is required. As an alternative to the above-mentioned ex-situ cathode sintering, some researchers have tried in-situ cathode sintering, where cathode is applied to a sintered metal support-electrolyte structure and sintered in the test setup prior to operation. Since the electrolyte is dense, the atmosphere for the metal side (anode) and cathode can be different, thereby protecting the metal support [47, 48]. The limitation in choice of cathode material and tuning of cathode in-situ sintering still remains though. Using in-situ sintering temperatures up to 900-1000°C are applicable which is still lower than that required for conventional cathode materials of cathode catalyst. Limited research has been published on cathodes that can be sintered in-situ at lower temperatures [48, 49]. Moreover, in-situ sintering

is difficult to scale up.

Hence this work presents a study on cathode sintering for MS-SOFCs. The first approach is to assess ex-situ sintering in non-oxidizing atmosphere. The sintering behaviors and stability of LSCF cathode catalyst under different atmospheres and temperatures has been investigated to optimize the cathode processing [49]. The second proposed solution is to use a porous cathode scaffold instead of a stand-alone cathode layer. The porous scaffold can be made from the electrolyte material and can be co-sintered with metal support and electrolyte. This porous scaffold can be later infiltrated by cathode material and in-situ sintered prior to operation. This approach also has the potential of increasing the TPB in the cathode [50]. Reports about the use of porous YSZ scaffold has been published by Zhan et al. [6, 41, 51]. Also, it has been reported that YSZ can react with lanthanum and cobalt containing cathode materials [52,53]. However, SDC as a porous scaffold for cathode has not been investigated to the best of authors knowledge. SDC has higher conductivity than YSZ and is a mixed ionic and electronic conductor which might increase cathode conductivity and lower cathode overpotential. Hence, the objective of this research is first to fabricate MS-SOFC without using in-situ cathode sintering and secondly to fabricate MS-SOFC with reasonable performance ($500-1000 \text{ mW.cm}^{-2}$) at intermediate cell operating temperatures ($700-800^\circ\text{C}$).

1.4 Thesis Organization

Chapter 1 gives an introduction to this work and outlines the motivation and objectives as well. Chapter 2 comprises a literature review mostly focused on materials used for active cell components and the metal support, and the different cell architectures studied. Then, in chapter 3, the experimental approach, experimental procedures, brief summary for experimental devices and method used in this research are given. Experimental results and analysis are given in Chapter 4 followed by conclusions and recommendations for future work in Chapter 5.

Chapter 2 Literature Review

2.1 Metal Supported Solid Oxide Fuel Cells

Metal Supported – Solid Oxide Fuel Cell (MS-SOFC) provides numerous advantages over conventional all ceramic cells. Other than enhancing the physical integrity, MS-SOFC also improves thermal and redox tolerance of cells, and reduces material cost by allowing for application of thinner layers for active material [1,41-42]. Although the majority of the research on MS-SOFC is reported in the last three decades, the first reported case dates as far back as 1960s [6,42], when austenitic steel as support with stabilized Zirconia as electrolyte. Since 1990s major groups with significant contribution to literature are the Lawrence Berkeley National Laboratory (LBNL), Danish Technological University (DTU), Ceres Power, Forschungszentrum Julich, Riso National Laboratory, Topsoe Fuel Cells (TFC), and the University of Toronto [6,54].

Although attractive, MS-SOFC faces many challenges. The first challenge is that of the material mismatch; whereas the support is made of a metal other cell components are metal oxides. Hence the difference in shrinkage during sintering and coefficient of thermal expansion (CTE) during fabrication and operation can lead to physical defects, like cracks, warping and delamination, of the cell [1,6,55]. This issue can be solved by choice of metal which has a similar CTE to that of other cell components.

Another challenge is the fabrication of MS-SOFCs. For cell integrity, performance and life, cell components have to adhere to each other which primarily comes from the fabrication route. Even though researchers have reported successful use of thermal spray deposition method, these methods are difficult to scale up because of complex fine tuning, long processing time, possibility of hot spots on cells and in some cases incapability to attain fully dense electrolyte [56,57]. Another fabrication route is the use of wet powder metallurgy and co-sintering of casted metal and other cell component layers together. This is challenging as the presence of metal imposes many limitations. Firstly, to achieve full density of electrolyte high temperature sintering, in the range of 1300-1400°C, is required [54]. At these high temperatures the components of the metal alloy

can go through interdiffusion. It has been reported that treating stainless steel metal support with nickel based anode at high temperature can lead to interdiffusion of iron, chromium and nickel [58-61]. Similarly most metals exhibit higher shrinkage than metal oxides, and hence a mismatch can lead to physical defects in the cell. Another limitation comes in the form of sintering atmosphere; to avoid metal oxidation, sintering has to be carried out in non-oxidizing atmosphere [13]. Another challenge comes directly from the use of non-oxidizing atmosphere, where most cathode materials (primarily metal oxides) are unstable in reducing atmosphere at high temperatures. Hence, a MS-SOFC cannot be sintered with metal support and cathode layer in a single sintering step [6,54]. Some reports exist which demonstrate sintering of cathode on an already sintered metal support-electrolyte half-cell in inert atmosphere [62].

Based on the discussion above, MS-SOFC challenges can be categorized into two sections: the choice of material and the cell failure during fabrication and operation. Hence this literature covers extensively the topic of materials and the challenges faced during the fabrication and operation of MS-SOFCs. This review provides a comparison of different materials used for metal support and cell active components, and different fabrication techniques. It should be noted, though, that due to inconsistency in testing conditions, variations in cell materials and architecture it is rather impossible to draw a direct comparison. Comparison is mostly seen in the form of polarization curve and life tests of cells complemented by microstructure analysis.

2.2 The Selection of Metal Supported Cell Materials

2.2.1 The choice of metal support

In general the following are the requirements from a metal support used in MS-SOFC [6]:

1. The metal to be used should be inexpensive.
2. The metal should have a high tolerance to oxidation.
3. The metal should have high tolerance to thermal cycling
4. The metal should have similar shrinkage behavior and CTE as that of other cell components.

Several types of metal alloy have been utilized as metal support, but the most preferable alloy is ferritic stainless steel (FSS). The reasons are summarized below in Table 2.1 in which the comparison between metal alloys have been made in terms of CTE, cost, oxidation rate and mechanical strength. Figure 2.1 shows the phase diagram of Cr-Ni-Fe based alloy; in which their properties have been stated above Table 2.1, and this diagram is estimated by Yang.

Table 2.1: The comparison between metal alloys [41,63].

Alloys	CTE (ppmK ⁻¹)	Cost	Oxidation resistance	Mechanical strength
Cr based	11.0-12.5	Very expensive	Good	High
Ferritic SS	11.5-14.0	Cheap	Good	Low
Austenitic SS	18.0-20.0	Cheap	Good	Fairly high
Fe based supper alloy	15.0-20.0	Fairly cheap	Good	High
Ni based super alloys	14.0-19.0	Expensive	Good	High
Ni	16.0-17.0	Expensive	Low	Low
NI-Fe	13.0-14.0	Fairly expensive	Low	Low
NiCrAlY	15-16	Expensive	Excellent	Good
Hastelloy-X	15.5-16	Expensive	Excellent	Good

Note that CTE of electrolytes (YSZ, CGO, LSGM are in the range $10 - 12 \times 10^{-6} \text{K}^{-1}$)

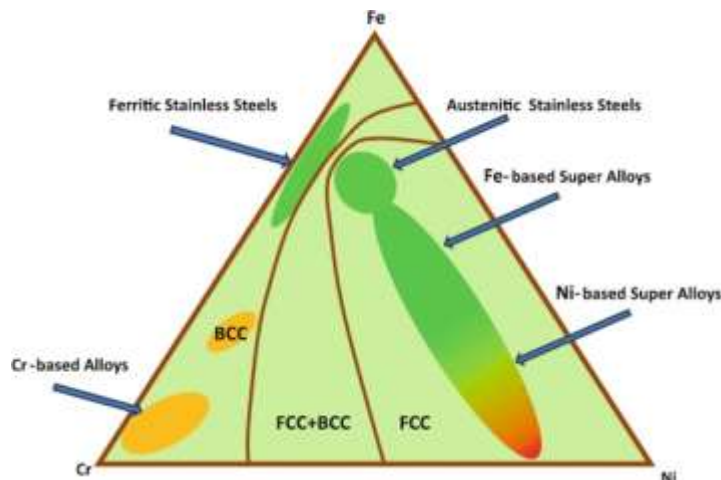


Figure 2.1: Schematic phase diagram for Cr-Ni-Fe system [64]

From Table 2.1, it can be seen that ferritic stainless steel (SS) –(e.g. 430L) have a CTE (11.5-14.0 ppm.K⁻¹) very close to that of common electrolyte materials (CTE for both YSZ and SDC is in the range of 10-12 ppm.K⁻¹) [41]. Further, SS-430 is cheaper compared to Hastelloy X and NiCrAlY alloy and exhibits higher resistance to oxidation when compared to SS-300 series [13, , 41, 54]. It has been reported that Ferritic stainless steel (SS)-430L has 16- 18 % chromium, and this amount of Cr content can create an electrically conductive protective layer of chromium oxide [32, 54]. As a result, SS-430L can conduct electrons [32, 54]. Although chromium can form a protective oxide coating, the atmosphere experienced during SOFC operation is harsh and can potentially lead to oxidation of ferritic stainless-steel with chromium content as high as 16-18% [65]. Table 2.2 shows the composition of SS-430 and SS-440 in weight percent.

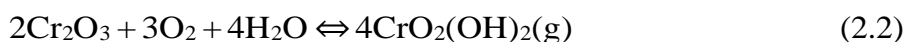
Table 2.2: Components of stainless steels utilized in metal support for SOFC [32,66,67]

Element	430 Stainless steel (wt %)	434 Stainless steel (wt %)	440 stainless steel (wt%)
Cr	16-18	16.66	16-18
Mn	< 1	0 .14	< 1
Si	< 1	0 .85	< 1
P	< 0.04	0.016	< 0.04
S	< 0.03	0.006	< 0.03
C	0.12	0.012	0.95-1.2
Mo	-	0 .94	0.75

It has been recorded that the maximum recorded power density (MPD) at 700°C is 246mW. cm⁻², when SS-430L has been utilized as metal support which contains 16-18% of chromium [68]. In other study, Tucker has been reported that the maximum recorded power density (MPD) at 700°C is 1.56W. cm⁻², when SS-434L has been utilized as metal support which contains 16.66% of chromium [69].

Although stainless steel seems like a good option, there are some downsides to the presence of chromium in the system. Firstly, the shrinkage rate of stainless is dependent on the amount of chromium and should be tuned to match that of ceramic components being sintered together [32]. Secondly, chromium is known to poison metal oxides used as catalyst in the cathode which can lead to decreased cell performance and eventually failure. Chromium oxide, which may form due to oxidation of metal support, can exist in volatile hexavalent oxides which are volatile and can also lead to poisoning [70, 71]. The chemical equation of chromium oxide conversion to

volatile chromium oxides is shown in equations 2.1 and 2.2 [70,71].



Though chromium oxide; which is formed in SS430-L, can protect SS-430L from oxidation, a buildup of it in SS-430L can lead to the formation of a fragile oxide layer; moreover, it may decrease the electrical conductivity which is undesirable in metal support cell applications [13, 54]. In the case of excess oxidation, the scale of chromia grows and will eventually lead to spalling. This can lead to physical defect failure of the cell [1,6,41]. It is reported that a scale thickness of 5 micron, which can grow over 30,000 hours of operation, is the threshold after which spalling can occur [46]. Another source of reduction in conductivity is the aluminum and silicon present in stainless steel, similar to chromium they can form non-conductive oxide leading to decreased cell performance [6, 13]. When Si element is added into the stainless-steel composite the adhesion among chromia scale and stainless-steel surface is improved due to silicon oxide formation which has formed by addition of Si [13]. However, another issues, which can affect the performance of cell when the ferritic stainless steel is used as metal support, is the use of high amounts of silicon and aluminum in ferritic stainless steel which can create non-conductive oxide during operation [6]. It has been reported that even a silicon content as low as 0.017 wt% can still undergo oxidation in SOFC operating conditions [6,13, 72].

Another option for use as metal support is the use of Ni based alloys and ceramic composites. Nickel is known for its activity towards electrochemical hydrogen oxidation and reforming of methane. It has been reported that a Ni-YSZ composite as anode can help in matching the CTE of anode and YSZ electrolyte thereby reducing the chances of cell warping during start-up and shut-down [13]. Nickel alone has a CTE of 16.5 ppm.K⁻¹ compared to 12.4 ppm.K⁻¹ of GDC [54]; however, it has been reported that alloying nickel with iron can reduce the CTE to match it with YSZ and GDC electrolytes [41]. Similar reports have been published regarding alloying nickel with molybdenum, where a MPD of 1196 mW.cm⁻² was reported at 750°C when Ni-Mo alloy was used as a metal support [6,13, 73, 74]. Gdansk University of Technology in Poland has studied nickel and chromium alloys in terms of corrosion rate and corrosion resistance, particular IN625 [75] and PI600 [76]. They found that the corrosion rate of IN625[75] has been reduced when the rare earth elements is infiltrated through porous alloy, and they concluded that yttria

element has more effect in reducing corrosion rate of IN625 than other elements. Furthermore, they found that by infiltrating yttria element; which is prepared in precursor solution, into porous P1600 alloy [76] the corrosion resistance is enhanced.

Despite being explored extensively, the use of nickel has several challenges. Other than being expensive, nickel does not have a high resistance to redox cycling, which can lead to cell failures [13,41].

Another grade of stainless steel explored is the Crofer 22 APU and 22 H, which have up to 24 wt% chromium. Heat treatment of 22 APU in 50% humidified atmosphere at 800°C showed that a 30 hour exposure led to an area specific resistance (ASR) of 0.02-0.03 [6,13,63,77,78].

2.2.2 Choice of Anode Materials

The primary purpose of anode is to facilitate electrochemical oxidation of fuel and conduct electrons to the outer circuit [1, 6]. Based on these functionalities, the anode material should have the following qualities:

1. High electrical conductivity to enhance transport of electrons to the outer circuit from the active sites
2. High activity towards fuel oxidation
3. Compatible CTE with electrolyte material to prevent cell warping and/or cracking during start up or cool down.

Nickel has been a common choice as having the above qualities; it is also active towards internal reforming of carbon containing fuels [6, 11, 31]. However, pure nickel is seldom employed as the anode and is mixed with either SDC or YSZ (electrolyte material) to match the CTE of anode with electrolyte [6,11]. Adding SDC and/or YSZ can also lead to an increase in the TPB thereby enhancing the cell performance [6]. The first study of nickel-zirconia cermet dates back to 1970 in the form of a patent [11,79]. However, it is also reported that Ni with YSZ exhibits a lower tolerance to redox cycling [80]. It is also reported that Ni-YSZ anode cermet has a lower resistance to sulfur poisoning [81]. Nonetheless, Ni-YSZ remains one of the common choice for anode of SOFCs [11].

The case of MS-SOFCs makes the use of nickel even more challenging, for example, issue of interlayer diffusion of chromium (from stainless steel support) and nickel (from anode) has been reported extensively [6, 60, 61, 82, 83]. When metal/anode/electrolyte half-cell is co-sintered at high temperature can lead to chromium diffusion into the anode causing chromium poisoning [83, 84]. Even during high temperature operation, interlayer diffusion is possible and can lead to formation of electrically insulating Cr_2O_3 , NiCr_2O_4 and iron oxides [11, 41], which can increase the anode polarization resistance [58]. In the same way, nickel from anode can also diffuse into stainless steel metal support; the incorporation of nickel into stainless steel can change the stainless steel to austenitic steel [1,6,11,64]. It has been reported that the CTE value of austenitic steel ($18\text{-}20 \text{ ppm.K}^{-1}$) [11,41] which is very different from that of common electrolytes, can lead to physical defects during operation [6, 11].

Figure 2.2 shows SEM image superimposed with EDAX elemental map for a MS-SOFC fabricated using plasma spray deposition, it is clear that after 1500 hours of operation interlayer diffusion took place. Despite these issues researchers still focus on the use of nickel as it can increase fuel flexibility. In the recent past many researchers have published work outlining changes in the structure of MS-SOFC that can help mitigate interlayer diffusion. These methods include adding diffusion barrier layer (DBL), lowering fabrication and operation temperatures, and decorating porous metal support with anode material rather than having a separate anode layer.

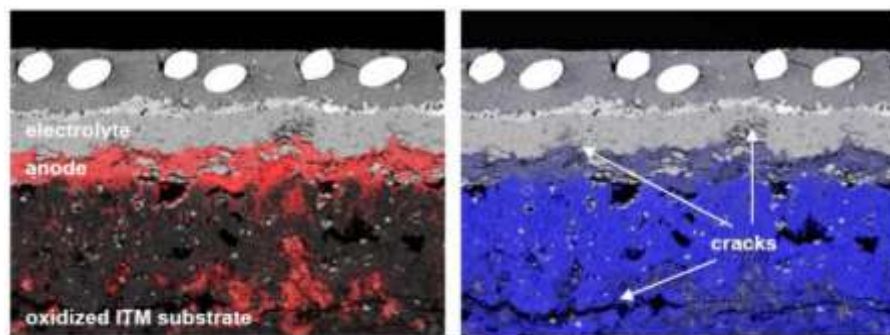


Figure 2.2: EDAX/SEM composite image of cross-section of MS-SOFC produced by plasma spray processing after 1500 H operation at 800 °C (Left: Ni distribution in red, Right: Fe distribution in blue)[60].

Another degradation mechanism for nickel-anode SOFCs and MS-SOFC is the coarsening of nickel particles during manufacturing and operation. It has been reported that MS-SOFC co-sintered showed a dense anode structure, attributed to coarsening of nickel, which led to a very low MPD of 100 mW.cm^{-2} [12, 29]. Figure 2.3 shows SEM image of Ni coarsening for a cell sintered in H_2 reducing atmosphere at 1400°C and sintered in air and then reduced at 800°C in H_2 . In this figure, comparatively large (coarsened) Ni grains with non-homogenous microstructure can be seen for cell sintered at 1400°C in H_2 [1, 85].

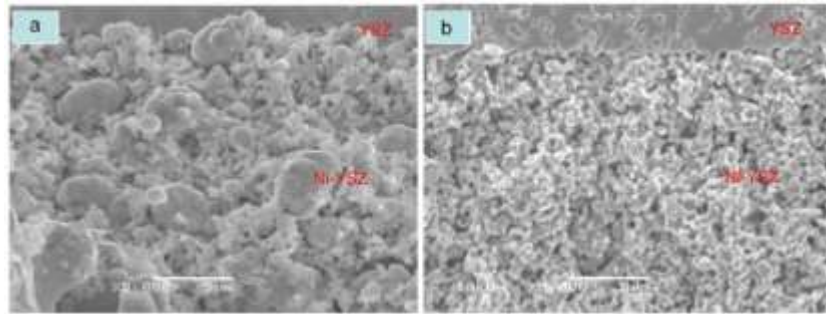


Figure 2.3: Electrolyte and anode microstructure of (a) Cell sintered at 1400°C in H_2 and (b) Cell sintered at high temperature in air and then reduced at 800°C in H_2 [1,85].

However, the coarsening of nickel during manufacturing can be avoided through infiltration of nickel particles into the porous metal of sintered metal-electrolyte substrate. In Figure 2.4, SEM images are taken at LBNL for sintered cell before anode infiltration and sintered cell after Ni anode infiltration.

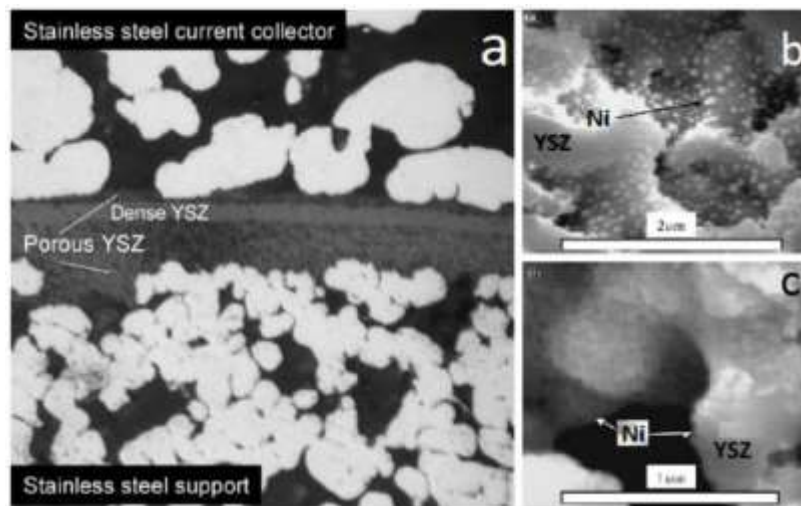


Figure 2.4: (a) Microstructure of the cell fabricated at LBNL by co-sintering before the catalyst infiltration, and the microstructure of anode after Ni infiltration (b) once and (c) 5 times [41, 86]

It has been reported that a MS-SOFC with 2 wt% loading of nickel catalyst shows an initial combined polarization resistance of $2.28 \Omega \cdot \text{cm}^2$ [51] which increased to $3.5 \Omega \cdot \text{cm}^2$ after a 12 hour operation, the authors attributed this increase to coarsening of nickel [51]. Figure 2.5 shows impedance spectra of this cell.

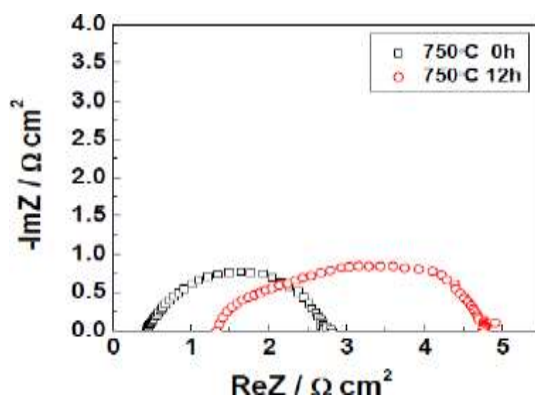


Figure 2.5: Impedance spectra of the single MS-SOFC before and after the 12h measurement at 750°C . [51]

Zhan et al. [87] reported a combined polarization resistance of $0.12 \Omega \cdot \text{cm}^2$ when nickel, combined with SDC, was infiltrated as the anode into the porous metal support. This is attributed to firstly increased TPB due to the presence of SDC and secondly to mixed ionic electronic conductive (MIEC) nature of doped ceria. Similarly Tucker et al. [88] also reported high performance of 0.44 , 1.1 and $1.9 \text{ W} \cdot \text{cm}^{-2}$ at 600 , 700 and 750°C respectively. In [49] the MPD of a MS-SOFC with Ni-YSZ infiltrated anode has been reported as $0.548 \text{ W} \cdot \text{cm}^{-2}$ at 750°C . But compared to Ni-SDC [87], the MPD with Ni-YSZ is lower. This is also reflected in the combined polarization resistances, where for Ni-YSZ it is $0.44 \Omega \cdot \text{cm}^2$ [49] compared to $0.12 \Omega \cdot \text{cm}^2$ for SDC [87]. Another report [89] has utilized Ni-YSZ as anode functional layer, but a low MPD of $0.05 \text{ W} \cdot \text{cm}^{-2}$ has been reported at 700°C .

Gadolinium Doped Ceria (GDC) is another alternate to SDC due to its similar properties [90]. Rojek-Wockner et al. [91] reported a MPD of $0.88 \text{ W} \cdot \text{cm}^{-2}$ at 850°C with dry hydrogen with a MS-SOFC containing Ni-GDC as the impregnated anode. Figure 2.6 shows the I-V curve for this cell at different temperatures in dry hydrogen as fuel.

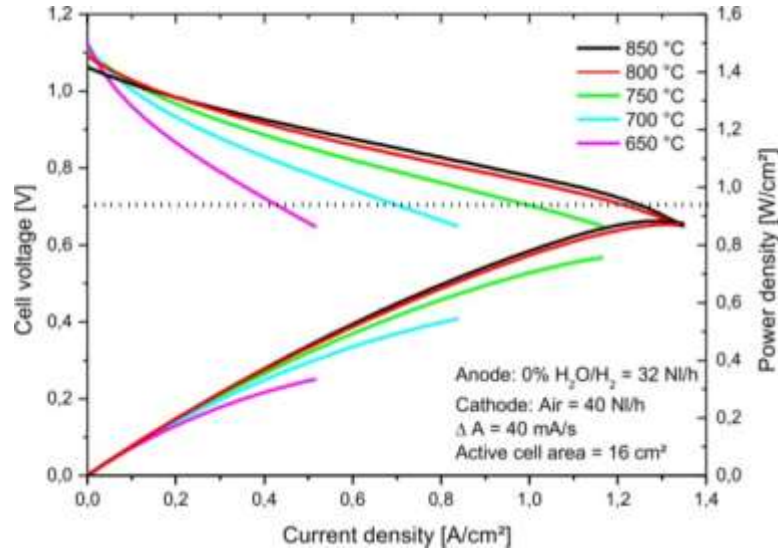


Figure 2.6: Current-voltage and current-power characteristics of a single metal-supported cell employing a Ni/GDC cermet anode[91]

Blennow et al. made comparison between GDC and ceria (CeO_2) as additive ceramic materials into nickel-based anode [59]. GDC showed a lower polarization resistance of $1.2 \Omega \cdot \text{cm}^2$ compared to ceria which was $5.1 \Omega \cdot \text{cm}^2$. They also reported that by adding GDC to nickel (10 wt%) the polarization resistance decreases to $0.12 \Omega \cdot \text{cm}^2$. Other than having a lower polarization resistance, MS-SOFC with Ni-GDC had a degradation of 5%/hr [6,59]. In [92] the durability of MS-SOFC with Ni-YSZ as anode was tested through thermal cycles between room temperature and 800°C after every 100 hours of operation. They reported that the cell maintained a MPD of $0.15 \text{ W} \cdot \text{cm}^{-2}$ at 800°C during the life test. They attributed this stability to stabilization of nickel by the addition of YSZ.

In [91] a comparison between Ni-YSZ and Ni-GDC is made using electrochemical impedance spectroscopy (EIS) and the area specific resistance (ASR). They concluded that the polarization arc appears at low frequencies for Ni-GDC anode which implies a gas diffusion limitation. In contrast, Ni-YSZ shows the polarization arc at low and medium frequencies, implying both gas diffusion limitation and charge transfer limitation. This is expected as GDC is a MIEC and can contribute to the conduction of electron to the active sites.

As mentioned earlier, nickel containing anode can go through volume changes during redox cycling causing physical defects in the cell [3,6 ,7]. Intuitively, cells with stand-alone anode functional layer (AFL) are more susceptible to this than cells in which a porous scaffold is

infiltrated with anode catalyst particles [46]. Bae et al. [93] used YSZ ceramic material as porous backbone layer which was infiltrated by 8-24 wt% nickel. However, due to poor electronic conduction of YSZ other materials have been tried as the anode scaffold as well. For example, in [94] $\text{La}_{0.4}\text{Sr}_{0.4}\text{Fe}_{0.03}\text{Ni}_{0.03}\text{Ti}_{0.94}\text{O}_3$ (LSFNT) was used as the scaffold with Ni-GDC as the anode catalyst. Nielsen et al. [94] reported that LSFNT showed a higher redox stability compared to a YSZ scaffold and also led to a MPD of 0.77 W.cm^{-2} at 750°C . This cell showed a degradation of $0.15 \text{ W.cm}^{-2}/1000$ hour in a durability test. In [95], SS-430L porous structure was impregnated with 10wt% loading of Ni catalyst. In Figure 2.7 SEM image has been taken for single metal support cell along with infiltrated anode and cathode catalysts.

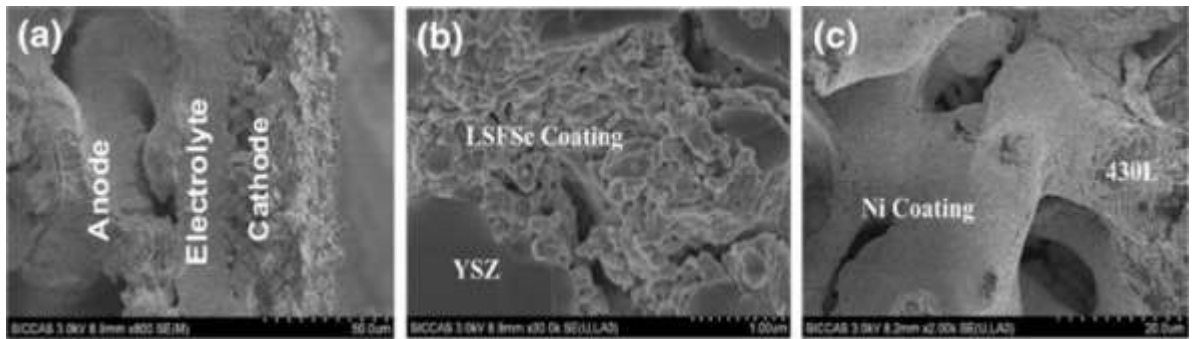


Figure 2.7: SEM images of (a) MS-SOFC, (b) LSFSc-YSZ cathode, (c) Ni-430L anode. [95]

As it can be seen in the above Figure 2.7, YSZ electrolyte is fully dense. For these cells the MPDs at $650, 700, 750$ and 800°C were $0.193, 0.418, 0.636$ and 0.907 W.cm^{-2} in humidified hydrogen. Figure 2.8 displays I-P-V plot for these cells.

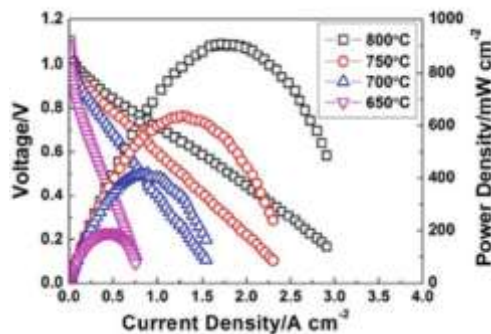


Figure 2.8: I-P-V characteristics for MS-SOFC [95]

Furthermore, in figure 2.9 impedance spectra measurement has been taken for this cell, and it is observed that the total polarization resistance losses of this cell are higher than ohmic resistance loss. Consequently, the polarization resistance dominates the cell performance.

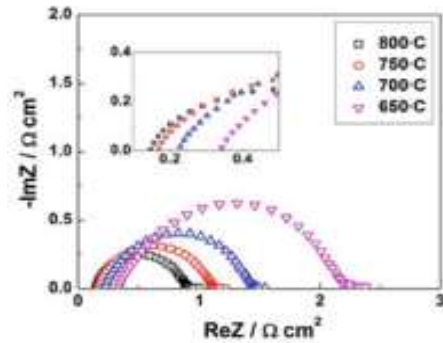


Figure 2.9: Impedance spectra at open circuits for MS-SOFC [95].

The comparison between infiltrated SDC-430L [96] (SDC loading = 10 wt%), Ni-430L [94] and Ni-SDC-430L [97] as anode catalysts has been made in terms of MPD, as well as polarization and ohmic resistances. By using infiltrated SDC-430L as anode catalyst, it has been reported that the MPD of this anode catalyst is higher than Ni-30L which is $0.94 \text{ W}\cdot\text{cm}^{-2}$ at 800°C under 3% humidified hydrogen fuels and dry air [96]. In contrast, the polarization and ohmic resistances of Ni-430L anode catalyst are very high compared to SDC-430L anode catalyst [96]. Figure 2.10 shows I-P-V and Nyquist plots of infiltrated SDC-430L anode catalyst used in single MS-SOFC at different temperature.

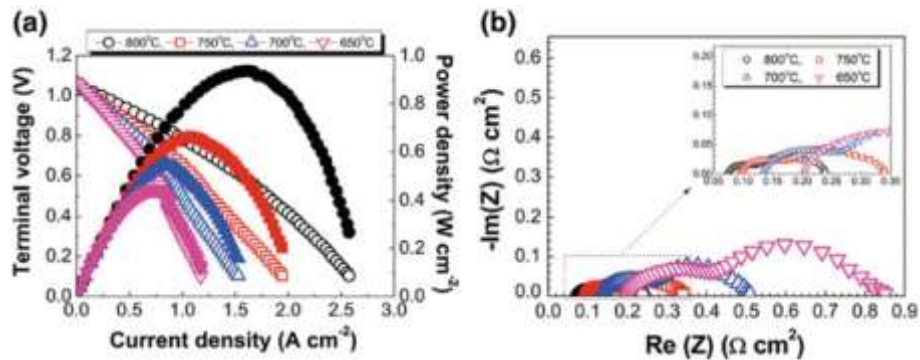


Figure 2.10: Electrochemical characteristics of a single cell measured at 650–800°C: (a) I–P–V characteristics, (b) Impedance spectra [96]

Based on Nyquist plot of infiltrated SDC-430L anode catalyst the polarization resistance dominates the cell performance. Stability measurement has been made at 650°C for MS-SOFCs with infiltrated SDC-430L as anode catalyst [12]. Figure 2.11 displays the stability measurement of this cell, and the authors concluded that infiltrated SDC-430L as anode catalyst is more stable than infiltrated Ni-430L anode catalyst. This cell shows good stability, which means that by utilizing SDC as the anode, catalyst coarsening and interdiffusion problems can be addressed.

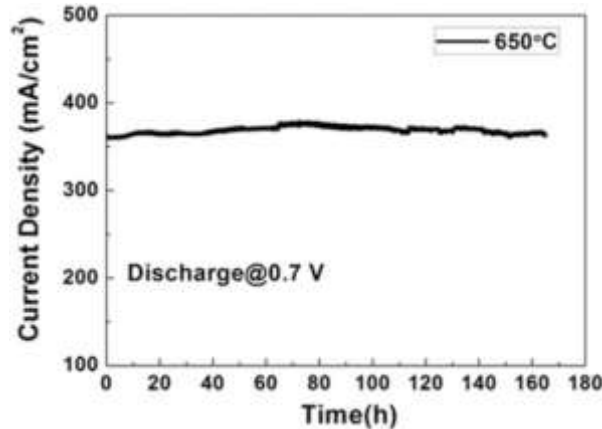


Figure 2.11: Stability of the single cell with used infiltrated SDC-430L as anode catalyst measured at 650°C [12].

In comparison to infiltrated SDC-430L and Ni-430L anode catalysts, Ni-SDC-430L has shown higher MPDs at 600, 650, 700, 750 and 800°C which are 0.4, 0.68, 0.92, 1.09 and 1.23 W.cm⁻², respectively [93]. Figure 2.12 shows MPD values of infiltrated Ni-SDC-430L as the anode catalyst in a single cell at different temperatures

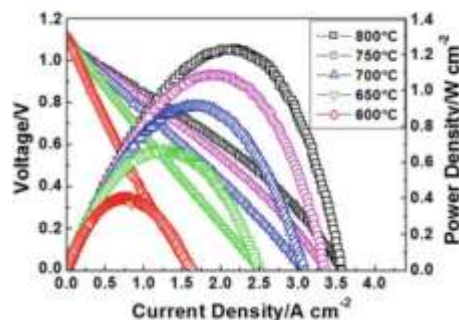


Figure 2.12: I-P-V characteristic for infiltrated Ni-SDC-430L used in MS-SOFC[96].

Further, the polarization resistance values of Ni-SDC-430L has been determined by impedance spectra at 800, 750, 700 and 650°C, which are 0.12, 0.13, 0.16 and 0.22 Ω.cm²,

respectively. The ohmic resistance of infiltrated Ni-SDC-430L in single cell has been observed as close to polarization resistance values, which are 0.12, 0.15, 0.19 and 0.26 $\Omega \cdot \text{cm}^2$ at 800, 750, 700 and 650°C, respectively [97]. Hence, infiltrated Ni-SDC-430L as anode catalyst is characterized by the polarization and ohmic resistances [97]; whereas, infiltrated Ni-430L [97] or SDC-430L [95] are characterized by mostly polarization resistance. Figure 2.13 shows a Nyquist plot of Ni-SDC-430L at different temperatures.

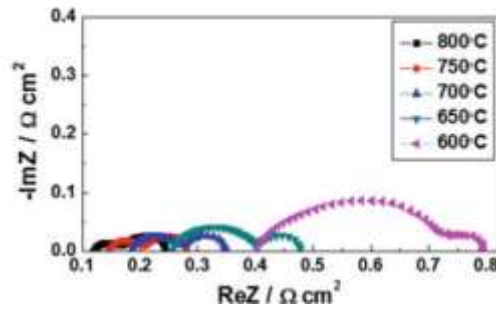


Figure 2.13: Impedance spectra for infiltrated Ni-SDC-430L used in MS-SOFC [95].

Although addition of YSZ or doped ceria can increase the performance of Ni cermet anode[6], another issue with the use of nickel is the coarsening of nickel particles during operation. For a MS-SOFC infiltrated with Ni-SDC during a durability test of 1,500 hours only 1.3%/1000-hour degradation was observed. However it can be seen in Figure 2.14 that after only 175 hours of operation there is significant change in the microstructure of the Ni-SDC anode [98]. Figure 2.14 shows SEM image of anode structure before and after 175 hours operation.

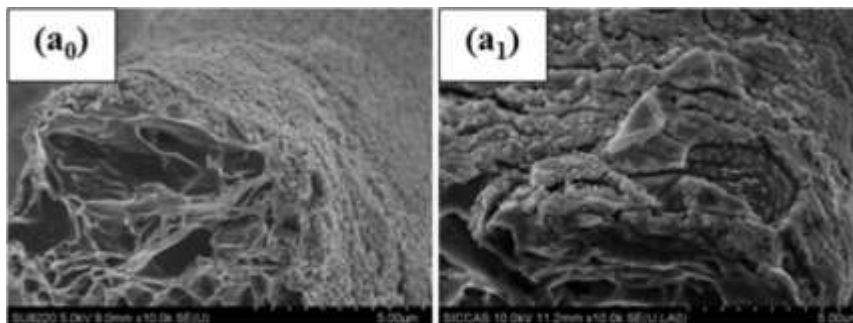


Figure 2.14: SEM image of MS-SOFC with Ni-SDC as the functional anode. (a₀) before cell operation and (a₁) picture after cell operation of 175 hours at 700°C[98].

Even though nickel has been very popular as an anode catalyst, due to its shortcomings other catalysts have also been investigated. A research group from Shanghai Institute of Ceramic-Chinese Academy of Science [99-101], has reported anode materials which do not have nickel in them. A MS-SOFC with $\text{Sr}_2\text{Fe}_{1.5}\text{Mo}_{0.5}\text{O}_{6-d}$ (SFMO) as anode had an area specific resistance and MPD of $0.11 \Omega\cdot\text{cm}^2$ and $0.81 \text{ W}\cdot\text{cm}^{-2}$ at 800°C , respectively, for a 16 wt% anode loading [100].

Comparison between (SFMO)[100], $\text{La}_{0.6}\text{Sr}_{0.4}\text{Fe}_{0.9}\text{Sc}_{0.1}\text{O}_{3-d}$ (LSFSc) | YSZ[101] and $\text{La}_{0.6}\text{Sr}_{0.4}\text{Fe}_{0.9}\text{Sc}_{0.1}\text{O}_{3-d}$ | LSGM[99] can be drawn in terms of polarization resistance and MPD. It has been observed that (SFMO) has a lower polarization resistance than (LSFSc)| YSZ and LSFSc| $\text{La}_{0.9}\text{Sr}_{0.1}\text{Ga}_{0.8}\text{Mg}_{0.2}\text{O}_{3-d}$ (LSGM), which are 0.11 [100], 0.21 [101] and 0.90 [99] $\Omega\cdot\text{cm}^2$ at 800°C , respectively; the MPD, intuitively, followed the inverse trend to that of area specific resistance, where it was highest for SFMO. Low performance with LSGM can be attributed to its low ionic conductivity compared to YSZ. To enhance the performance of LSFSc| LSGM system copper was added to the system [99]. The area specific resistance reduced to $0.58 \Omega\cdot\text{cm}^2$ and the MPD increased from 0.18 to $0.54 \text{ W}\cdot\text{cm}^{-2}$. As a comparison to Ni-SDC as anode, an area specific resistance of $0.096 \Omega\cdot\text{cm}^2$ has been reported [87].

In another study, comparison between Ni-GDC and ruthenium(Ru)-GDC has been made [102]. Ru-GDC has a superior performance compared to Ni-GDC. Figure 2.15 shows polarization curves and Nyquist plots for the two samples.

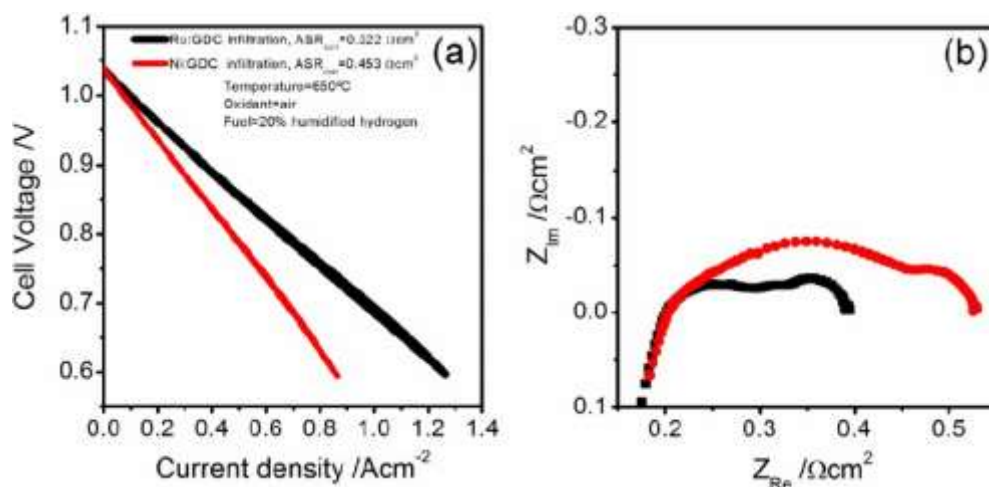


Figure 2.15: (a) Polarization curves and (b) Electrochemical impedance spectra of the Ru:GDC and the Ni:GDC infiltrated MS-SOFCs [102].

Bischof et al. [103] studied the effect of Ni-GDC anode microstructure, thickness and surface roughness, and reported that optimizing the microstructure can increase the MPD of the cell from 0.9 to 1.25 W.cm⁻² at 700°C. Another metric of performance is the redox stability, in [104] it was reported that Ni-GDC anode cermet exhibits a higher redox stability than Ni-YSZ.

As a concluding remark, Ni based anode remains one of the superior choices for anode material in SOFC. Michael tucker et al. [105] demonstrated this by using a Ni-SDC impregnated anode in MS-SOFC to assess the prospect of internal reforming of carbon containing fuel. For example, they reported that with ethanol/water blend and anhydrous ethanol, they observed a MPD of 1.0 W.cm⁻² and 1.4 W.cm⁻², respectively, at 700°C.

2.2.3 The Choice of Electrolyte

Electrolyte, is a critical component of SOFCs, and is responsible of conducting negative ions from cathode to anode to complete the circuit [32]. Requirements from an electrolyte are [1,6]:

1. High oxygen ion conduction.
2. Chemical and physical stability at high manufacturing and operating temperatures and in oxidizing and reducing atmospheres.
3. Ability to sinter to a full density to avoid any fuel or oxidant crossover.
4. Matching CTE to other cell components; however, mostly other component materials are developed for their CTE to match that of the electrolyte.

The first requirement can only come through the use of an oxide material with oxygen vacancies which can be generated through creating stoichiometric imbalance by use of dopants, some common examples are that of yttrium stabilized zirconia (YSZ) and doped ceria [51, 60, 106, 107].

There are several types of electrolyte such as YSZ, Strontium-Magnesium doped-Lanthanum Gallate (LSGM), Scandia Stabilized Zirconia (ScYSZ), Gadolinium Doped Ceria (CGO) or Samarium Doped Cerium (SDC). Although there are a few choices, the selection of material is mainly governed by its ability to attain full density using either a sintering process or a thermal spray deposition process.

2.2.3.1 Yttria Stabilized Zirconia (YSZ)

YSZ is the oldest and still one of the most common choices for electrolyte material because of its high oxygen ion conduction, insulation to electronic conduction and relatively lower cost [1, 32]. However, its ionic conductivity is lower than some other electrolyte materials, which leads to higher ohmic losses.

To decrease the ohmic resistance, the thickness of the electrolyte materials should be as thin as possible, so that it can have a lower resistance during operation. For example, with a 10 μm thick electrolyte, the area specific resistance at 800°C can be as low as 0.05 $\Omega\cdot\text{cm}^2$, compared to 0.75 $\Omega\cdot\text{cm}^2$ for a 150 μm thick YSZ electrolyte [1].

One of the key requirements, complete density of electrolyte, has been studied using two different processing routes, 1) use of thermal spray deposition and 2) high temperature sintering of electrolyte. Even though thermal spray deposition can be done at temperatures lower than that required for sintering, poor performance has been reported for electrolyte deposited through thermal spray deposition [43]. It has been reported that electrolyte deposited through plasma has a lower ionic conductivity than a sintered YSZ electrolyte [43]. The ionic conductivity of sintered YSZ was reported as 0.068 $\text{S}\cdot\text{cm}^{-1}$ compared to 0.021 $\text{S}\cdot\text{cm}^{-1}$ for plasma spray deposited YSZ [43]. Plasma spray deposition can also lead to increase in point defects, local hot spots and open pores, when a thick layer is deposited. In the same study [43] Open Circuit Voltage (OCV) plasma spray deposited YSZ was studied as a function of electrolyte thickness, where the OCV decreased with increasing thickness. This can be attributed to a higher ohmic resistance and also to the possibility of more local defects in thicker layers. As seen in Table 2.3, the leak through plasma deposited electrolytes increases with increasing thickness which signifies the presence of point defects leading to a low OCV. Figure 2.16 displays the OCV and power density results of cells with YSZ thickness from the study in [43].

Table 2.3: Thickness and leak rate values of different generations of plasma sprayed 8YSZ [43].

	Deposit Generations (1)	Deposit Generations (2)	Deposit Generations (3)	Deposit Generations (4)
Thickness (μm)	65 ± 8	50 ± 6	40 ± 4	35 ± 4
Leak rate (Pa.m/s)	5.2 ± 2.3	5.9 ± 0.9	5.6 ± 0.7	1.7 ± 0.2

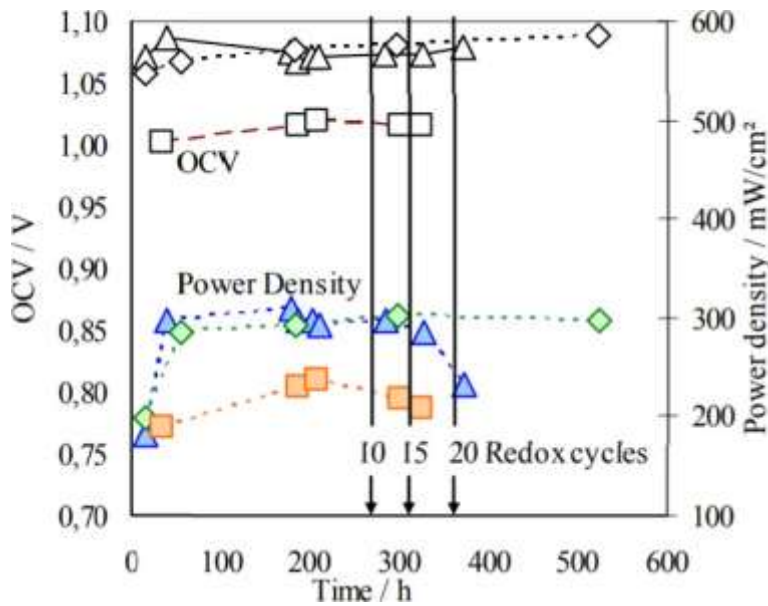


Figure 2.16: Open circuit voltage (OCV) and the power density (p) of different generations of cells tested under redox cycling Generation1 ■ Generation 2 ▲ Generation3 ◆ [43]

Another work [60], reports similar results concluding that the OCV and MPD of cells with plasma spray deposited YSZ is lower than that of sintered YSZ. In [86], the power density and cell voltage have been measured for co-sintered YSZ at 700°C which are above 1.2 Wcm^{-2} and above

1 V respectively. Figure 2.17 displays these results.

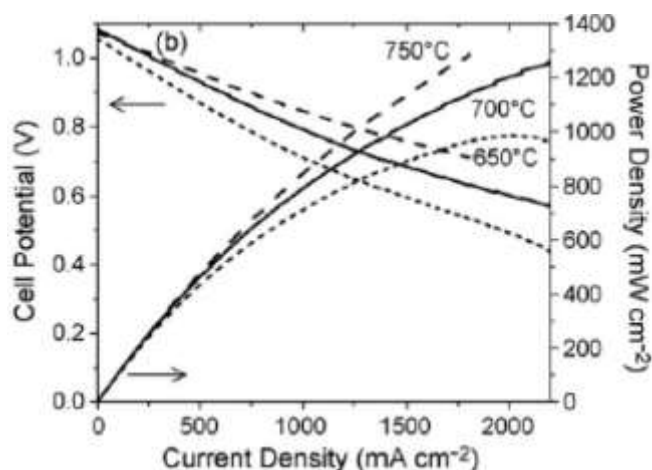


Figure 2.17: Performance of MS-SOFC with YSZ electrolyte obtained by co-sintering [86].

It appears that using sintering of YSZ can enhance the performance, however sintering has its own challenges. Particular to MS-SOFC is the sintering atmosphere. To protect the metal support from oxidation the sintering atmosphere should be either inert or reducing. The OCV for co-sintered YSZ under reducing atmosphere (5% H₂/95% N₂) at 1300°C has been recorded in multiple articles which have similar OCV values in the range of 1.0-1.12 V at 700°C [46, 49, 51, 87, 88, 89, 90, 98, 100, 108, 110]. In contrast, an OCV of 0.96 V at 823°C is reported for cells in which thermal spray deposition was used for electrolyte [111]. The authors of [111] concluded that this low OCV was because of a high leak rate. In another work, Franco et. al. [112] reported that by optimizing the thickness and layers of electrolyte deposited using a physical vapor deposition (PVD), the OCV of the cells range between 0.95-1.1V.

2.2.3.2 Doped Ceria

Doped ceria is known for its mixed ionic electronic conducting nature which characterized by a higher conductivity than YSZ. The MIEC nature is attributed to the transition of cerium between +4 to +3 oxidation states [11]. This brings its own challenges of instability during sintering at high temperatures and chances of internal short-circuit at operation above 600°C [11]. However, at intermediate operation temperature this transition of oxidation states can be reduced enhancing the cell life and performance [32]. The two common types of doped ceria used are gadolinium doped ceria (GDC) and samarium doped ceria (SDC). Although the concept of doped ceria is very attractive, it presents a challenge when co-sintered with metal support in MS-SOFCs. The sintering of MS-SOFC needs to be in an inert or

reducing atmosphere to avoid oxidation of metal support. High sintering temperature in a non-oxidizing atmosphere can lead to reduction of doped ceria, change of +4 oxidation state to +3 for ceria, which is coupled with crystal structure change which can induce physical stress and defects in the sintered samples [113].

One approach to mitigate or reduce the reduction of doped ceria is to reduce the sintering temperature for doped ceria. It has been reported that dopants, like copper, can act as sintering aid for doped ceria [114, 115, 116] effectively reducing the sintering temperature. Another way of avoiding high temperature sintering is the use of thermal spray deposition methods, such as Pulsed Laser Deposition (PLD), Magnetron Sputtering (MS) and Plasma Spray Deposition (PSD) which can fabricate ceria-based electrolyte at lower temperature [1]. In [116] the MPD of a MS-SOFC with a GDC electrolyte was reported to be 0.35 W.cm^{-2} at 600°C ; this low MPD is attributed to the possibility of electronic conduction through the electrolyte.

For SDC, as shown in Figure 2.18, the measured open circuit voltage (OCV) is lower than the theoretical OCV [123].

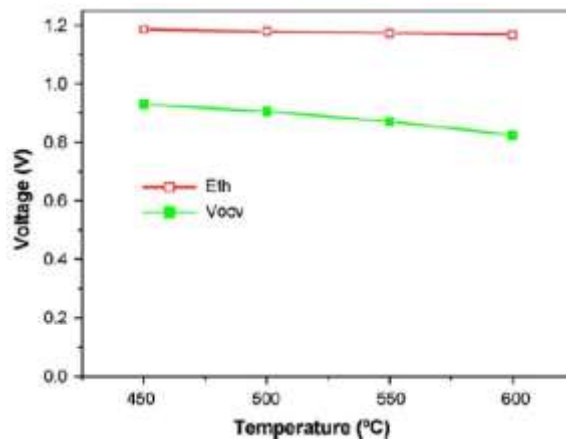


Figure 2.18: Theoretical open circuit voltage (Eth) and measured open circuit voltage V OCV over 450–600°C [123].

One way of reducing the conduction of electrons through electrolyte is the use of a barrier layer, which blocks the flow of electrons and only oxygen ions to pass through, on one side of the electrolyte. In [117, 118] scandium stabilized zirconia (ScSZ) has been used as a barrier with SDC electrolyte. Figure 2.19 shows cell performance of these cells in comparison to cells with just SDC as electrolyte.

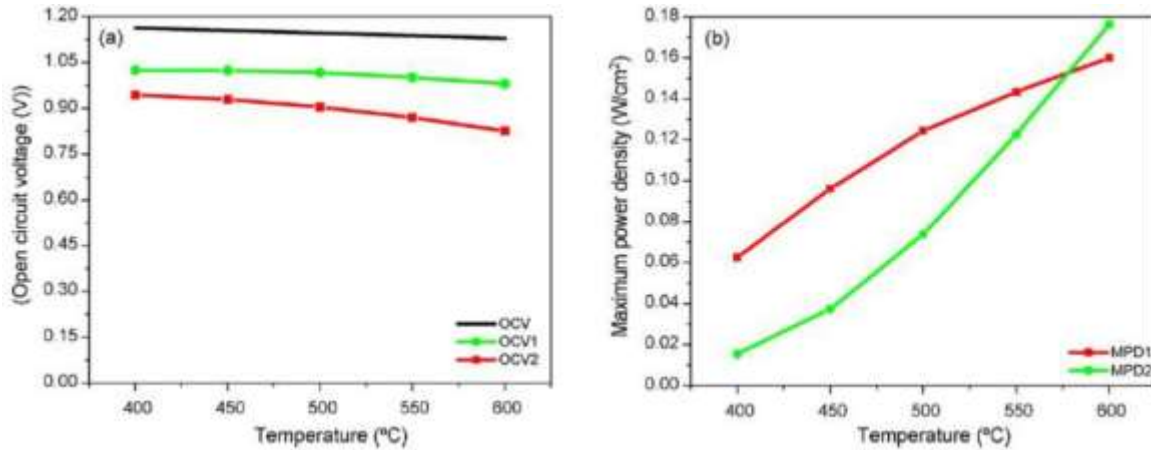


Figure 2.19: comparison of OCV of cells with bi-layered ScSZ-SDC as electrolyte (OCV1) and cell with only SDC as electrolyte (OCV2); b) comparison of MPD of cell with bi-layered ScSZ-SDC as electrolyte (MPD1) and cell with just SDC as electrolyte (MPD2) [117].

2.2.3.3 Scandia Yttria Stabilized Zirconia (ScYSZ)

It is one of zirconia-based electrolyte mixed with yttria. In [59, 124, 125], the OCV of MS cell with ScYSZ as a co-sintered electrolyte was reported in the range of 1.1 to 1.13 V.

In a different study, in order to reduce or avoid the oxidation of metal substrate, Wang et al. [126] have used very low pressure plasma spraying (VLPPS) method to fabricate scandia-stabilized zirconia electrolyte. They have reported a MPD and OCV for this cell at 750°C of 1112 mW.cm⁻² and 1.07 V, respectively.

2.2.3.4 Strontium- and Magnesium-Doped Lanthanum Gallate (LSGM)

In comparison to YSZ and ScSZ, LSGM has a higher ionic conductivity [11]; however, it has also been reported that LSGM reacts with chromia [119] and Ni-Fe alloys [120]. However, LSGM has been used as electrolyte because of its high oxygen ion conduction at low temperatures [41]. In [121] LSGM formed through plasma spray deposition exhibited an OCV and MPD of 1.0 V and 0.48 W.cm⁻², respectively, at 750°C. In another study the MPD and OCV for a LSGM electrolyte cell at 750°C was reported as 0.716W.cm⁻² and 0.9881 V, respectively [122].

2.2.4 The Choice of Cathode

The cathode is responsible for receiving electrons and oxygen, performing oxygen reduction and transporting reduced oxygen (oxygen ions) to the electrolyte. This requires a few qualities from the

cathode material:

1. Electronic conduction to facilitate the incoming electrons.
2. Activity towards oxygen reduction reaction
3. Conduction for oxygen ions
4. Chemical stability in different atmospheres, particularly in oxidizing atmosphere
5. Chemical inertness towards electrolyte material

To provide functionality towards oxygen reduction and conduction it is intuitive that cathode material will be made from an oxide. Although there are many choices of cathode material, all of them face the same problem in their application in MS-SOFCs. As mentioned earlier, when co-sintering is employed to avoid oxidation of metal support the sintering needs to be done in a non-oxidizing atmosphere. Non-oxidizing atmosphere and high temperature can lead to reduction of metal oxides in the cathode material, thereby changing their crystal structure and chemical activity [6]. Another primary challenge with most cathode materials is their activity towards YSZ electrolyte [11]. It has been reported that LSM cathode can react with YSZ electrolyte at high temperatures to form insulating oxides like $\text{La}_2\text{Zr}_2\text{O}_7$ and SrZrO_3 [127]. As described in section 2.3 “the choice of metal support” chromium can form volatile compounds like CrO_3 and $\text{CrO}_2(\text{OH})_2$ that can transport into the cathode and react with the cathode material [128]. There are reports of use of a thin ceramic coating on metal support to reduce the formation and vaporization of chromium compounds [32, 129].

As mentioned earlier, most cathode materials can react with YSZ electrolyte and form insulating phases leading to decreased performance. There are published reports of use of a thin barrier layer of GDC which can mitigate direct contact of YSZ with cathode material. In [112, 124, 133], GDC has been used as a diffusion barrier layer between YSZ, and Cobalt and Strontium containing cathode catalyst, such as LSCF and LSM. The GDC layer was applied through Physical Vapor Deposition (PVD) and spin coating. With a GDC diffusion barrier layer the ASR was recorded as $0.27 \Omega \cdot \text{cm}^2$ at 650°C .

Cobalt content in itself also has effect on the performance of cathodes [137, 138]. For example, it is reported that a cobalt content of 40 mole % in the base crystal structure leads to lower ASR. Cobalt higher than 40% can lead to increased ASR and also the formation of insulating cobalt phases when in contact with YSZ.

To bypass the degradation caused by reaction of YSZ with lanthanum, cobalt and strontium, Zhan et al. [49] used oxide of bismuth-erbium and silver (ESB-Ag) composite. For this MS-SOFC they reported an ASR of $0.09 \Omega \cdot \text{cm}^2$ and MPD of $0.568 \text{ W} \cdot \text{cm}^{-2}$ at 750°C . In [108], ESB-Ag was screen printed on a YSZ and a scandia stabilized zirconia (SSZ) electrolytes; it was reported that cell with SSZ shows a lower ASR of $0.07 \Omega \cdot \text{cm}^2$ and a higher MPD of $1.55 \text{ W} \cdot \text{cm}^{-2}$ at 750°C , compared to the cell with YSZ as electrolyte for which the ASR was $0.10 \Omega \cdot \text{cm}^2$ and MPD was $1.3 \text{ W} \cdot \text{cm}^{-2}$ at 750°C .

In another approach to mitigate the reaction between cobalt and YSZ, cobalt was replaced with chromium [6,139] in the form of $\text{La}_{0.8}\text{Sr}_{0.2}\text{Cr}_{1-x}\text{Mn}_x\text{O}_{3-\delta}$ (LSCrM). In these studies the chromium content was varied between 0 and 80 mol%. In the same work LSCrM and ruthenium (5mol%) as a cathode composite were also studied. Table 2.4 shows the comparison of cathodes containing varying content of chromium

Table 2.4: ASR for different LSCrM cathodes calculated using ASR plots at 900°C [6,139].

Cathode	ASR ($\Omega \cdot \text{cm}^2$) (sintered in N_2)	ASR ($\Omega \cdot \text{cm}^2$) (sintered in air)
LSM	~ 5.0	~ 0.1
$\text{La}_{0.8}\text{Sr}_{0.2}\text{Cr}_{0.2}\text{Mn}_{0.8}\text{O}_{3-d}$	~ 2.5	~ 4.5
$\text{La}_{0.8}\text{Sr}_{0.2}\text{Cr}_{0.5}\text{Mn}_{0.5}\text{O}_{3-d}$	~ 0.2	~ 0.2
$\text{La}_{0.8}\text{Sr}_{0.2}\text{Cr}_{0.8}\text{Mn}_{0.2}\text{O}_{3-d}$	~ 3.16	~ 0.23
$\text{La}_{0.8}\text{Sr}_{0.2}\text{Cr}_{0.45}\text{Mn}_{0.5}\text{O}_{3-d}/\text{Ru}$ 0.05	~ 0.2	~ 0.15

There are two approaches to incorporate cathode in a MS-SOFC; sintering cathode on the cell and infiltrating cathode in a porous cathode scaffold which is sintered with rest of the cell.

2.2.4.1 Cathode Sintering

Cathode sintering is when a stand-alone layer of cathode is sintered to bond with the rest of the cells. As discussed earlier, in the case of MS-SOFCs, this brings about many challenges, for instance high temperature of sintering in oxidizing atmosphere can lead to undesired oxidation of metal support. A possible solution is to use cathode materials which can be sintered at low temperatures, below 1000°C [41]. This limitation can reduce the choice of cathode materials that can be used. Poor cathode performance in term of polarization (ASR of $0.25 \Omega \cdot \text{cm}^2$) was reported for metal supported cell with LSCF cathode when sintered below 1000°C to avoid excessive oxidation of the metal support surface [130]. In comparison to LSCF, when $\text{LaNi}_{0.6}\text{Fe}_{0.4}\text{O}_3$ (LNF) cathode was sintered at

1000°C a better performance was reported, with a MPD of 1.56 W.cm^{-2} at 800°C [41,131]. There are two types of cathode sintering which are in-situ sintering and ex-situ sintering.

2.2.4.1.1 In-Situ Sintering

In-situ sintering means that the cathode is sintered during cell testing process. This facilitates the sintering of cathode at somewhat high temperatures ($800\text{-}1000^\circ\text{C}$) in oxidizing atmosphere as the cathode is sealed away from the metal support (given the metal support is on the anode side). There are many research published on the use of in-situ sintering for cathode material [48, 59, 124, 132, 133]. In [48] a comparison is made between LSCF, LSCF/GDC, LSC and LSC/GDC when the cathode was in-situ sintered at 850°C . In this article it was reported that LSC/GDC has the highest performance followed by $\text{LSC} > \text{LSCF/GDC} > \text{LSCF}$. However, the authors of the article also reported that LSC/GDC has a high CTE, 18.6 ppm.K^{-1} , compared to other cell components which can lead to cell warping and layer delamination. In another study, the long term performance and electrochemical properties of in-situ sintered ($\text{SmBa}_{0.5}\text{Sr}_{0.5}\text{Co}_2\text{O}_{5+\delta}$ 50 wt% of (SBSCO)/ $\text{Ce}_{0.9}\text{Gd}_{0.1}\text{O}_{2-\delta}$ 50 wt% of (CGO91)) (SBSCO:50) as cathode composite was reported by Irvine et al.[134]. They report that by in-situ sintering the cathode at 750°C instead of 700°C the ASR can be decreased from $0.031 \text{ }\Omega\text{.cm}^2$ to $0.014 \text{ }\Omega\text{.cm}^2$. Figure 2.20 shows the ASR of SBSCO versus time for different in-situ sintering temperatures ($650, 700, 750^\circ\text{C}$).

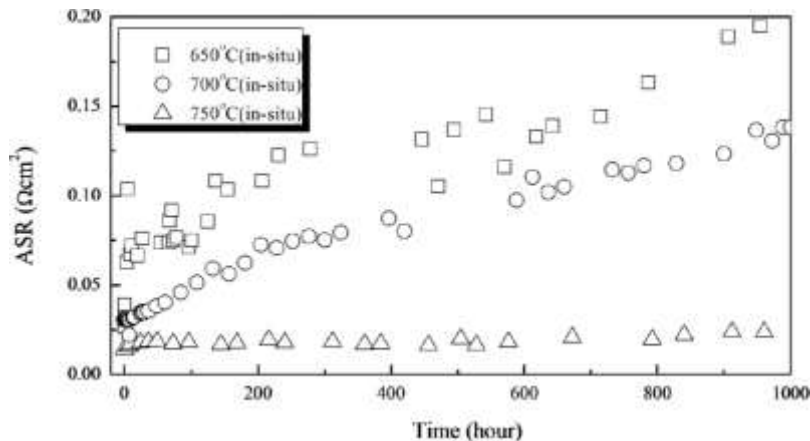


Figure 2.20: ASRs of in-situ SBSCO cathode measured at various temperatures ($650, 700$ and 750°C) over 1000 hours [134].

In a different study, Bae et al. [135] have compared in-situ sintered SBSC50 and $\text{Ba}_{0.5}\text{Sr}_{0.5}\text{Co}_{0.8}\text{Fe}_{0.2}\text{O}_{3-\delta}$ (BSCF) cathodes. They found that the presence of barium can enhance the sinterability and lower the required sintering temperature. They report that BSCF shows a higher ASR of $0.05 \Omega \cdot \text{cm}^2$ compared to SBSC50 (ASR of $0.02 \Omega \cdot \text{cm}^2$). In [136], different cathode materials (LSM, LSF, LSCF, SSC40, BSCF and SBSC50) are compared to electrolyte-cathode adhesion for in-situ sintering below 900°C . They reported that below 900°C , SBSC50 and BSCF have the highest adhesion compared to other cathodes. In [154], the cathode, $\text{Ba}_{0.5}\text{Sr}_{0.5}\text{Co}_{0.8}\text{Fe}_{0.2}\text{O}_{3-\delta}$ (BSCF)/GDC was screen printed on a dense ScSZ /NiO-ScSZ anode assembly, and a MPD at 750°C of $1.0 \text{ W} \cdot \text{cm}^{-2}$ was reported.

2.2.4.1.2 Ex-Situ Sintering

In this type of sintering, the cathode layer is sintered prior to testing to enhance the adhesion between cathode and electrolyte. The sintering atmosphere is chosen to be inert (argon) to avoid oxidation of the metal support. There are reports of ex-situ sintered cathode MS-SOFC in literature [140, 141, 142, 143]. Since the sintering is done in inert atmosphere, there is a possibility for the cathode material to change its structure when exposed to ambient (oxidizing atmosphere) after sintering. Menzler et al. [143] shows a comparison of LSCF, LSC, LSF and $\text{La}_{0.58}\text{Sr}_{0.4}\text{CoO}_{3-\delta}/\text{Ce}_{0.8}\text{Gd}_{0.2}\text{O}_{2-\delta}$ (LSC/GDC), in terms of their performance and stability. They reported that all cathode materials show poor stability when exposed to ambient atmosphere after sintering except for LSC/GDC which can be stored for up to 2 days without any apparent physical degradation. Another study by Udomsilp et al. [140] also reported that between LSCF and LSC, LSCF shows more stability when exposed to ambient atmosphere after ex-situ sintering in argon.

Brama et al. [141] also conducted a study to assess the effect of ex-situ sintering on the adhesion and performance of LSCF cathodes. Figure 2.21 shows the IVP curve for their sample at different temperatures. In this figure, the current density was measured at temperatures between 655 and 858°C for ex-situ sintered LSCF; power densities of $940 \text{ mW}/\text{cm}^2$ were attained above 800°C .

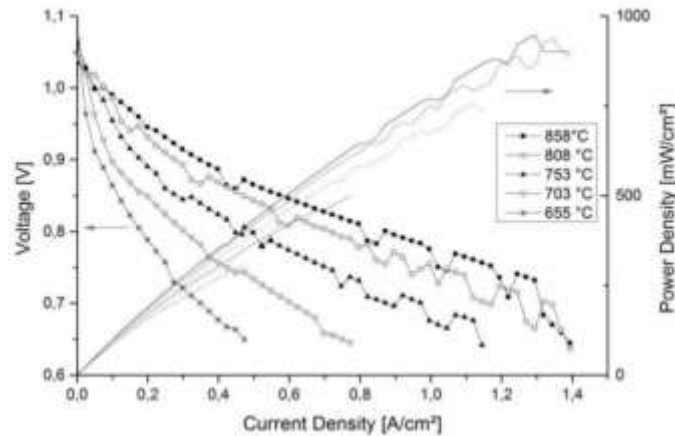


Figure 2.21: I/V-curves and resulting power density of an MSC with ex-situ sintered LSCF cathode at different operating temperatures [141]

2.2.4.2 Cathode Infiltration

In cathode infiltration, a porous cathode scaffold is infiltrated with a cathode catalyst solution prior to testing. The porous scaffold is sintered at the same time of the electrolyte/anode assembly in reduced or inert atmosphere. Using this approach, the sintering of cathode and related issues can be avoided [41]. This approach also leads to a dispersion of small catalyst particles throughout the porous scaffold structure which mitigates the physical strain put on a cell due to mismatch in CTE of standalone layers. The catalyst solution can be an aqueous salt solution of catalyst or a molten salt of the catalyst. Once infiltrated it can be thermally decomposed to form the required catalyst [144]. There are several reports dealing with this approach, most of these are discussed briefly below.

In [97], for the cathode, $\text{La}_{0.6}\text{Sr}_{0.4}\text{Fe}_{0.9}\text{Sc}_{0.1}\text{O}_{3-\delta}$ (LSFSc) is infiltrated in a YSZ scaffold; the mass loading of LSFSc was optimized by measuring the polarization resistance. Figure 2.22 shows the variation in polarization resistance with the mass loading of LSFSc. It can be seen that 30 wt% loading is an optimum point.

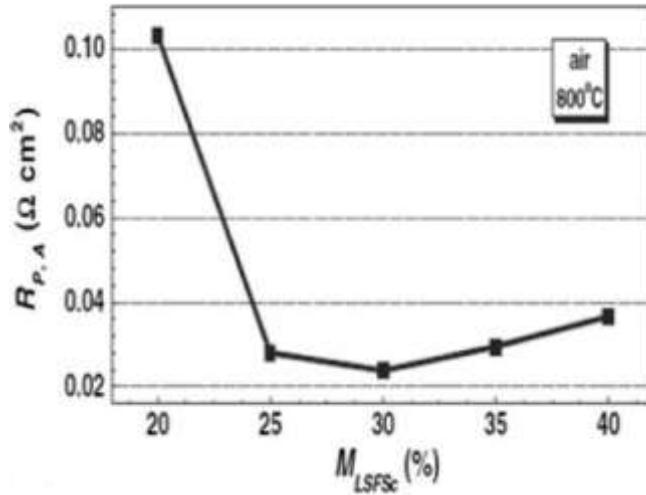


Figure 2.22: the polarization resistance for different loading percentage of infiltrated LSFSc [97].

In another study, comparison between LSC, LSCF and $\text{SmBa}_{0.5}\text{Sr}_{0.5}\text{Co}_{2.0}\text{O}_{5+\delta}$ (SBSC) was made when these cathodes were infiltrated in a $(\text{ZrO}_2)_{0.89}(\text{Sc}_2\text{O}_3)_{0.1}(\text{CeO}_2)_{0.01}(\text{SSZ})$ porous cathode scaffold [145]. Figure 2.23 shows the polarization resistance of these cathodes, in which SBSC shows the lowest polarization. Low polarization of SBSC is attributed to its large capacity for surface adsorption/desorption of oxygen [146]. LSC-SSZ has a lower polarization resistance than LSCF-SSZ; this is due to high electronic and ionic conductivity of LSC at 800°C [147].

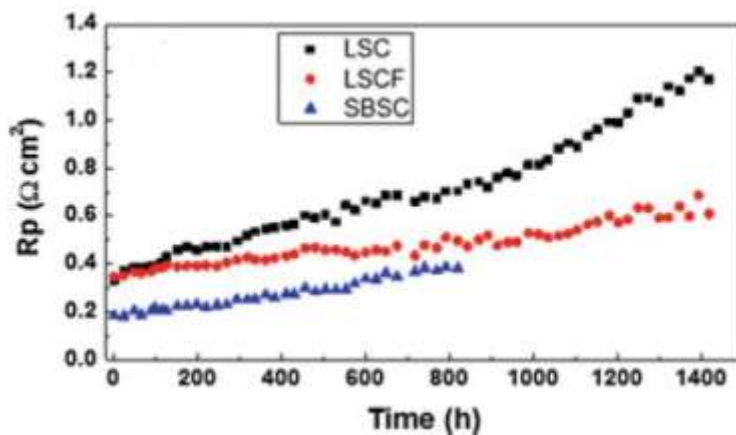


Figure 2.23: Polarization of LSC-SSZ, LSCF-SSZ and SBSC-SSZ at 700°C [145].

In another study on the MPD and combined polarization resistance for MS-SOFC, SBSC infiltrated in SSZ porous cathode has been reported [148]. Figure 2.24 shows the MPD and impedance spectra for a single cell.

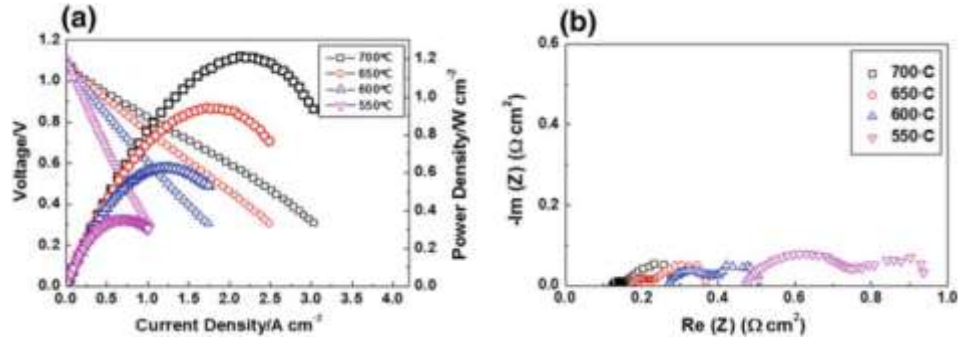


Figure 2.24: I–P–V characteristics, b Impedance spectra at different operating temperature from 550 to 700°C [148].

Zhan et al. [51] have used $\text{Sm}_{0.5}\text{Sr}_{0.5}\text{CoO}_3$ (SSC) SSC as cathode catalyst and porous YSZ as scaffold with single cell (MS-SOFC), ; they reported a MPD and ASR/polarization resistances at 750°C of 0.38 W.cm^{-2} and $2.28 \text{ } \Omega.\text{cm}^2$, respectively. Compared to the MPD and ASR of SSC, it has been reported that LSFSc shows higher MPD and lower ASR at 750°C, which are 1.09 W.cm^{-2} and $.037 \text{ } \Omega.\text{cm}^2$. However, LSFSc shows higher ASR at 650°C which is $0.155 \text{ } \Omega.\text{cm}^2$ [87]. In contrast with LSFSc [87] (single cathode cell), in [95], it has been recorded that LSFSc (single cathode cell) has lower MPD at 750°C than LSFSc (symmetrical cathode cell); which is 0.636 W.cm^{-2} , also it has lower ASR at 650°C compared to LSFSc (symmetrical cathode cell) which is $0.16 \text{ } \Omega.\text{cm}^2$.

$\text{Sr}_2\text{Fe}_{1.5}\text{Mo}_{0.5}\text{O}_{6-d}$ (SFMO) as an infiltrated cathode has also been reported [109, 149]. In [109] the ASR and MPD of the cell was reported as $0.09 \text{ } \Omega.\text{cm}^2$ and 0.56 W.cm^{-2} at 750°C, respectively. In [149] the ASR and MPD of the cell were as $0.1 \text{ } \Omega.\text{cm}^2$ and 0.136 W.cm^{-2} at 750°C, respectively.

In [148], SBSCo, as cathode, was infiltrated in a SSZ porous cathode scaffold with a SSZ electrolyte. This cell showed a MPD of 1.25 W.cm^{-2} at 700°C. In another study, a symmetrical cell with SBSCo infiltrated on both sides in a LSGM porous scaffold, and with LSGM electrolyte was investigated; after SBSCo infiltration the cell was calcined at 850°C. This cell showed a MPD of 1.5 W.cm^{-2} at 600°C [150]. The higher performance than the cell in [148] is attributed to the use of LSGM as the porous electrode scaffold for both anode and cathode sides for cathode and anode impregnation.

Tucker et al. [151] have made a comparison of 5 different material categories for cathode including perovskites, nickelates, praseodymium oxide, binary layered composites, and ternary layered composites. Similarly, they have also reported results on the loading of nickel-SDC as the anode catalyst. In all their cells, they have used either 10Sc1CeSZ or YSZ as the electrolyte. In conclusion, they report that with Ni-SDC (40wt% nickel) and praseodymium oxide (PrO_x) shows the highest performance in terms of power density. At 700°C cells with Ni-SDC as anode and PrO_x as cathode had a power density of 1.34 W.cm^{-2} when YSZ was the electrolyte and 1.56 W.cm^{-2} when SCSZ was the electrolyte. In continuation of this work, Tucker et al. have published a degradation study for cells containing Pr_6O_{11} as the cathode catalyst and Ni-SDC as the anode [152]. They report that for these cells, coarsening of Pr_6O_{11} particles and Cr poisoning of Pr_6O_{11} (their structure has metal support on both anode and cathode side) are the primary degradation mechanisms. A degradation rate of $2.3\%.\text{kh}^{-1}$ was reported.

In another study, Tucker [153] has conducted a study on using MS-SOFC for delivering power to a microelectronic LED driver and voltage boost circuits. In this study, he used 5 MS-SOFCs stacks. $\text{La}_{0.15}\text{Sr}_{0.85}\text{MnO}_{3-d}$ (LSM) has been infiltrated into porous YSZ scaffold. The MPD of this 5 stacks system has been recorded as 156 mW.cm^{-2} .

In conclusion, table 2.5 shows brief summary of cathode literate review

Table 2.5: Brief summary of cathode literate review [49, 133, 136, 143,148]

Cathode materials	Fabrication method	Area Specific Resistance (ASR) ($\Omega.\text{cm}^2$)	Maximum Power Density (MPD) (W.cm^{-2})
$(\text{Bi}_2\text{O}_3)_{0.7}(\text{Er}_2\text{O}_3)_{0.3} - \text{Ag}$ as composite cathode [49]	Tape casting for MS-Cell while screen printing and in-situ sintering for cathode	$0.09 \Omega.\text{cm}^2$ at 750°C	1.55 W.cm^{-2} at 750°C
$\text{La}_{0.58}\text{Sr}_{0.4}\text{Co}_{0.2}\text{Fe}_{0.8}\text{O}_3$ / $\text{Ce}_{0.9}\text{Gd}_{0.1}\text{O}_{3-d}$ as composite cathode [133]	Tape casting for MS-Cell while screen printing and in-situ sintering for cathode	$0.27 \Omega.\text{cm}^2$ at 650°C	1.14 W.cm^{-2} at 650°C
$\text{Ba}_{0.5}\text{Sr}_{0.5}\text{Co}_2\text{O}_{5-d}$ / $\text{Ce}_{0.9}\text{Gd}_{0.1}\text{O}_{1.9}$ (SBSC50) [136]	Tape casting for MS-Cell while screen printing and	$0.02 \Omega.\text{cm}^2$ at 800°C	0.50 W.cm^{-2} at 800°C

	in-situ sintering for cathode		
$\text{Ba}_{0.5}\text{Sr}_{0.5}\text{Co}_{0.8}\text{Fe}_{0.2}\text{O}_{3-d}$ (BSCF) [136]	Tape casting for MS-Cell while screen printing and in-situ sintering for cathode	$0.054\Omega\text{cm}^2$ at 800°C	0.65 Wcm^{-2} at 800°C
$\text{La}_{0.58}\text{Sr}_{0.4}\text{CoO}_{3-d}/\text{Ce}_{0.8}\text{Gd}_{0.2}\text{O}_{2-d}$ (LSC/GDC) [143]	Tape casting for MS-Cell while screen printing and ex-situ sintering for cathode	It is not provided	1.49 Wcm^{-2} at 800°C
$\text{SmBa}_{0.5}\text{Sr}_{0.5}\text{Co}_{2.0}\text{O}_{5+d}$ (SBSC) $(\text{ZrO}_2)_{0.89}(\text{Sc}_2\text{O}_3)_{0.1}(\text{CeO}_2)_{0.01}$ (SSZ) as electrolyte and porous scaffold [148]	Tape casting for MS-Cell while infiltration method for cathode	$.054\Omega\text{cm}^2$ at 700°C	1.25 Wcm^{-2} at 700°C

Chapter 3 Experimental Methodology and Equipment

In this chapter, the experimental procedures and approaches used in this thesis are presented in detail. This chapter comprises two main parts. In the first part, the fabrication method and the materials used for MS-SOFC fabrication are described; in addition, devices and techniques (co-sintering, XRD, SEM and electrochemical testing station) are also presented. The second part deals with the fabrication procedure of individual components, specifically, metal support, electrolyte, anode and cathode layers.

3.1 Experimental Approach, Devices and Methods Used for MS-SOFC

The first step was linked to the choice of metal support material which must be compatible with other cell components, especially the electrolyte. In this study, YSZ has been selected as the electrolyte with 430L stainless steel as the metal support because it has been seen that both are compatible with each other. In the second step, in order to avoid agglomeration and cracks on tape casted components (typically, electrodes, electrolyte, metal support), the tape casting procedure has been tuned by careful formulation of casting slurries. In the third step, to avoid cell warping and cracking during co-sintering and ex-situ sintering, particular attention was given to the tuning of co-sintering and ex-situ sintering temperature profiles, which are used for half MS-SOFC and cathode, respectively. Tuning of those sintering profiles was done by understating the shrinkage behavior of all cell components. In the fourth step, in order to have sufficient cathode infiltration for cathode catalyst, the porosity of ceramic structure; which acts as scaffold for cathode catalyst infiltration, has been formulated by comparing different percentage of porosity. The last step was linked to cell performance during operation.

3.1.1 Tape Caster

A tape caster has been used to spread a liquid suspension slurry as a flat form by using a doctor blade; the thickness of the tape cast has been adjusted via a doctor blade depending on the type of a suspension slurry and desired tape cast thickness. Figure 3.1 shows the tape caster used in this work with the doctor blade. Then, the casted slurry was dried at room temperature, until it was converted to solid state. Five types of slurries have been prepared for tape casting in order to fabricate a single cell: 1) 430L stainless steel support, 2) YSZ electrolyte, 3) porous YSZ, 4) anode transition and 5) cathode transition. The slurries preparation and tape casting procedures are presented in detail in section 3.2.

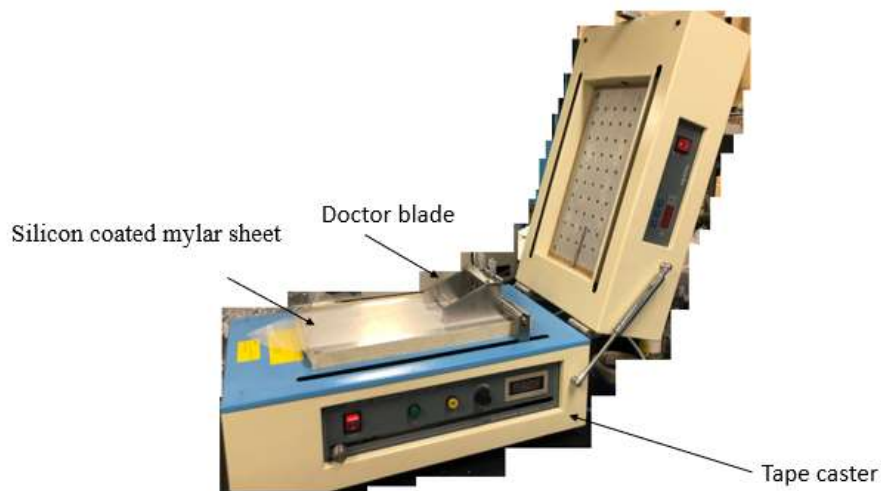


Figure 3.1: Tape caster and doctor blade

3.1.2 Co-Sintering

Co-sintering was carried out in a tubular furnace (MTI GSL-1500X tubular furnace) under controlled atmosphere. Co-sintering was used to shrink and densify dried tape casts by applying thermal energy. In other words, co-sintering was utilized to obtain solid layers for MS-SOFC half-cell structure, consisting of MS layer, transition layer and YSZ electrolyte. Two main types of half-cell structures have been co-sintered at 1325°C in reducing atmosphere (5% H₂/95% Ar). The difference between the two structure types is in the design of the cathode; in structure 1, a stand-alone cathode layer is deposited on the sintered half-cell, whereas in structure 2, a porous scaffold layer is co-sintered with the half-cell prior to impregnation of active cathode materials (more details are provided in section 3.2.2). After co-sintering of MS-SOFC half-cell for cell structure 1, LSCF as cathode layer is deposited and sintered on MS-SOFC half-cell at 1100°C in inert atmosphere. Details of the co-sintering procedure is provided in section 3.2.

3.1.3 X-ray Diffraction

X-ray diffraction has been utilized to determine crystal type and crystal lattice parameters for ceramic and perovskite or any kind of materials used in this work. It has also been used to measure crystal size of these materials. A Bruker D8 Focus X-Ray diffractometer, located in the Chemical Engineering Department at the University of Waterloo, was used. The powder of SBSCo, used as cathode catalyst was prepared for x-ray diffraction analysis, then the powder has been placed and distributed as smooth and flat surface in the sample holder before placing it on the sample holder tray. 8 samples can be loaded simultaneously in this tray, and this tray is connected to the X-ray diffraction device. 40 kV and 40 mA have been selected as a voltage and a current, respectively. CuK α radiation with a wavelength (λ) of 1.5425 Å has been utilized. Furthermore, the rotation angle for the sample holder has been set for 2 θ values in the range 20-90°. Peak positions and crystal structure have been identified using the Eva software.

3.1.4 Scanning Electron Microscopy (SEM)

SEM device has been used to scan the microstructure of some MS-SOFC half-cells before and after electrochemical tests. Energy- Dispersive X-Ray Spectroscopy (EDX) has also been utilized to analyze element inside single and half cells or to analyze the chemical characterization of MS-SOFC single and half cells. A SEM LEO 1530, SEM ZEiss Ultra Plus and ESEM, located at the Waterloo Advanced Technology Lab (WATLAB), have been utilized for SEM and EDX analysis. Sputtering equipment; which is also existed at WATLAB was used to coat MS-SOFC half and single cells with a 10nm thin gold layer. SEM images of various magnifications have been taken by Secondary Electrons (SE) and Back Scattered Electrons (BSE).

3.1.5 Electrochemical Testing

3.1.5.1 Assembly for MS-SOFCs

Electrochemical tests were carried out in a Fiaxell Open FlangesTM test setup, shown in Figure 3.2. Figure 3.2a represents how the assembly looks like when positioned on a furnace (with the cell in the bottom). Figure 3.2b shows the cell assembly when installing/removing the cell (the whole setup needs to be put upside down). The cell is placed on the diffuser (Figure 3.2c), as seen in Figure 3.2d.

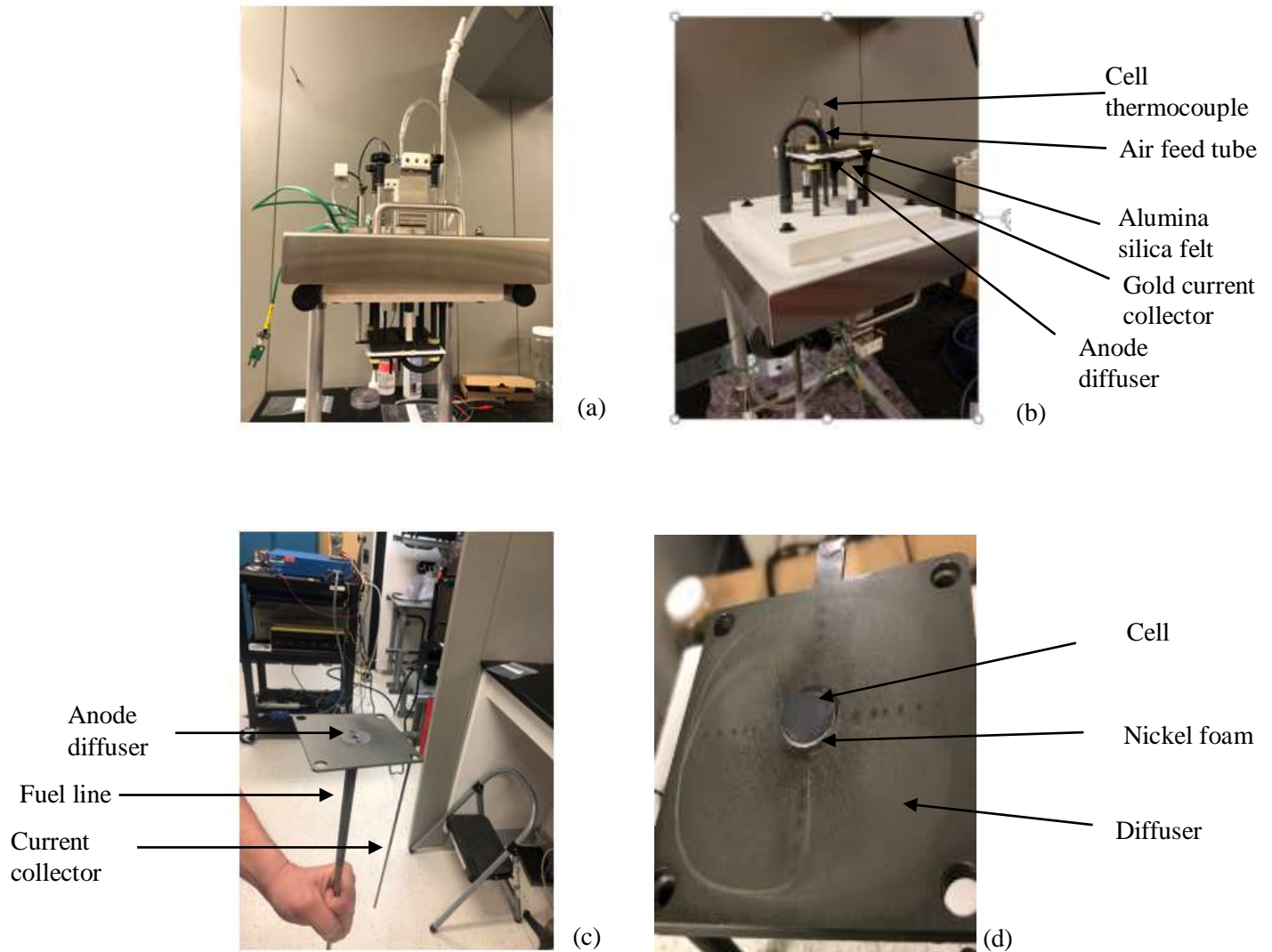


Figure 3.2: SOFC testing station

First, the diffuser (Figure 3.2c) is inserted in the main tube (fuel feed at anode side) and nickel rod (current collector) in the ceramic tube. Then a piece of nickel foam of similar size as the cell is punched, typically 5/8" or 15.88 mm in diameter. The nickel foam is then placed in the center of the diffuser, and the cell is placed on top of the nickel foam (as seen in Figure 3.2d); scotch tape (to be burned out during heating up) was used to attach them together. Then an alumina-silica felt has been punched with a hole size of 11.11mm (about the size of the cathode) and placed on the top of cell set. Next, gold mesh has been used and with similar cathode diameter to cover the cathode, so it can easily contact with the cathode. A small piece of scotch tape is utilized to attach the gold mesh with cathode prior to closing and compressing the

assembly. Then, in order to ensure electrical insulation, a second alumina silica felt is placed on top of the first alumina silica felt and gold mesh/current collector. Finally, the set-up is closed with the upper flange, and tight together using a spring system composed of threaded rods, washers, springs and nuts. The springs are compressed by around 2 mm from their rest position, which is checked using a Vernier caliper. After that, the set-up is placed in the opened furnace, followed by connecting, using silicon tubes, the air and fuel inlets to the gas manifold system used to supply air, hydrogen and argon. In order to run the furnace, a blue security plug must be inserted to the female socket which is behind the kiln. Figure 3.3 shows the test assembly with gas manifold inside the walk-in fumehood.



Figure 3.3 The test assembly with gas manifold inside the fumehood.

For MS-SOFC, during heating up of the setup to the desired temperature (e.g. 750°C), a reducing gas must be supplied at the anode side to prevent oxidation of the metal support. The reducing gas used here is a 5% H₂, balanced argon gas mixture. This gas mixture, during preheating is further diluted with argon, the flow rate of each being typically 50 mL/min for the gas mixture and 100 mL/min for pure argon. Calibration of each flowmeters can be found in Appendix. Then, snoop leak detector is used systematically to check if there is any leakage before starting to heat up the furnace. The cell thermocouple probe is connected to a digital temperature reader, and the set-up shell is connected to the ground by using a clamp to isolate the set-up shell from both the anode and cathode. Then, the temperature controller is turn on. The temperature

profile which has been used for cell analysis is shown in Table 3.1 below.

Table 3.1 – Temperature profile to heat up the test setup to the desired temperature (here 750°C) and to cool down at the end of the experiment.

Temperature (°C)	Ramping rate (°C/hr) (duration)	Dwell (hr)
400 (from room temperature, 25°C)	120°C/hr (~3.20 hr)	0
750	200°C/hr (1.45 hr)	as desired
Cooling down to 450°C	300°C/hr (0.50)	0
Cooling down to room temperature (25°C)	Furnace turned off (natural convection cooling)	0

When the temperature has reached the desired temperature (here 750°C) the 5% H₂/Ar gas mixture is switched to pure H₂ and the experiment is ready for measuring the OCV, polarization curve and EIS curve using a biologic potentiostat (CML-SP-150-2), after proper connection of the electrical wire to the anode and cathode sides.

3.1.5.2 Electrochemical Impedance Spectroscopy

Electrochemical impedance spectroscopy is used to measure polarization and Ohmic resistances for the cells tested. Grain boundary and grain interior are two various paths through which current can pass into the electrolyte. Because these mechanisms are different, various resistances are shown by these mechanisms due to their various time constants. The resistances of these two mechanisms can be distinguished when AC voltage bias with different frequencies are utilized. Equation 3.1[6, 11] expresses the relation between actual voltage signal and angular frequency

$$E^l = E_o \sin(\omega t) \quad (3.1)$$

Where E^l is the actual voltage signal, E_o is the set voltage bias, t is the time, and ω is the angular frequency which is equal to $2\pi f$.

Equation 3.2 [6, 11] shows the actual current passing through the sample, when an AC voltage bias is applied.

$$I^l = I_o \sin(\omega t + \phi) \quad (3.2)$$

where I^l is the actual passing current through the sample, I_o is the output current signal, and ϕ is the

phase angle.

Equation 3.3 [6] shows the definition of the impedance of the system in the time domain, Z , expressed as the actual voltage signal divided by the actual current passing through the sample.

$$Z = \frac{E^1}{I^1} \quad (3.3)$$

Equation 3.4 shows the impedance, Z , when expressed as complex number in the frequency domain [11,155]

$$Z = |Z| \exp j\varphi = |Z| \cos(\varphi) + j|Z| \sin(\varphi) = Z^1 + Z^{11} \quad (3.4)$$

where Z^1 is the real part of the impedance and Z^{11} is the imaginary part.

In order to represent impedance, the Nyquist and Bode plots are used, as seen in Figure 3.4, where the real and imaginary parts of the impedance are represented in Nyquist plot (Figure 3.4a), and where the phase angle and impedance module are represented in the bode plot as a function of the frequency (Figure 3.4b).

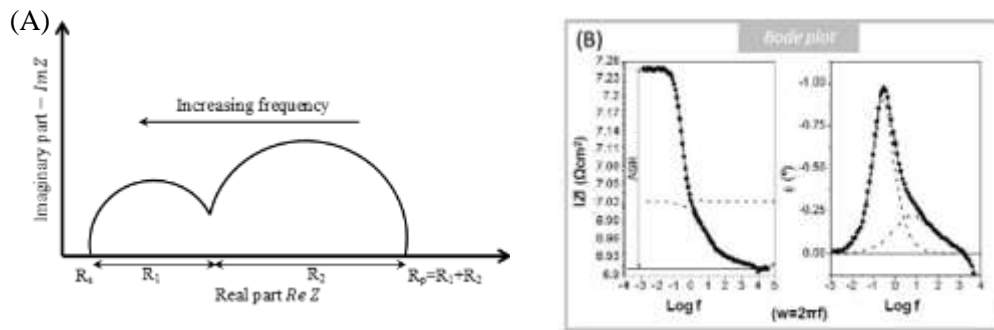


Figure 3.4: (A) Nyquist diagram and (B) Bode diagram of a SOFC [11,155,156]

Area Specific Resistance (ASR), ohmic resistance and polarization resistance can be identified from the Nyquist plot. In this work, the ASR is defined as the surface area of current collector. Equation 3.5 shows the ASR formula.

$$ASR (\Omega.cm^2) = (R_s + R_p) * A \quad (3.5)$$

where R_s is the polarization resistance (which can be obtained from EIS, as seen later in this chapter) and A is surface area of current collector, which in our case is 0.785 cm^2 (1 cm diameter

current collector).

The ohmic resistance, which is the potential loss incurred due to resistance to transport of charge in the system, can comprise the resistance to ions travelling through electrolyte and electrons travelling through current collectors and interconnect. Polarization resistance is associated with activation of electrochemical reactions taking place at the electrodes. The activation barrier to these reactions is in turn dependent on the reaction kinetics and the activity of the catalyst. [5,6].

The Nyquist plot shows different semicircles, and all these semicircles represent various conduction mechanisms in the cell such as electrolyte resistance, charge transfer and electrode polarization. The resistance values are represented at the x-intercepts. EC-LabV11.20 and Z sim software were utilized for the EIS analysis.

For example, the Nyquist plot shown in Figure 3.2A displays two semi-circles; which represent the total polarization resistance $R_p = R_1 + R_2$ at low frequency and high frequency spectra. Whereas, at the end of the high frequency spectra ohmic resistance is represented by R_s . In order to measure the ohmic and polarization resistances, an equivalent electrical circuit model, which involves inductor (L), resistor (R) and capacitor (C), is utilized. Figure 3.5 shows the equivalent circuit that was selected in this study to fit into impedance spectra for measuring resistances.

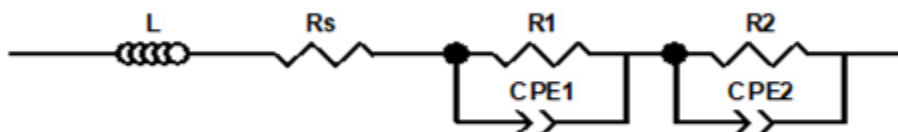


Figure 3.5 Equivalent circuit used in the present work

In this study, because we are using a 2-electrode system, the polarization resistance R_p ; which is measured over the full cell represents the combined impacts of both anode and cathode processes.

3.2 Experimental Procedure

In this part, chemical preparation and experimental procedure for making half-cells and then single cells are presented in detail. Different procedures and chemical compositions have been utilized to prepare metal transition layer, dense YSZ electrolyte, porous YSZ cathode scaffold, and

cathode transition layer, not only because the different layers have different compositions, but also because YSZ has lower density particles (6.1 g/cm^3) than metal support particles (7.7 g/cm^3). Regarding the last point, because of the higher density of metal support particles, the sedimentation problem when metal particles are present can easily occur, but this issue has been resolved as described in the subsequent sections.

3.2.1 Selection of Half MS-SOFC Materials

The MS-SOFC half-cell is composed essentially of the metal support layer, the anode layer and the electrolyte layer, with eventually some transition layers in between. For the electrolyte, YSZ has been chosen because it can sinter at high temperature in reducing atmosphere. In conventional SOFC, high temperature sintering is done in air, but here reducing atmosphere is necessary when using metal support to prevent metal oxidation.

In this thesis, SS-430L has been selected as metal support based on shrinkage behavior and compatibility with YSZ [6].

3.2.2 Configurations of the Half-cell Structures

Two cell structures have been considered in this work, as seen in Figure 3.6, the main difference between the two being the design of the cathode. Structure 1 consists of a stand-alone cathode deposited on the half-cell (Figure 3.6a), whereas structure 2 consists of a porous cathode scaffold co-sintered with the half-cell, followed by impregnation of the active cathode material.

The half-cell structure #1, is composed of four layers which are 1) the porous metal support layer, 2) metal transition layer which is used to provide a smooth transition from metal support to YSZ, 3) dense YSZ electrolyte layer, and 4) cathode transition layer.

In the half-cell structure #2, the first 3 layers are the same and the difference is the use of a YSZ cathode scaffold instead of a cathode transition layer which is used to increase the Triplee Phase Boundary (TPB).

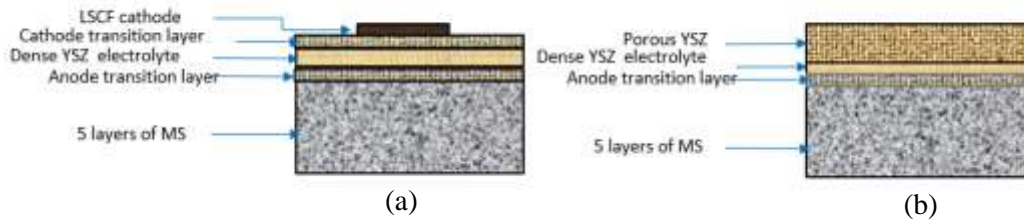


Figure 3.6: (a) Cell structure 1: Stand-alone cathode layer; (b) Cell structure 2: Porous infiltrated cathode scaffold

3.2.3 Slurry Preparation for Tape Casting of Half MS-SOFC

3.2.3.1 Slurry for Metal Support Layer:

Acetonitrile and Polyethylene Oxide (PEO) have been selected as solvent and binder, respectively, for preparing the metal support slurries. Due to the high density of SS-430L powder which can precipitate easily, one of the advantages found in acetonitrile and PEO when they are mixed together as solution is the control of SS-430L sedimentation. 5 g of PEO are added to 70 g of acetonitrile, and ball milled (20/100 rotating speed) for 24 hours to become a viscous solution. This viscous solution is referred as “MS-Preliminary slurry”. After that, 12 grams of MS-Preliminary Slurry is poured to a 100 ml-vial, next 7.2 grams of SS-430L is added to 12 grams of MS-Preliminary Slurry; those amounts were chosen because not only no particles agglomeration were observed in the slurry, but also no cracks were observed on the dried tape casted sheet [6]. Thereafter, the mixture is mixed by using a vortex mixer (VWR, Analog Vortex Mixture Canada) at maximum speed (10) because of the high mixture’s viscosity. In order to achieve sufficient porosity of the metal support (in the vicinity of 40%) for allowing enough fuel gas diffusion, Poly(methyl methacrylate), PMMA, has been used as an organic pore former in this study and added to the above mixture; a PMMA/SS-430L mass ratio of 0.125 was chosen based on [6], where a final MS support layer porosity around 40% is achieved under those conditions (this correspond to a PMMA mass of 0.9 g). In order to avoid the agglomeration of PMMA particles in the slurry, PMMA is added to the slurry while the slurry is mixed on the vortex mixer; it is important that the slurry remains vibrating on the vortex mixer while adding PMMA. Finally, because of the small loss of PMMA during the procedure, an initial mass of 1 g of PMMA is used (instead of 0.9g). Table 3.2 summarize the amounts used and

corresponding mass percentage of the metal support (SS-430L) slurry used in this study.

Table 3.2: Composition of slurry for metal support

Component	Mass (g)	wt%
MS-preliminary slurry	12	59.70
SS-430L	7.2	35.82
PMMA	.9	4.48

3.2.3.2 Slurry for Ceramic Layers:

In this study, ethanol and toluene, Poly Vinyl Butyral (PVB), Santicizer S-160, Hypermer KD-1 have been utilized as solvents, binder, plasticizer and dispersant, respectively, to prepare the transition layer slurry, the dense YSZ electrolyte slurry, and the porous YSZ slurry. The chemical compositions of those slurries were chosen based on optimal slurry compositions studied in [6]. It was necessary to prepare two types of slurry, one is a preliminary slurry common to all layers and the second is a base slurry whose composition depends on the layer. The reason is the binder (PVB) and plasticizer (Santicizer S-160) can form particle agglomeration if mixed directly with the base slurry.

All the above-mentioned slurries are based on the same preliminary slurry, referred here as “ceramic preliminary slurry”. The ceramic preliminary slurry is produced by mixing 38.4 g of ethanol, 60.36 g of toluene, 81.96 g of santicizer, and 43.8 g of PVB, and then ball milled for 24 hours. The preliminary ceramic slurry composition is shown in table 3.3.

Table 3.3: Composition of the ceramic preliminary slurry

Component	Mass (g)	wt %
PVB(Polyvinyl butyral)	43.80	19.508
Sanitizer 160	81.96	36.504
Ethanol	38.40	17.103
Toluene	60.36	26.884

Specific base slurries for each ceramic layer were prepared. Those base slurries contain ethanol, toluene, Hypermer KD-1, and base powders (YSZ, SS-430L, PMMA, LSCF). The differences between the different ceramic layer slurry compositions resides on the different base powder composition. For all base slurries, 1.15 g of ethanol, 1.68 g of toluene are mixed with 0.168 g of Hypermer KD-1 using the vortex mixture until achieving a homogeneous solution. Then, the base

powders of the desired materials (with the exception of PMMA) are added to this solution using the vortex mixer (at maximum speed). The resulting base slurry is ball milled for 24 hours. In this thesis, 8 g of YSZ powder was used as base powder for the dense YSZ electrolyte slurry. In term of metal transition slurry, 3.75 g of stainless steel (SS-430L) and 3.75 g of YSZ were used as base powder. For porous YSZ slurry, 7.5 grams of YSZ was used as base powder. For the cathode transition slurry, 7.125 g of YSZ and 0.05 g of LSCF have been used as base powder.

Thereafter, 3 grams of ceramic preliminary slurry is added to the base slurry, and ball milled together for 24 hours. PMMA is not added during the 24-hour ball milling step as it would agglomerate; instead, it is added to the slurry just before tape casting. The amount of PMMA added is such that the mass ratio of PMMA/(YSZ+SS-430L) is 0.2 for the anode transition slurry, and the mass ratio of PMMA/YSZ is 0.35 for the porous YSZ slurry. The base powder slurry compositions for the different layers are shown in table 3.4.

Table 3.4: Base powder slurry for transition, porous layers and electrolyte layers.

Component	Anode transition layer mass(g)	Mass wt%	Cathode Layer mass (g)	Mass wt%	Porous YSZ layer mass (g)	Mass wt%	Dense YSZ layer mass (g)	Mass wt%
Ethanol	1.15	9.59	1.15	11.3	1.15	8.77	1.15	10.46
Toluene	1.68	14	1.68	16.5	1.68	12.8	1.68	15.3
Hypermer as dispersant	.168	1.4	.168	1.66	.168	1.28	.168	1.53
PMMA	1.5	12.5	-		2.62	19.98	-	
SS-430L	3.75	31.3	-		-		-	
YSZ	3.75	31.3	7.125	70.1	7.5	57.21	8	72.79
LSCF	-		.05	.49	-		-	

3.2.4 Tape Casting and Co-Sintering Procedure for the MS-SOFC Half-Cell

3.2.4.1 Tape Casting:

To degas any air bubbles that may be in the slurries, all slurries vials are left open for a minute at room temperature in air atmosphere before tape casting.

The procedure for tape casting is as follows:

- Open the cover of the MTI tape caster and turn on the vacuum pump.
- Place the silicon coated mylar sheet (tape casting substrate) on the vacuum bed.
- Insert the slot die head (without forgetting to attach the springs) and adjust the gap to the desired value of tape thickness using the micrometer heads. The thickness of the tape has been selected depending on the type of slurry. The tape casting thickness of all slurries are listed in Table 3.5.

Table 3.5: The tape casting thickness of cell slurry

Slurry	Casting thickness (μm)
Metal support	750 ^a
50/50 MS/YSZ anode transition layer	350 ^a
Dense YSZ for electrolyte	175 ^a
LSFC/YSZ cathode transition	150 ^b
Porous YSZ	400 ^b

^a From [6]

^b Determined from trial and error in the present work

- Proceed with tape casting (“run” button) after setting up the speed to 016.
- After the tape casting process, the casted slurries are left at room temperature for 20 minutes until the casted slurry becomes dried.
- Remove the casted tape from the vacuum bed and, using a 20 mm diameter punch set with hammer, punched out disks. Repeat for each layer: metal support layer, transition layer, porous layer, and electrolyte layer.

3.2.4.2 Co-Sintering:

Before co-sintering the MS-SOFC half-cell, the layers are pressed together using a molding die set (20 mm diameter cylindrical shape) and a hydraulic press at 11 metric ton for 5 minutes. Both cell structures followed the same procedure. The “stand-alone cathode layer” structure consists of 5 disks of metal support, 1 disk of 50/50 SS-430L/YSZ anode metal transition, 1 disk of dense YSZ electrolyte, and 1 disk of 95/5 YSZ/LSCF cathode transition layer. The “porous infiltrated cathode scaffold” structure consists of 5 disks of metal support, 1 disk 50/50 SS-430L/YSZ anode transition, 1 disk of dense YSZ electrolyte, and 1 disk of porous YSZ cathode scaffold.

The cells of both structures are co-sintered at 1325°C for 2 hours in reducing atmosphere (5% H₂/95% Ar) in a MTI GSL-1500X tube furnace. The co-sintering profile for these structures are based on the shrinkage study for SS430L and YSZ electrolyte [6], and is listed in table 3.6. To ensure that no oxygen is present, as even small amount would be detrimental to the oxidation of the metal support affecting expansion/shrinkage behaviour (e.g. due to chromia formation), scavenger particles (SS-430L powder) have been placed inside the tube on each side of the disks (see Figure 3.7).

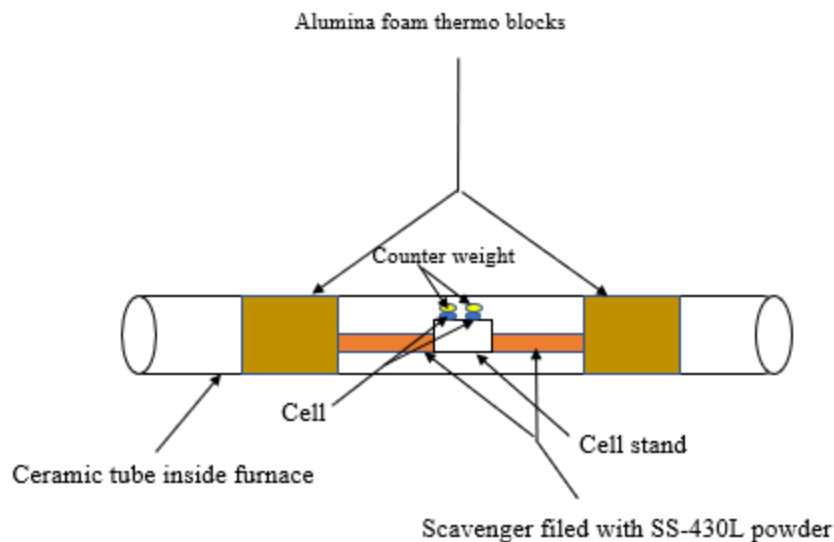


Figure 3.7: Scavenger, counter weight and thermo block

In addition, in order to reduce warping during cell sintering, a counterweight has been placed on the cell during co-sintering. For thermal isolation during high sintering temperature, alumina foam blocks have been used as insulating materials. The flow rate of the 5% H₂/95% Ar gas is set at 114 mL/min (i.e. scale reading of 30 using the rotameter with stainless steel float). This flow rate was determined as sufficiently high to prevent any air ingress, but sufficiently low to allow the furnace to attain the sintering temperature. Before starting the furnace, wait for one hour with the 5% H₂/95% Ar gas to ensure that the tube is purged.

Table 3.6: Co-sintering temperature profile for half MS-SOFC

Temperature (°C)	Ramping rate (°C/min)	Dwell (min)
400 (from room temperature, 25°C)	2 °C/min (188 min)	30
1000	5°C/min (120 min)	10
1325 sintering temperature	7.5°C/min (43 min)	120
Cooling down to room temp (25°C)	3.25°C/min (400 min)	0

3.2.5 Anode and Cathode Infiltration Procedures

In this research, infiltration method was used to infiltrate anode and cathode catalysts into porous metal and porous YSZ cathode scaffold, respectively. NiO/SDC and LSCF/GDC have been used as anode and cathode catalyst respectively [6].

3.2.5.1 Anode Infiltration:

To prepare the anode infiltration solution, 29.631 grams of nickel nitrate, 3.867 grams of samarium nitrate, 15 grams of cerium nitrate and 250 ml of DI water are mixed in a 500 mL beaker and then covered using laboratory film (parafilm “M”). For samarium and cerium nitrates, use aluminum weighing dish (to ensure all the particles in the weighing dish are poured in the beaker, use part of the DI water to “rinse” the weighing dish). For nickel nitrate use a 500ml beaker (because of the larger amount) and use the “Scout Pro” balance. The beaker is then placed on a heated plate (50°C) with magnetic stirrer (speed 300 rpm) for 90 minutes. Then, 1 gram of Triton x-100 is added,

and the final mixture is left stirring at 50°C for 24 hours. Triton x-100 is added to the anode solution in order to reduce the surface tension of the solution to facilitate infiltration. Table 3.7 summarizes the anode composition used in this study (same for both structures investigated here).

Table 3.7: Anode composition used for anode infiltration

Component	Mass (g) , volume (ml)	Mass wt % for all of powder added to solution	Mass (g) for Ce, Sm and Ni	Mass wt% for Ce, Sm and Ni
Cerium nitrate hexahydrate	15 (g)	30.30	4.84	39.9
Samarium nitrate hydrate	3.869 (g)	7.82	1.31	10.80
Nickel nitrate hexahydrate	29.631 (g)	59.86	5.98	49.30
DI water	250 (ml)	-	-	-
triton x-100	1 (g)	2.02	-	-

Before impregnation, the anode solution is heated up to 90°C while stirred (300 rpm) for 30 minutes. Before anode infiltration, the mass of the cell is measured. A small pipette is used to impregnate the anode catalyst in the porous metal support and especially in the anode transition layer. Figure 3.8 shows the pipette used for anode and cathode catalysts infiltration into porous structure.

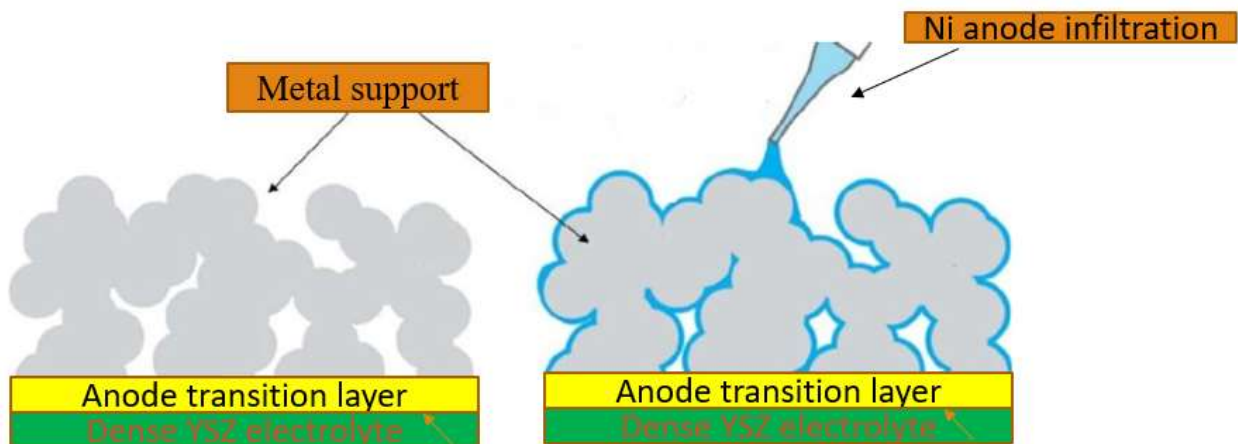


Figure 3.8: A schematic of the Ni- SDC anode fabricated through infiltration

The infiltrated cell is then heat-treated at 400°C in air in a muffle furnace to break down the nitrates to form Ni oxide. The temperature ramp is 1.5°C per minute and the dwell time at 400°C is 5 minutes, after which the furnace turns off. After cooling, the mass of the infiltrated cell is weighed. This infiltration/heat treatment process is repeated through up to 5 cycles, until reaching a 10 wt% loading based on the initial cell mass.

3.2.5.2 Cathode Infiltration:

Cathode infiltration is only for the porous infiltrated cathode scaffold structure. For cathode catalyst infiltration, Samarium Barium Strontium Cobalt oxide (SBSCo) solution was used. This solution is composed of 4.821 grams of samarium nitrate, 2.835 grams of barium nitrate, 2.296 grams of strontium nitrate, 12.62 grams of cobalt nitrate, and 250 ml of DI water. In addition, 10 grams of anhydrous citric acid is added to this cathode solution as chelating agent for metal nitrate solution, and 7 grams of ammonium hydroxide are added to this solution to induce the chelating agent. In other words, citric acid and ammonium hydroxide are added to prevent particle sedimentation. Ammonium hydroxide addition should be done in the fumehood. In order to reduce the cathode solution surface tension, 25 ml of ethanol is used as surfactant material. The same infiltration procedure as that described for the anode was used, except that obviously the cathode solution was infiltrated on the cathode transition layer. Table 3.8 shows cathode composition used in this study

Table 3.8: Cathode solution composition and SBSCo composition.

Component	Mass (g) , volume (ml)	Mass wt % for all of powder added to solution	Mass (g) for Sm, Ba, Sr, and Co	Mass wt% for Sm, Ba, Sr, and Co
Samarium Nitrate hexahydrate	4.821 (g)	12.18	1.63	24.59
Barium Nitrate	2.835 (g)	7.16	1.49	22.47
Strontium Nitrate anhydrous	2.296 (g)	5.8	.95	14.32
Cobalt nitrate hexahydrate	12.62 (g)	31.89	2.56	38.61
DI water	250 (ml)	-	-	-
Citric acid	10 (g)	25.27	-	-
Ammonium hydroxide	7 (g)	17.69	-	-
Ethanol	25 (ml)	-	-	-

3.2.6 Cathode Deposition and Ex-Situ Sintering for Deposited Cathode

Contrary to the case of cell structure 2 in which the cathode catalyst material is infiltrated into a porous YSZ scaffold, for cell structure 1, a LSCF/GDC cathode layer is printed onto the electrolyte surface. The procedure is as follows. First, five pieces of scotch tape are piled together. After that, the piled tapes are punched using a 6 mm diameter punch set. This diameter represents the diameter of the cathode layer to be deposited. Thereafter, the punched tape is placed in the center of the electrolyte surface to deposit LSCF/GDC cathode ink on the hole of the tape. Then, a blade (similar to doctor blade) is used to level off the deposited ink. Next the punched tape is removed. After that, the circular printed cathode is left in the air for two hours to dry, after which it is ex-situ sintered in argon atmosphere, according to the temperature profile shown in Tables 3.9 and 3.10.

Table 3.9: Old ex-situ sintering temperature profile used for printing the LSCF/GDC cathode on the YSZ dense electrolyte

Temperature (°C)	Ramping rate (°C/min)	Dwell (min)
400 (from room temperature, 25°C)	2 °C/min (188 min)	30
1100	1.8°C/min(388min)	120
Cooling down to room temp (25°C)	2.56°C/min (420 min)	0

Table 3.10 New ex-situ sintering temperature profile used for printing the LSCF/GDC cathode on the YSZ dense electrolyte

Temperature (°C)	Ramping rate (°C/min)	Dwell (min)
100 (from room temperature, 25°C°C)	2 °C/min (38 min)	60 min
800	2 °C/min (350 min)	60 min
1125	1.8 °C/min (181 min)	60 min
Cooling down to room temp (25°C)	2.62 °C/min (420 min)	0

Chapter 4 Results and Discussion

As described previously, the overarching goal in our group at UW is to develop a MS-SOFC using conventional ceramic processing techniques such as tape-casting and screen printing. More specific to the present study is the development of a cathode for an MS-SOFC that can be prepared (essentially sintered) ex-situ, which would be considerably more practical than in-situ sintering. In this work we considered two main routes to fabricate the cathode: 1) stand-alone cathode layer and 2) porous infiltrated cathode scaffold, as seen in Figure 4.1. For both structures, the half-cell, composed of metal support layer, anode transition layer and dense electrolyte layer are the same. The difference between the two structures is that for the stand-alone cathode layer structure, the cathode layer is printed on the assembly after co-sintering the half-cell (to which is also added eventually a cathode transition layer), whereas for the cathode scaffold structure, the cathode material is infiltrated in the co-sintered half-cell/porous cathode scaffold assembly.



Figure 4.1: (a) Cell structure 1: Stand-alone cathode layer. (b) Cell structure 2: Porous infiltrated cathode scaffold

Finally, depending on the cathode structure, we have used two different cathode materials. For the stand-alone cathode layer, a cathode paste was needed and since not only LSCF was indicated as a possible cathode material for ex-situ MS-SOFC, but also because LSCF paste is commercially available, LSCF was selected as the cathode for the stand-alone cathode layer. For the cathode scaffold structure, it was decided to use Samarium Barium Strontium Cobalt oxide (SBSCo) because it can be calcined at relatively low temperature.

4.1 Fabrication and Performance of MS-SOFC with Stand-alone Cathode Layer.

4.1.1 Fabrication of Full MS-SOFC Cell with Stand-alone Cathode Layer

The fabrication of MS-SOFC for cells with stand-alone cathode layer has been made using three consecutive steps. The first step is to co-sinter in reducing atmosphere (95% Ar, 5% H₂) the metal support with the anode transition layer, the electrolyte layer and eventually a cathode transition layer. The second step is to infiltrate and calcine the anode catalyst, and then the third step is to print the cathode layer and sinter it in argon atmosphere.

The first and main challenge is the fabrication of a cell that is visually not warped and not cracked. Such MS-SOFC cells are very sensitive to any changes in the fabrication process. The half-cell fabrication recipe is the result of the work of a previous graduate student. Nonetheless several tries were necessary to just come up with a flat and not cracked full cell.

The first full cell that was fabricated had the following structure: 5 MS layers, 1 anode transition layer and 1 dense YSZ electrolyte layer. Composition of the different layers are given Chapter 3. This half-cell was sintered under reducing atmosphere (5% H₂, 95% Ar), and the temperature profile used was that shown in Table 3.5 in chapter 3. However, this fabrication method led to huge cracks, as seen in Cell 1 in Table 4.1.






Then in order to avoid cracks on the electrolyte, a cathode transition layer (whose composition is shown in Table 3.3) was added on top of the electrolyte. The resulting cell was visually flat and without cracks, as seen in Cell 2 in Table 4.1.


In order to improve the YSZ electrolyte densification, the amount of YSZ powder was increased from 7.5 g to 8 g in the electrolyte slurry and sintered using a 7°C/min ramping rate to reach 1325 °C. However, although the resulting cell was flat, some cracks on the cathode transition surface appeared, as seen in Cell 3 in Table 4.1.

The amount of YSZ powder was further increased to 8.5 g in the electrolyte slurry, but the resulting cell, sintered at 1325°C at rate of 7°C/min, still showed some cracks, even though it was flat, as seen in Cell 4 in Table 4.1. Several attempts with 8.5g of YSZ powder in the electrolyte slurry were attempted at different sintering temperature ramping rate, but all showed some cracks.

Finally, after several trials and errors, it was found that 8.0 g of YSZ powder in the electrolyte slurry sintered at a ramping rate of 7.5 °C/min up to 1325°C, and with cathode transition layer led to the most visually satisfactory cell, in term of flatness and absence of cracks, as seen in Cell 5 in Table 4.1. Note that a change in sintering ramping rate to 7.6 °C/min is sufficient to lead to some cracks.

Table 4.1 – Resulting half-cell depending on different fabrication process parameters.

Sintered cell	Description	Picture
Cell 1	Cell without cathode transition layer.	
Cell 2	Cell with cathode transition layer	
Cell 3	Cell with 8 g of YSZ in the electrolyte layer and with a sintering ramping rate of 7 °C/min up to 1325 °C. Also with a cathode transition layer.	
Cell 4	Cell with 8.5 g of YSZ in the electrolyte layer and with a sintering ramping rate of 7 °C/min up to 1325 °C. Also, with a cathode transition layer.	
Cell 5	Cell with 8 g of YSZ in the electrolyte layer and with a sintering ramping rate of 7.5 °C/min up to 1325 °C. Also, with a cathode transition layer.	

Cell 6	Cell with mixed coarse (tape cast grade) YSZ powder and nano YSZ powder; sintering ramping rate of 7.5 °C/min up to 1325 °C. Also, with a cathode transition layer.	
--------	---	--

Still with the goal of densifying the electrolyte as much as possible, it was attempted to mix the tape-cast grade YSZ powder with some nano YSZ powder using different ratios, but all led to broken cells, as shown in Cell 6 in Table 4.1.

In conclusion, for the stand-alone cathode layer structure, it seems that, prior to cathode printing, a cathode transition layer is necessary here, and one should use 8.0 g of tape cast grade YSZ powder in the electrolyte slurry and sinter the half-cell at a temperature ramping rate of 7.5 °C/min. The cathode was then printed on the half-cell/cathode transition layer assembly using the procedure described in Chapter 3. The resulting SEM micrograph of that cell, before any test is shown in Figure 4.2, where each layer is indicated. From this figure, the cathode transition layer is hardly distinguishable from the electrolyte. The electrolyte appears dense, however one can see some areas (e.g. center of the picture) where the anode transition is not in complete contact with the electrolyte.

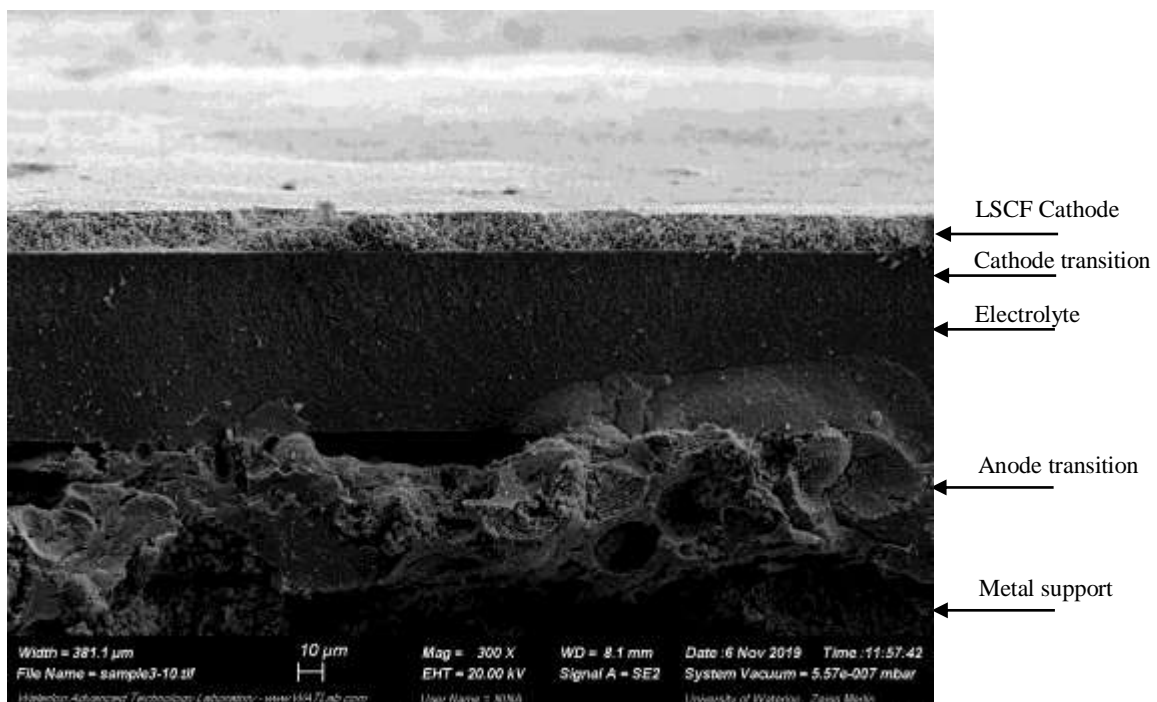


Figure 4.2 – SEM micrograph of fresh structure 1 cell, with cathode transition.

4.1.2 Electrochemical Performance of Full MS-SOFC Cell with Stand-alone Cathode Layer

Figure 4.3 shows the polarization curve and power density of a cell prepared as described at the end of section 4.1.1. The operating conditions for this test are 50% H₂ (balance argon) and cell temperature or 804°C. Clearly, the performance is very poor with a limiting current close to only 12 mA/cm² and a maximum power density of about 2.2 mW/cm². In addition, the open circuit voltage (OCV) was only ~0.85 V, when one would expect to be above 1 V. This low OCV is indicative of possible H₂ leaks through the electrolyte, which is further reinforced by the very high cell temperature, ~800°C, which is 50°C higher than the furnace temperature set of 750°C. The fact that voltage is falling very rapidly when the current is drawn points to very high polarization losses, which could be attributed to bad surface contact inside the cell between some layers and/or poor ionic/electronic conductivity. Figure 4.4a shows the corresponding micrograph of the cell used in Figure 4.3. In this figure, one can distinguish the cathode transition layer from the cathode layer. The electrolyte appears dense without cracks, but eventually some small holes. Figure 4.4b shows the EDX results for cathode layer, and part of the transition layer; since the cathode is composed of LSCF and SDC, and the cathode transition contains primarily YSZ, all elements shown in EDX are expected, with the exception of iron. It is not clear at this stage whether some iron has migrated to the cathode during operation, or if the presence of iron originates from cutting of the cell.

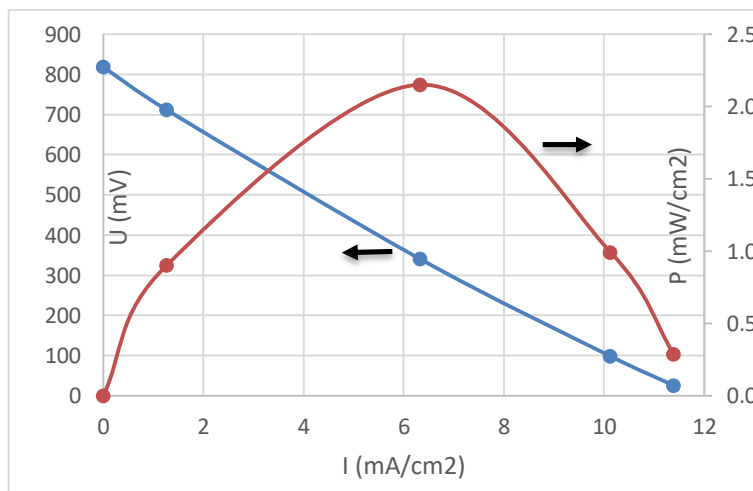


Figure 4.3 – Polarization and power density for a cell with cathode stand-alone layer. 50%

H₂ (balance argon), cell temperature ~800°C (furnace temperature of 750°C). With cathode transition layer.

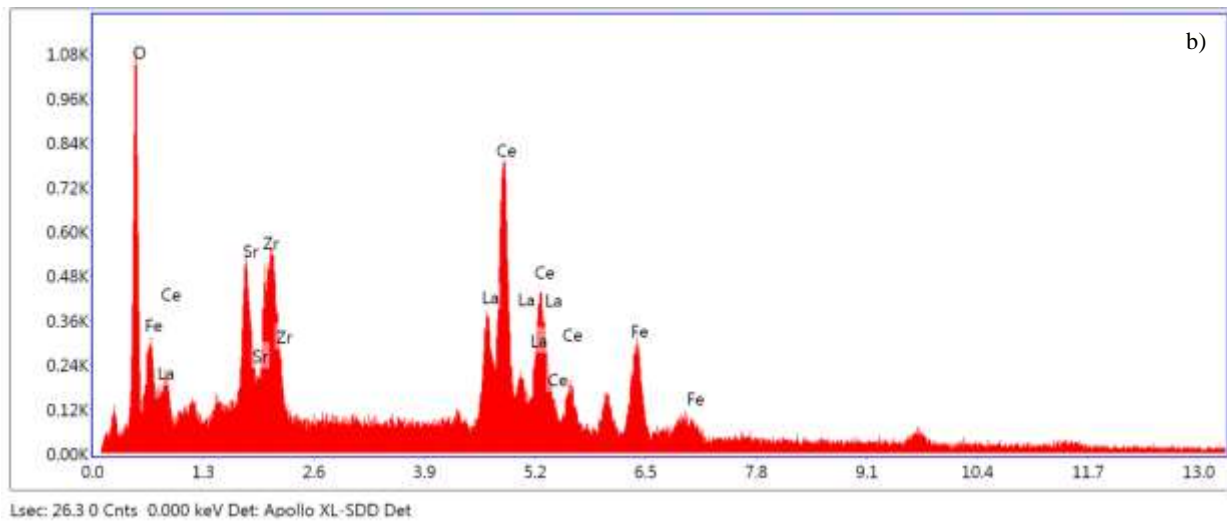
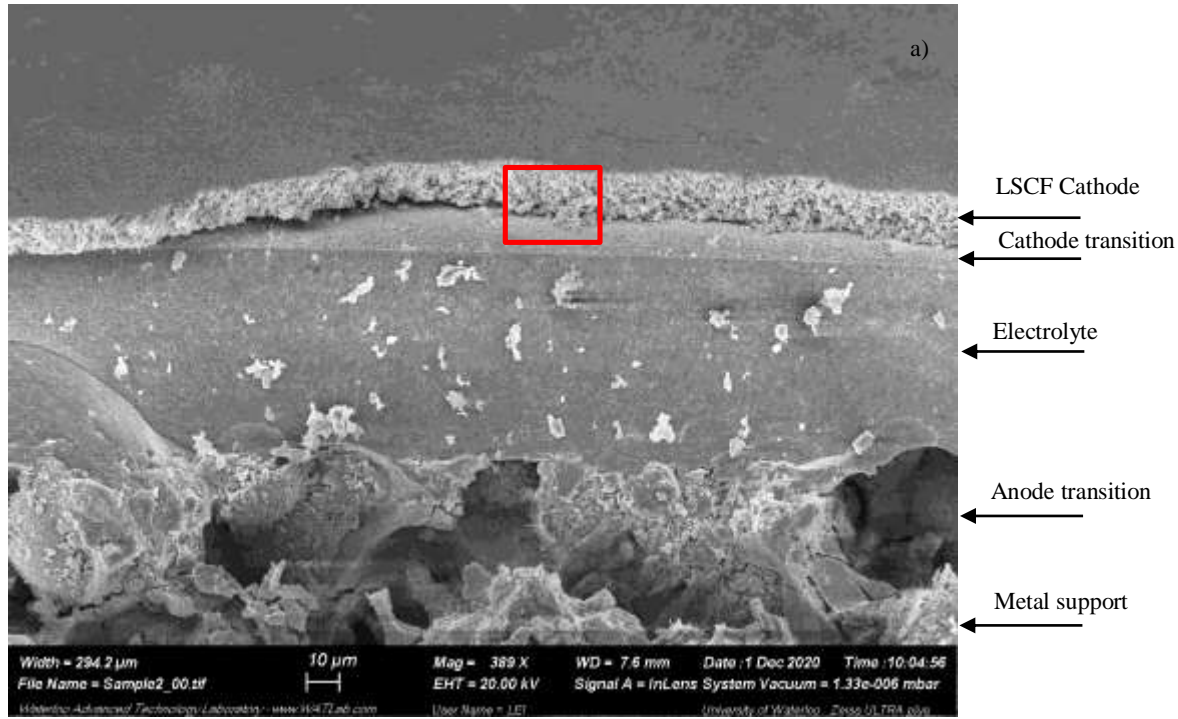


Figure 4.4 – Spent cell with cathode stand-alone layer. 50% H₂ (balance argon), cell temperature ~800°C (furnace temperature of 750°C). With cathode transition layer. a) SEM micrograph; b) EDX results for the region indicated by the red square in a).

One possible contribution to the large polarization could be the cathode transition layer, which was initially added to obtain flat and crackles cells. An attempt was successfully made to fabricate a half-cell without cathode transition layer that is flat and without apparent cracks, on which the LSCF cathode was printed. The electrochemical performance of this cell is shown in Figure 4.5. This cell shows similar poor results as those in Figure 4.2. However, even if the OCV is even lower (~ 620 mV), the limiting current density is slightly higher (above 12 mA/cm²) and the maximum power density is about the same (~ 2.2 mW/cm²). This indicates that, although there are still some leak-through problems (cell temperature of 784°C is still high), the polarization is lower in the case than in the previous case, most likely due to the removal of the cathode transition layer. EIS measurements were taken and shown in Figure 4.6, which indicates very high polarizations

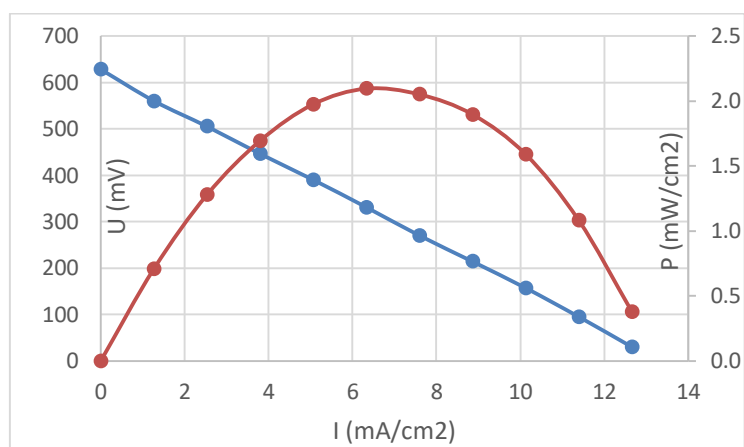


Figure 4.5 – Polarization and power density for a cell with cathode stand-alone layer. 40% H₂ (balance argon), cell temperature $\sim 784^\circ\text{C}$ (furnace temperature of 750°C). Without cathode transition layer.

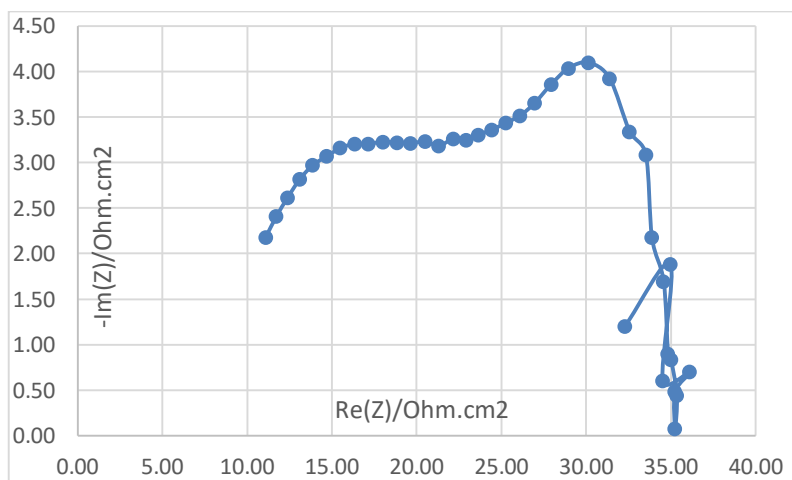


Figure 4.6 – Nyquist plot a cell with cathode stand-alone layer. 50% H₂ (balance argon), cell temperature ~784°C (furnace temperature of 750°C). Without cathode transition layer.

In order to improve the polarization resistance, if associated in part with poor contact between the cathode and the electrolyte (in the absence of cathode transition layer), the sintering profile for the printed cathode was modified. The resulting electrochemical performance is in Figure 4.7. The OCV is still poor (~650 mV), still indicating leak through the cell. However, the maximum power density (~5 mW/cm²) and limiting current density (~28 mA/cm²) have almost doubled compared to the original cell, indicating that the new cathode sintering profile is better, which is also seen in the EIS results shown in Figure 4.8 (when compared to Fig. 4.6). Nonetheless, the overall performance remains very poor. Figure 4.9 shows the corresponding SEM micrograph of the spent cell. Note that the cathode layer was found completely detached from the cell at the end of the experiment, which is why it does not show on the SEM micrograph. Figure 4.9 shows some cracks in the electrolyte, as well as areas where the electrolyte does not contact well with the anode.

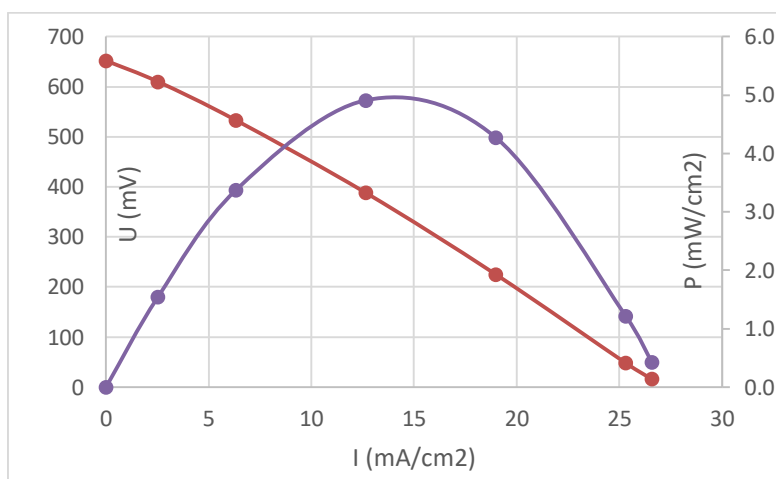


Figure 4.7 – Polarization and power density plot for a cell with cathode stand-alone layer. 33% H₂ (balance argon), cell temperature ~773°C (furnace temperature of 750°C). Without cathode transition layer. New cathode sintering profile.

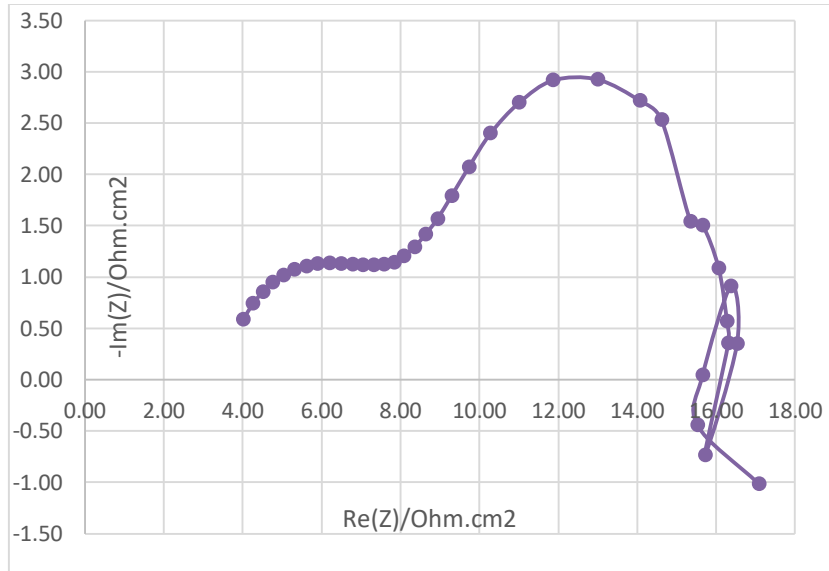


Figure 4.8 – Nyquist plot a cell with cathode stand-alone layer. 33% H₂ (balance argon), cell temperature ~773°C (furnace temperature of 750°C). Without cathode transition layer. New cathode sintering profile.

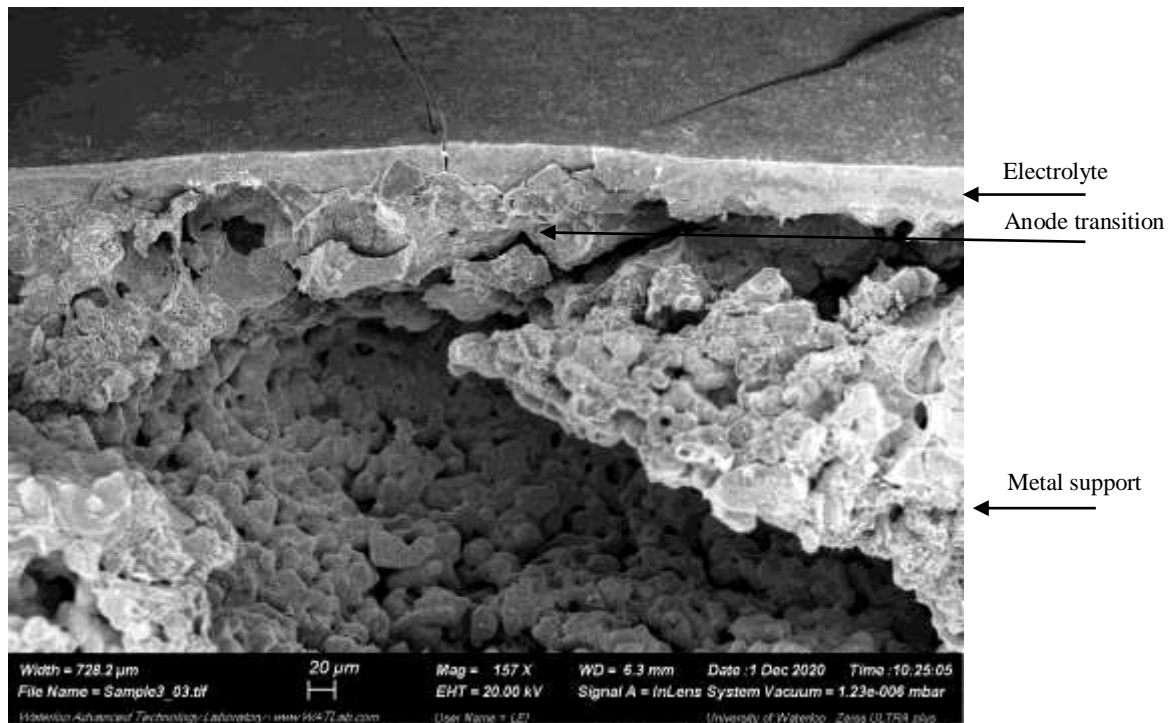


Figure 4.9 – SEM micrograph for cell with cathode stand-alone layer. 33% H₂ (balance argon), cell temperature ~773°C (furnace temperature of 750°C). Without cathode transition layer. New cathode sintering profile.

Finally, a cell with cathode transition layer was tested using the new cathode sintering profile and the results are shown in Figure 4.10. The OCV has been greatly improved, reaching 1010 mV. However, compared to the case without cathode transition layer, the limiting current is smaller ($\sim 14 \text{ mA/cm}^2$) and so is the maximum power density ($\sim 3.7 \text{ mW/cm}^2$). The EIS results are shown in Figure 4.11, which also indicate higher polarization when the cathode transition layer is present.

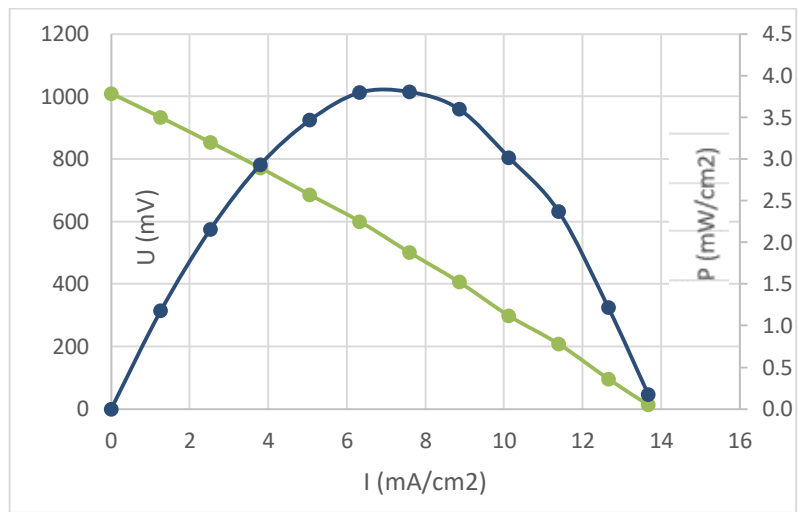


Figure 4.10 – Polarization and power density plot for a cell with cathode stand-alone layer. 38% H₂ (balance argon), cell temperature $\sim 773^\circ\text{C}$ (furnace temperature of 750°C). With cathode transition layer and new cathode sintering profile.

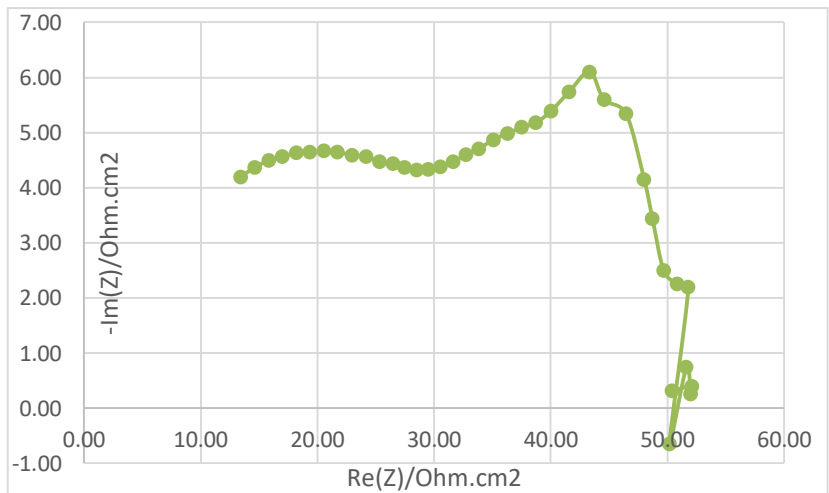


Figure 4.11 – Nyquist plot a cell with cathode stand-alone layer. 38% H₂ (balance argon), cell temperature

~773°C (furnace temperature of 750°C). With cathode transition layer and new cathode sintering profile.

Several attempts with modified stand-alone cathode layer structures were made, all without cathode transition layer, but all have failed. One attempt was to have a more graded structure by inserting a layer with 75% YSZ/ 25% SS between the MS layer and the anode transition layer, but the resulting cell after co-sintering showed major cracks (Figure 4.12a). Another attempt was to co-sinter the half-cell at 1325°C for 5 hours (also with 75wt% YSZ in electrolyte slurry, as opposed to 72.7wt% for the previous ones); the resulting cell is shown in Figure 4.12b, and was severely warped, although not cracked. A similar cell was then sintered for 4 hours, but that one had significant crack (see Figure 4.12c).



Figure 4.12 – Additional stand-alone cathode layer cell structures; a) more graded MS layer to anode transition layer, b) Cell co-sintered for 5 hours, c) Cell co-sintered for 4 hours.

In conclusion, there is still much work to do to improve the performance of the stand-alone cathode layer structure. Clearly, the cathode transition layer causes significant polarization losses, but at the same time helps in increasing the OCV. On the other hand, in the absence of the cathode transition layer, the polarization losses are lowered, but also is the OCV. The challenge is thus to manufacture a cell with good OCV (fully dense electrolyte) without the presence of a cathode transition layer.

4.2 Fabrication and Performance of MS-SOFC with Cathode Scaffold Layer.

4.2.1 Fabrication of Full MS-SOFC Cell with Cathode Scaffold Layer





The half-cell composed of the metal support, anode transition layer and electrolyte is the same as what is described in Chapter 3. The challenge here is to find the composition of the porous cathode scaffold (e.g. how much YSZ, how much PMMA in the slurry), which has to be co-sintered with the half-cell under reducing atmosphere. As a start, 8 g of YSZ powder with 20 % PMMA was tried, followed by co-sintering at 7.5°C/min up to 1325°C. Unfortunately, the resulting cell had major cracks, as seen in Cell 1 in Table 4.2.

Another trial was done using an amount of YSZ powder decreased to 7.5 g with 35 % PMMA, followed by co-sintering at 7.5°C/min. This cell worked well, leading to a flat cell and without cracks, as seen Cell 2 in Table 4.2.

In order to improve both the ionic and electronic conductivity of the cathode scaffold, porous SDC was tried instead of porous YSZ, using 7.5 g SDC with 35 % PMMA, followed by co-sintering at 7.5°C/min. However, those cells did not sinter well at all, as seen in Cell 3 in Table 4.3. This is not surprising considering that the co-sintering is carried out in reducing atmosphere thus affecting the oxidation state of ceria in SDC.

Although not directly related to the cathode scaffold, in order to increase the sintering of the electrolyte, it was also attempted to mix tape cast grade YSZ powder with YSZ nano powder, but still with a cathode scaffold. As in the case of the stand-alone cathode layer, it did not work leading to cracks on the cell (see Cell 4 in Table 4.4), likely due change of the electrolyte shrinking behavior in the presence of YSZ nano powder.

Table 4.2 – Resulting half-cell with cathode scaffold depending on different fabrication process parameters.

Sintered cell	Description	Picture
Cell 1	Cathode scaffold made of 8 g YSZ powder and 20% PMMA. Co-sintering at 7.5°C/min.	
Cell 2	Cathode scaffold made of 7.5 g YSZ powder and 35% PMMA. Co-sintering at 7.5°C/min and dwell for 2 hours	
Cell 3	Cathode scaffold made of 7.5 g SDC powder and 35% PMMA. Co-sintering at 7.5°C/min.	
Cell 4	Cell with mixed coarse (tape cast grade) YSZ powder and nano YSZ powder for the electrolyte. ; Cathode scaffold made of 7.5 g YSZ powder and 35% PMMA. Co-sintering at 7.5°C/min.	

In conclusion, the initial cell for testing was manufactured using the configuration of Cell 2 in Table 4.2. Figure 4.13 shows an SEM micrograph of a fresh cell with cathode scaffold (structure 2). Figure 4.14 shows the EDX results for the main region layers of the cell. The composition of the electrolyte (Figure 4.14a) is exactly what is expected (yttria and zirconia). For the cathode scaffold region (Figure 4.14b), with the exception of strontium (which may be hidden in the large peak of yttrium), barium, samarium and cobalt are clearly present, which indicates that the infiltration of the cathode solution has successfully reached the cathode/electrolyte interface. For the anode transition region (Figure 4.14c), only the expected components

are detected (Ni infiltrated, Fe from the metal support, and Y/Zr from YSZ).

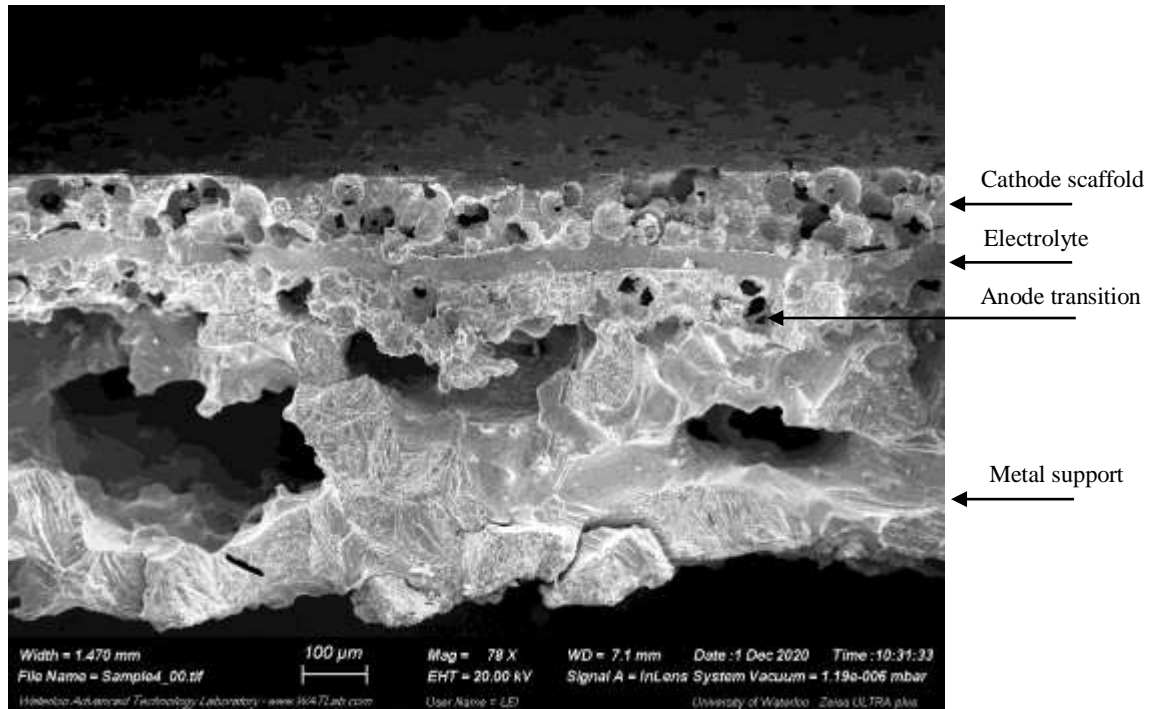
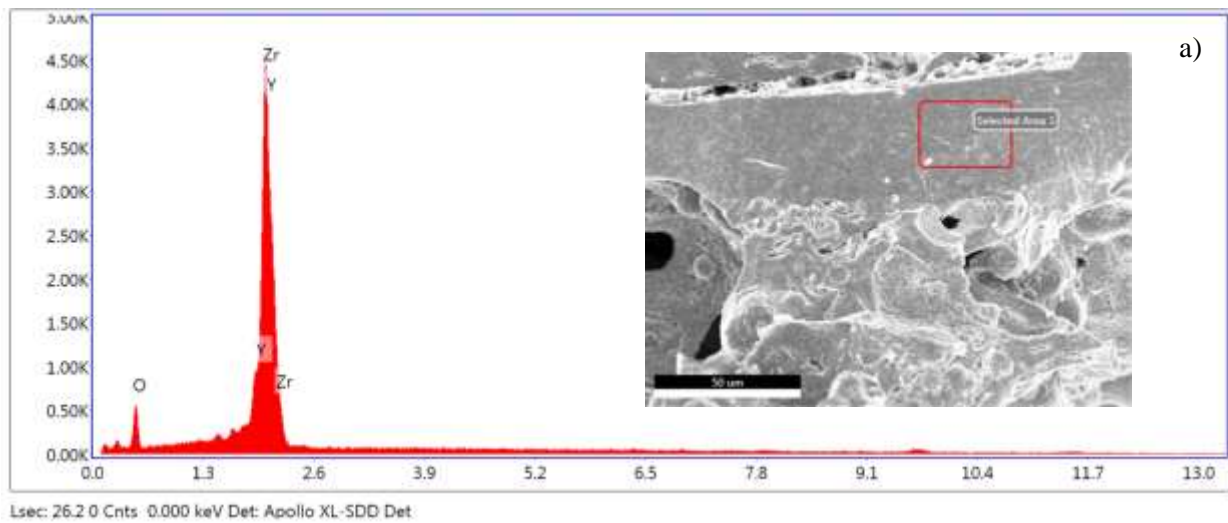


Figure 4.13 – SEM micrograph of fresh cell with cathode scaffold (structure 2)



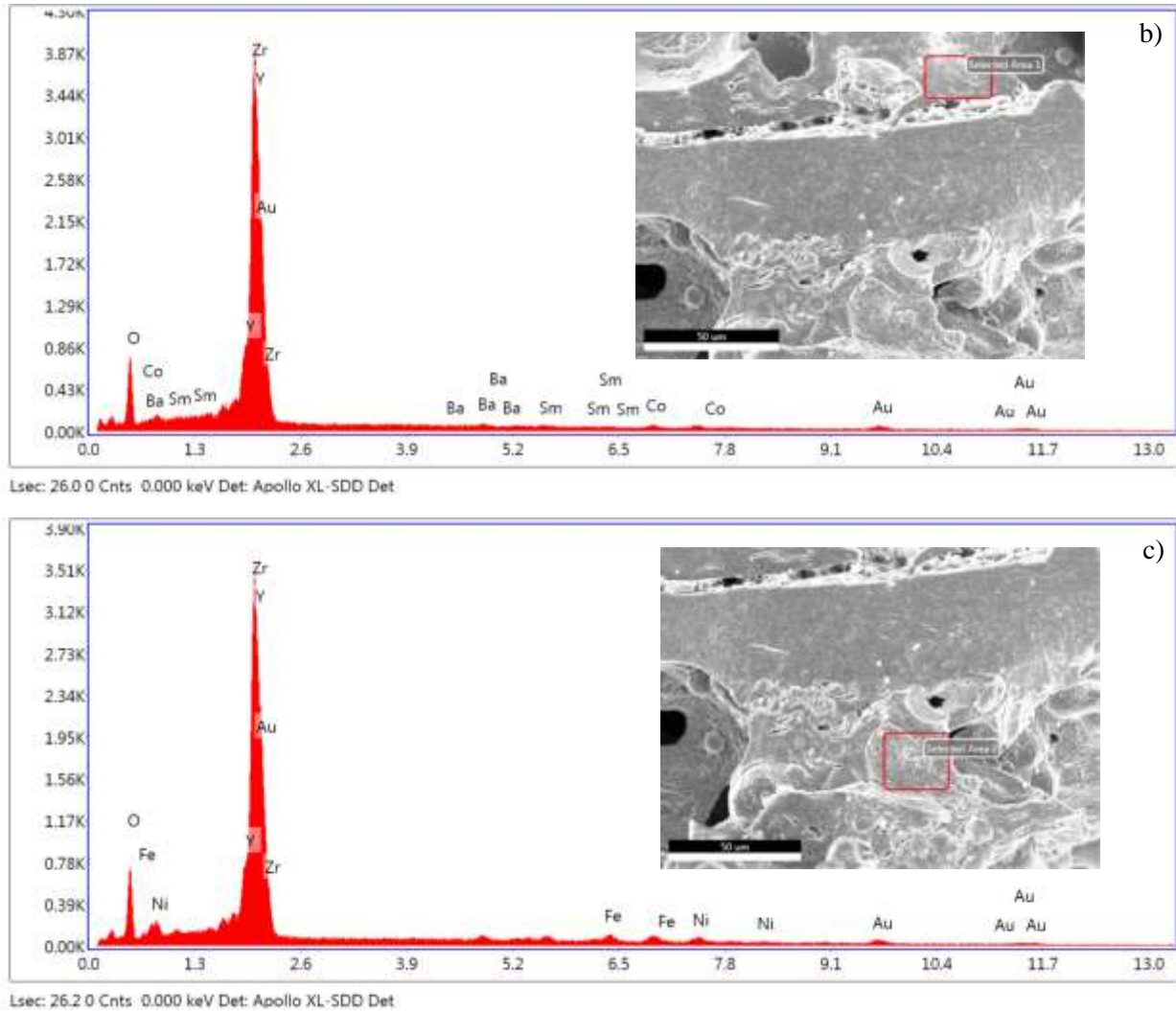


Figure 4.14 – EDX results for a) electrolyte region; b) cathode scaffold region; c) anode transition region.

4.2.2 Electrochemical Performance of Full MS-SOFC Cell with Cathode Scaffold

Figure 4.15 shows the polarization curve and power density of a cell prepared as described for Cell 2 in Table 4.2. The results are significantly better than for the stand-alone cathode configuration, but lower than published performance. A very good OCV (1.1 V) was obtained, but the voltage drops faster when current is drawn than in published results. Here the limiting current density close to 500 mA/cm^2 , and the maximum power density is about 138 mW/cm^2 . The corresponding EIS results are shown in Figure 4.16. This figure shows an ohmic resistance of $\sim 1.92 \text{ } \Omega \cdot \text{cm}^2$, which is very high and which points to some issues with the electrolyte, which dense enough to prevent leak through the cell (as indicated by the high OCV), but not dense enough to provide better ionic conductivity. The polarization resistance ($1.42 \text{ } \Omega \cdot \text{cm}^2$) and Area

Specific Resistance (ASR) ($2.64 \Omega \cdot \text{cm}^2$) are also higher than published data, which indicates considerable possibility for improvement. Figure 4.17 presents the corresponding SEM micrograph.

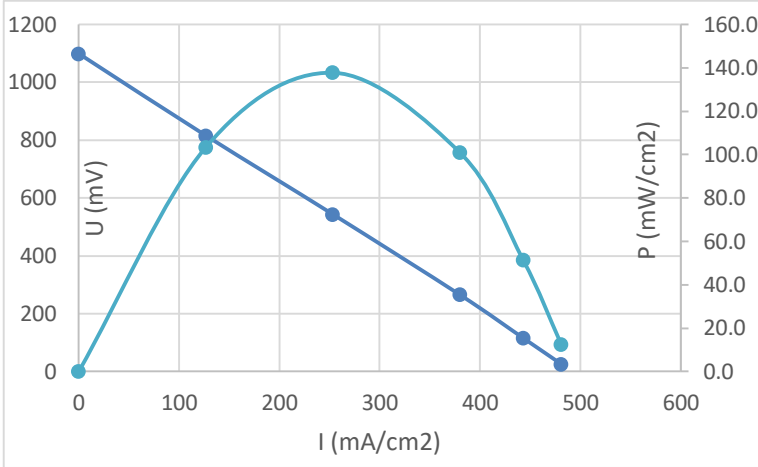


Figure 4.15 – Polarization and power density plot for a cell with cathode scaffold. 40% H₂ (balance argon), cell temperature ~775°C (furnace temperature of 750°C). Cell according to cell 2 in Table 2.1.

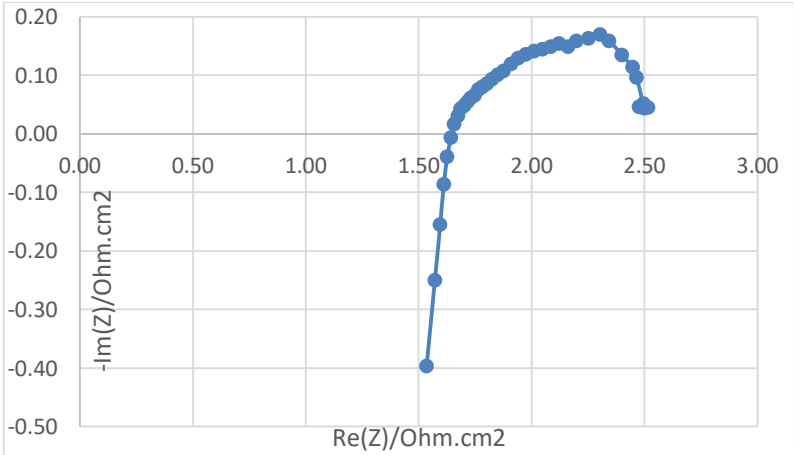


Figure 4.16 – Nyquist plot a cell with cathode scaffold. 40% H₂ (balance argon), cell temperature ~775°C (furnace temperature of 750°C). Cathode scaffold made of porous YSZ (according to Cell 2 in Table 2.1).

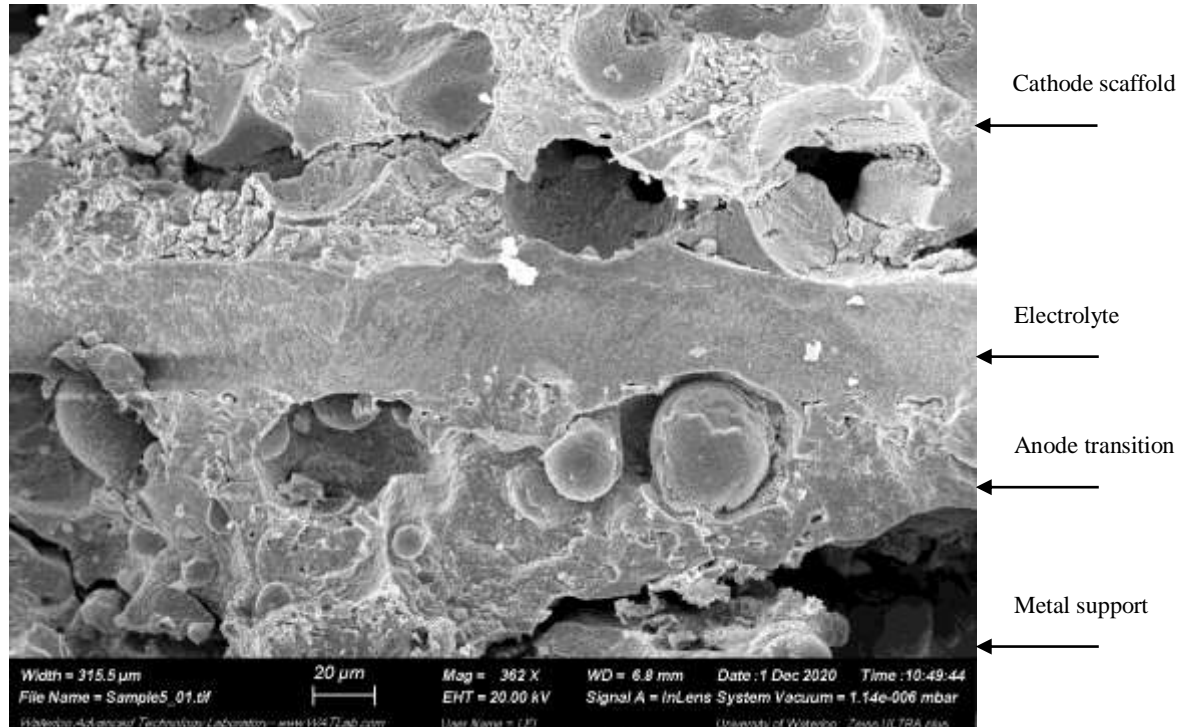


Figure 4.17 – SEM micrograph for spent cell with cathode scaffold. 40% H₂ (balance argon), cell temperature ~775°C (furnace temperature of 750°C). Cathode scaffold made of porous YSZ (according to Cell 2 in Table 2.1).

An expected reason for the large polarization is the fact that the porous cathode scaffold is made of YSZ, which is known for not conducting electricity. And, therefore, it is hypothesized that only the cathode materials near the current collector participate in the electrochemical reaction. It was seen in section 4.2.1 that replacing YSZ by SDC (a mixed ionic and electronic conductor) does not lead to a good cell because of the change in the ceria oxidation state, which affects the structure of the scaffold. It was then decided to consider a composite cathode scaffold made of YSZ and SDC, the bulk being YSZ to maintain a strong and stable structure and the SDC's function being mostly to conduct the electrons between the electrochemical reaction sites and the current collector.

A cell was manufactured with a scaffold composed of 50% SDC and 50% YSZ, but unfortunately, after co-sintering, this cell was broken and “bubbles” were apparent on the cathode surface, as seen in Figure 4.18a; this cell was not tested for its electrochemical performance.

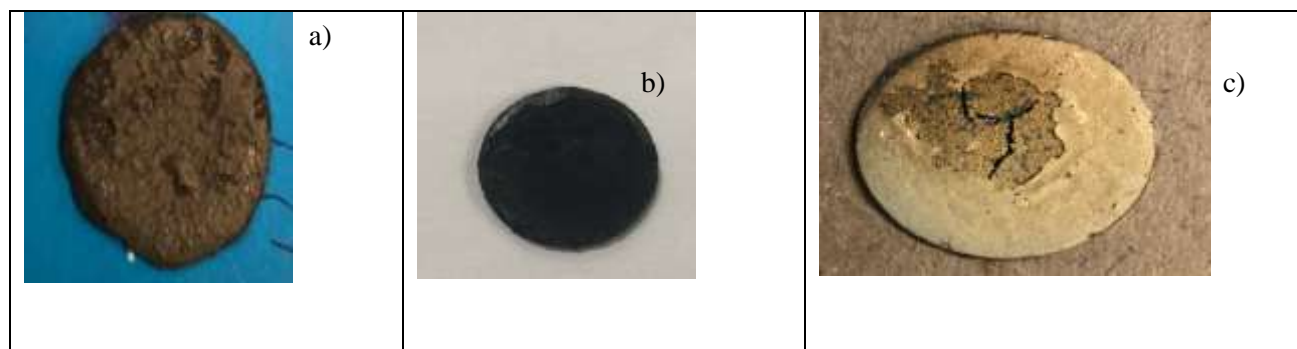


Figure 4.18 – Picture of cell with cathode scaffold with different amounts of SDC after co-sintering; a) 50% SDC/50% YSZ with infiltrated cathode, b) 10% SDC/90% YSZ with infiltrated cathode, and c) 5% SDC/95% YSZ after co-sintering.

The amount of SDC was then reduced to 25% and Figure 4.19 shows the polarization and power density curves for a composite cathode scaffold made of 25% SDC/75% YSZ. Note that visually, one could still see some sort of “bubbles” on the surface of the sintered scaffold. Figure 4.19 shows that the OCV (~ 770 mV) is not as good as with the porous YSZ scaffold, which indicate that the presence of 25% SDC in the scaffold may affect somewhat the densification of the electrolyte (e.g. through difference in shrinking behavior). Also, the maximum power density (close to 90 mW/cm^2) and limiting current density (400 mA/cm^2) are lower than with the cathode YSZ porous scaffold. On the other hand, the EIS results (Figure 4.20) indicates that the ohmic resistance ($1.56 \Omega \cdot \text{cm}^2$), although still high, is lower than for the YSZ scaffold. And more important, the polarization resistance (distance between each end of the arc at intercept of zero) ($\sim 93 \Omega \cdot \text{cm}^2$) and Area Specific Resistance (ASR) ($1.97 \Omega \cdot \text{cm}^2$) are lower in the case of 25% SDC in the scaffold than for pure YSZ ($\sim 1.42, 2.64 \Omega \cdot \text{cm}^2$). This indicates that indeed the presence of SDC helped reducing the polarization resistance. Figure 4.21 shows the corresponding SEM micrograph (Figure 4.21a) and EDX results in the electrolyte (Figure 4.21b), cathode scaffold (4.21c) and anode transition (4.21d). The SEM micrograph clearly shows a crack in the electrolyte, which likely explains the lower OCV, but the overall microstructure of the cathode scaffold with 25% SDC is not much different from that without SDC (see Figure 4.17). Again, the anode transition seems too porous, not allowing for complete intimate contact between the anode and the electrolyte. Figure 4.21b indicate the presence of samarium and cobalt, when one would expect only yttria and zirconia; since no ceria is detected, one can rule out the SDC, and thus those likely originate from the infiltrated cathode solution. In the fresh sample, no such species were detected (see Figure 4.14a) and therefore, this may be indicative of samarium and cobalt migrating from the

cathode to the electrolyte during cell operation. Figure 4.21c shows many additional species from what was present in the fresh sample (see Figure 4.14c), most notably the components (samarium, barium, cobalt) present in the cathode solution; it is difficult to assume that so much of those cathode solution would migrate during the fairly short operation of the cell, and it is more likely that some of the cathode solution “spilled” into the anode/metal support during the impregnation process, either from the side of the cell or through some cracks in the electrolyte.

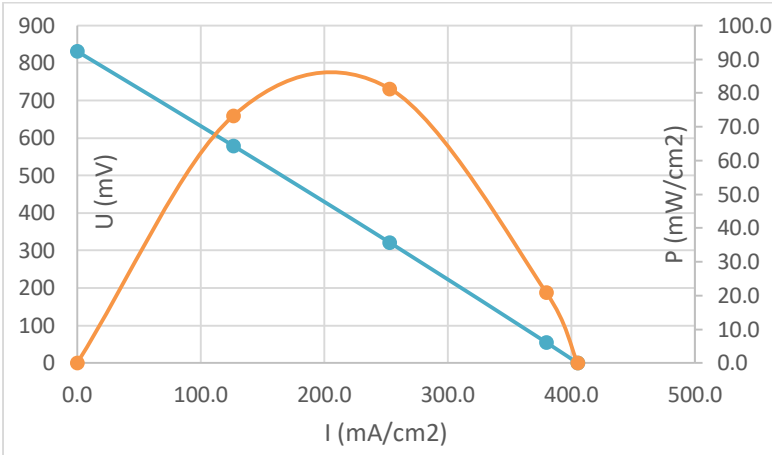


Figure 4.19 – Polarization and power density plot for a cell with cathode scaffold. 38% H₂ (balance argon), cell temperature ~774°C (furnace temperature of 750°C). Cathode scaffold made of porous 25%SDC/75% YSZ.

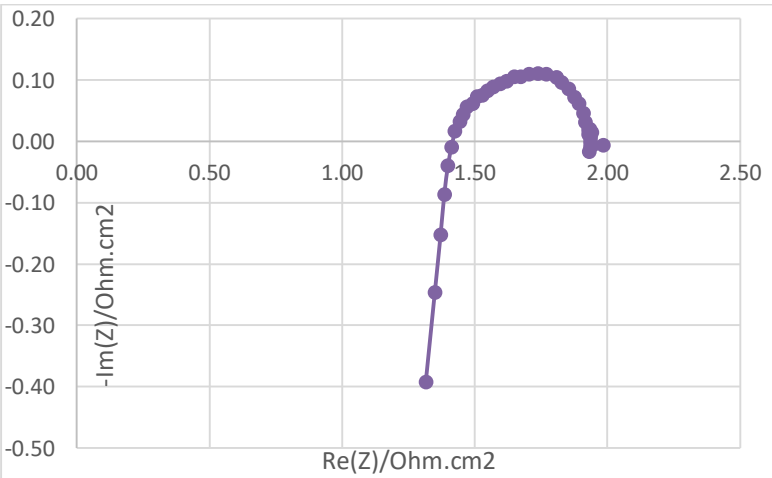
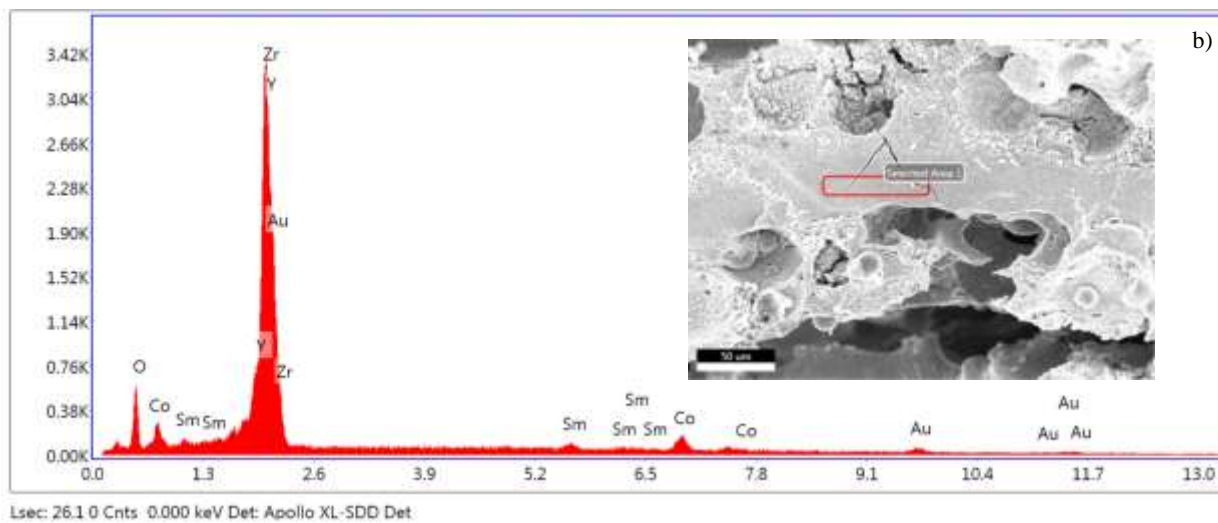
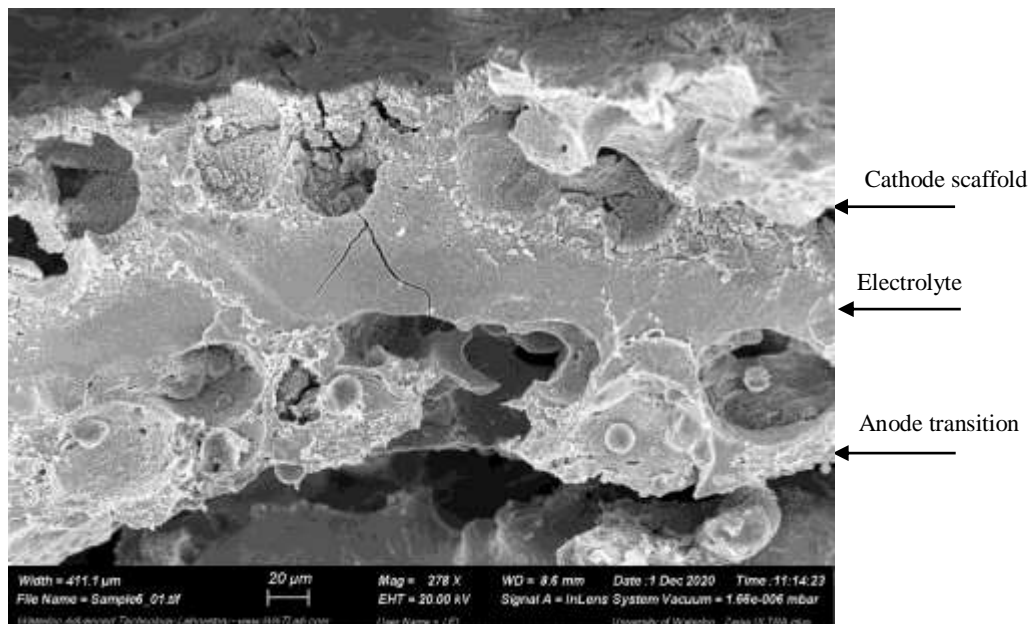


Figure 4.20 – Nyquist plot a cell with cathode scaffold. 38% H₂ (balance argon), cell temperature ~774°C (furnace temperature of 750°C). Cathode scaffold made of porous 25%SDC/75% YSZ.



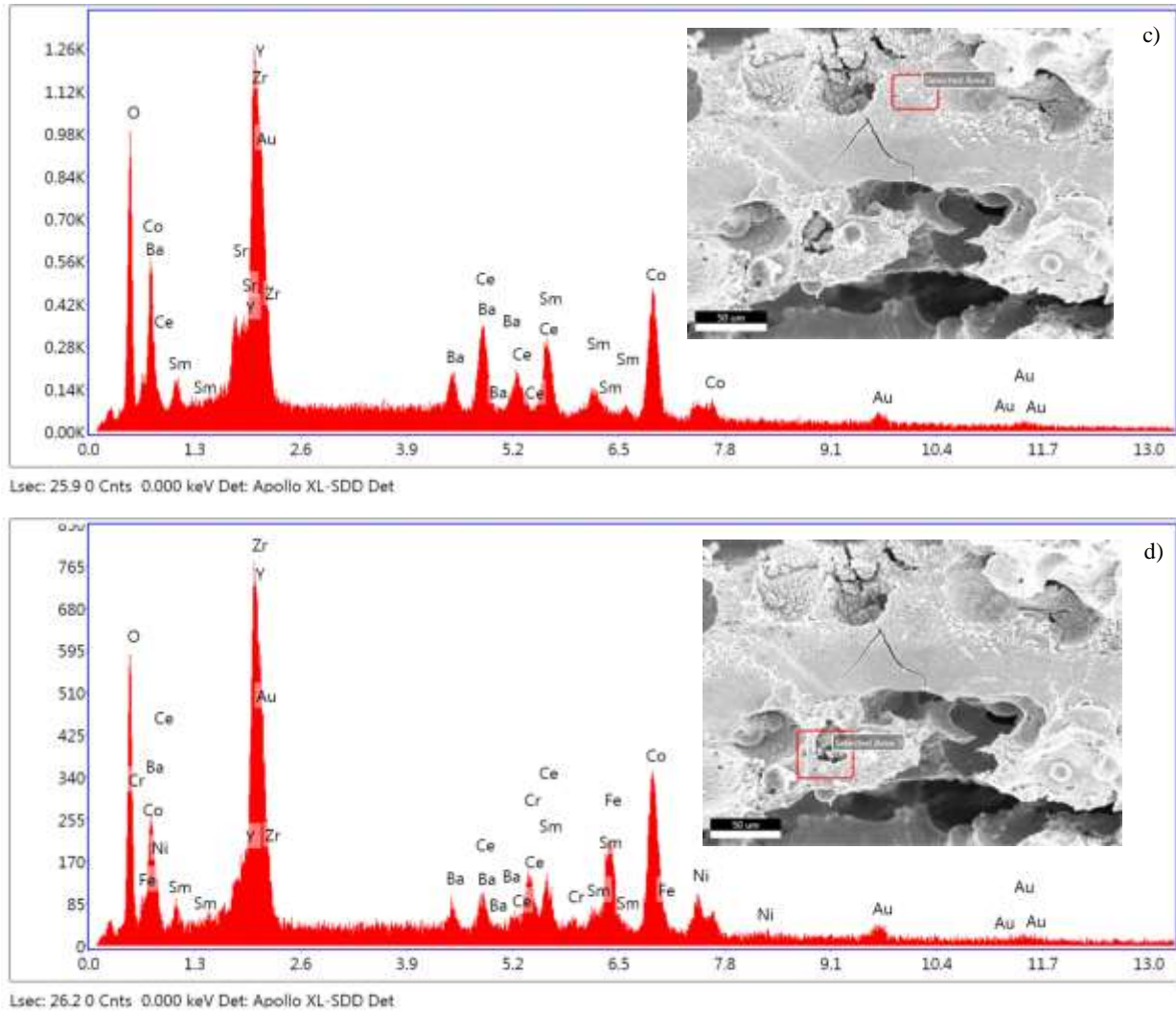


Figure 4.21 – Spent cell with cathode scaffold. 38% H₂ (balance argon), cell temperature ~774°C (furnace temperature of 750°C). Cathode scaffold made of porous 25%SDC/75%YSZ. a) SEM micrograph; b) EDX results for electrolyte region; c) EDX results for cathode scaffold region; d) EDX results for anode transition results.

Considering the non-smooth aspect of the SDC/YSZ composite scaffold surface in the presence of at least 25% SDC, it was decided to further reduce the amount of SDC, keeping in mind that the primary purpose of SDC is to conduct electrons. Attempts were made with 10% and 5% SDC and the resulting cells are shown in Figure 4.18b) and c), respectively. The cell with 10% SDC still showed a few “bubbles”, although much fewer than with 25% SDC. The cell with 5% SDC showed major cracks after co-sintering.

The EIS results above all showed large ohmic losses, which may point to a problem with the electrolyte (e.g. not as dense as expected). In order to address this problem and investigate whether one can reduce the ohmic losses, longer co-sintering times (e.g. 5 or 4 hours compared to 2 hours) were investigated with the aim at further densifying the electrolyte. Two cells were prepared, both with pure YSZ cathode scaffold: the first cell was co-sintered for 4 hours and the second one for 5 hours. For the second cell, the amount of YSZ in the electrolyte slurry was also increased slightly to 75wt% (9 g) as opposed to 72.7wt% (8 g, as per Table 3.2). The resulting two cells (Figure 4.22) were flat and without noticeable delamination. The cell sintered for 5 hours showed a slight crack on one side, but was mostly intact, whereas the cell sintered for 4 hours did not show any cracks. Both cells were tested for their electrochemical performance. Surprisingly, the cell sintered for 4 hours, and which looked quite good visually showed no OCV at all! The reason for this is unclear, but clearly, something went wrong with that particular cell. For the cell sintered for 5 hours, the polarization curve and EIS results for a feed of 29% H₂ is shown in Figure 4.23 and Figure 4.24, respectively. Those figures can be directly compared with Figures 4.8 and 4.9, the main difference being the sintering time. Clearly, here increasing the sintering time had a negative effect with lower OCV (620 mV compared to 1100 mV), lower maximum power density (38 mW in comparison to 138 mW.cm⁻²), and lower ohmic resistance (1.8 Ω.cm² compared to 1.92 Ω.cm²). This was definitely not expected: one reason could be the cathode solution used, which was a bit “old” and changed somewhat in appearance (more pink and not as transparent); another reason, maybe that the contact between the metal support and the rest of the cell may have degraded when sintering for a longer period, as seen from the crack part in Figure 4.22b. Figure 4.25 show the SEM of the spent cell. This figure confirms a very bad contact between the metal support and the rest of the cell, as it looks nearly delaminated. As the sintering duration is extended, the metal support shrinks more, which may lead to cell warping or near delamination as it is the case here. To address the poor contact, new cells with more graded composition layers between metal support and electrolyte should be tried.



Figure 4.22. Cell with prolonged sintering time; a) 4 hours sintering and 72.7wt% YSZ in electrolyte slurry, b) 5 hours sintering and 75wt% YSZ in electrolyte slurry.

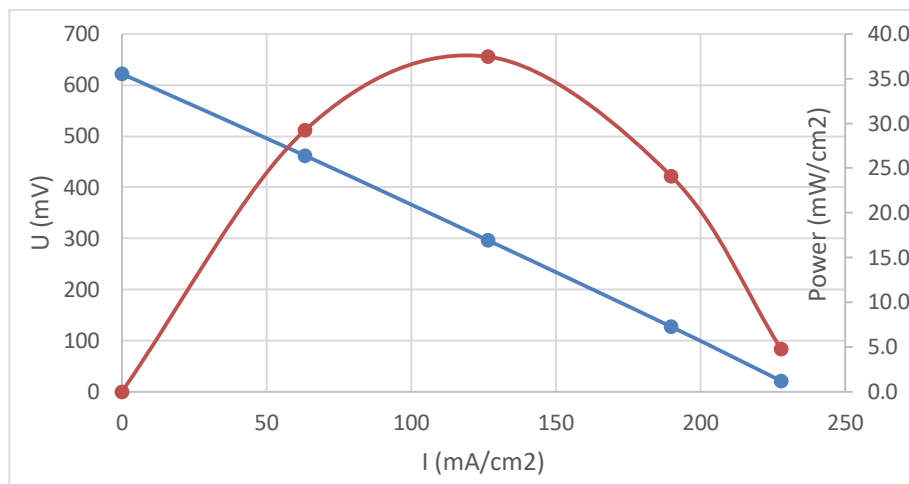


Figure 4.23 – Polarization and power density plot for a cell with cathode scaffold. 29% H₂ (balance argon), cell temperature ~771°C (furnace temperature of 750°C). Cell according to cell 2 in Table 2.1, except sintered for 5 hours (and 75% YSZ in electrolyte slurry).

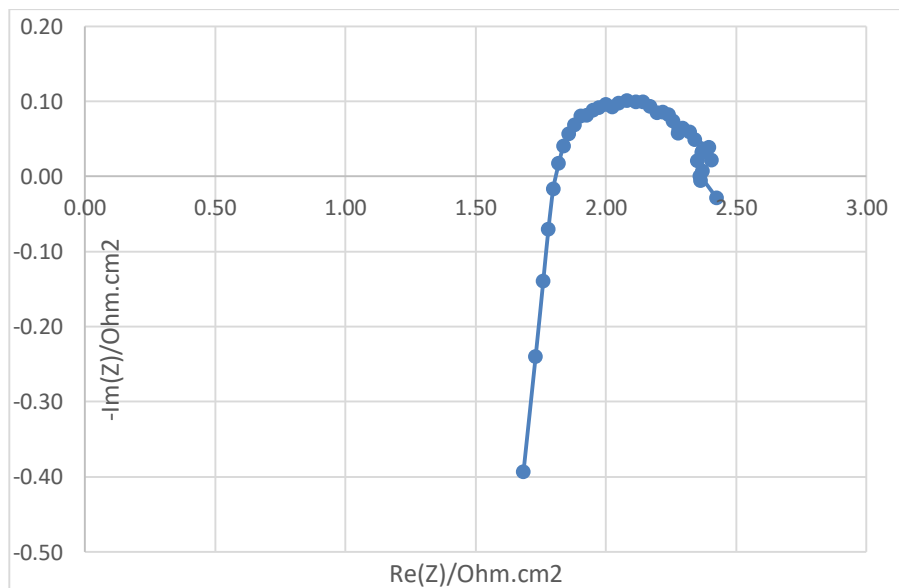


Figure 4.24 – Nyquist plot a cell with cathode scaffold. 29% H₂ (balance argon), cell temperature ~771°C (furnace temperature of 750°C). Cell according to cell 2 in Table 2.1, except sintered for 5 hours (and 75% YSZ in electrolyte slurry).

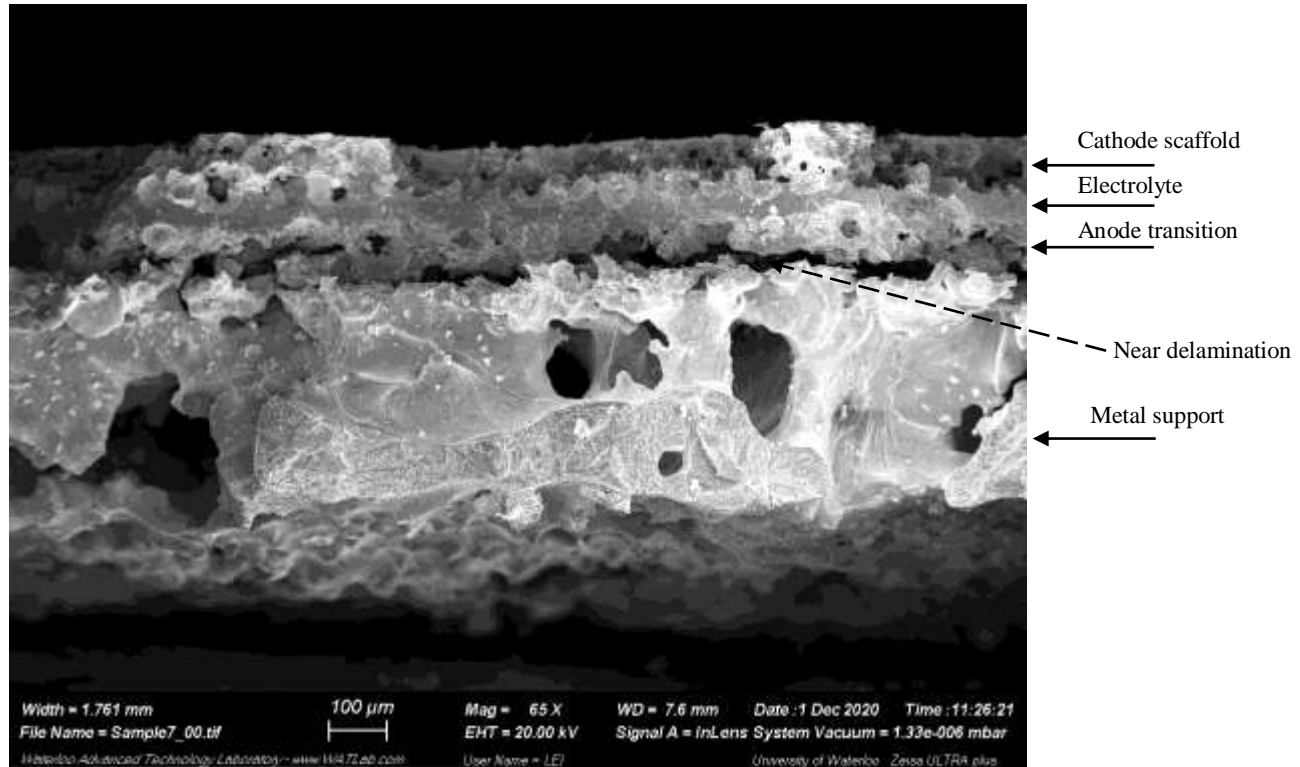


Figure 4.25 – SEM micrograph of the spent cell with cathode scaffold. 29% H₂ (balance argon), cell temperature ~771°C, sintered for 5 hours at 1325°C.

In conclusion, the MS-SOFC configuration with cathode scaffold shows promising results, but more fine tuning to determine the right amount of SDC in the scaffold is required; the amount should be small enough as to not affect the integrity of the structure during sintering in reducing atmosphere, as well as not negatively affecting the densification of the electrolyte, but sufficiently high to provide enough electronic conductivity to the current collector. In addition, more tuning should be done when considering prolonged sintering up to 5 hours.

Chapter 5 Conclusions and Recommendations

5.1 Conclusions

The main focus of this study was on the cathode, for which two different types of cathode material/preparation were considered: 1) ex-situ sintering of a printed stand-alone cathode layer and 2) infiltration of cathode materials on a cathode scaffold. For the first type, $\text{La}_{0.58}\text{Sr}_{0.4}\text{Co}_{0.2}\text{Fe}_{0.8}\text{O}_{3-\delta}$ mixed with Gadolinium Doped Ceria (LSFC-GDC) was used as cathode materials. For the second type, Samarium Barium Strontium Cobalt oxide (SBSCo) was infiltrated in the cathode scaffold. Cell performance was evaluated through IV curve, power density, and electrochemical impedance spectroscopy.

In this thesis, SS-430L and YSZ have been used as metal support and electrolyte, respectively. MS-SOFC full cells were fabricated without visible cracks and without in-situ cathode sintering which was a good result in this work.

The performance of structure 1 was very poor (e.g. max. power density less than 5 mW/cm^2), so some modifications were made to improve performance (e.g. no cathode transition layer, increased sintering time), but to no avail so far. There is still much work to do to improve the performance of the stand-alone cathode layer structure. Clearly, the cathode transition layer causes significant polarization losses, but at the same time helps in increasing the OCV. On the other hand, in the absence of the cathode transition layer, the polarization losses are lowered, but also is the OCV. The challenge is thus to manufacture a cell with good OCV (fully dense electrolyte) without the presence of a cathode transition layer.

The MS-SOFC configuration with cathode scaffold shows promising results. Structure 2 (with cathode scaffold) yielded much better performance (e.g. max. power density of 140 mW/cm^2), but still lower than published and target results of about 1000 mW/cm^2 . Consequently, some modifications were made to improve performance (e.g. add SDC in the porous scaffold, increased sintering time), but without much success, even though SDC addition showed a decrease in polarization resistance.

5.2 Recommendations

5.2.1 For Porous Cathode Scaffold Structure:

1. Reduce SDC content below 25% in the porous scaffold, possibly to very low concentration, recalling that the main function of SDC here is to conduct electrons.
2. Fine tune layers compositions (including slurry composition) in order to increase co-sintering duration up to 5 hours, while obtaining a flat cell without cracks.

5.2.2 For Stand Alone Cathode Structure

1. Because of high ex-situ cathode sintering temperature may lead to anode catalyst coarsening, deposit the cathode prior to infiltrate the anode.
2. Use more refined graded metal support/anode transition layers.

References

- [1] Satardekar P. Materials Development for the Fabrication of Metal-Supported Solid Oxide Fuel Cells by Co-sintering (Doctoral dissertation, University of Trento). 2014.
- [2] BP. BP Statistical Review of World Energy 2019. Br Pet 2019:1–52. doi: <https://www.bp.com/content/dam/bp/business-sites/en/global/corporate/pdfs/energy-economics/statistical-review/bp-stats-review-2019-full-report.pdf>
- [3] AbolhosSseini H, Heshmati A, Altmann J. A review of renewable energy supply and energy efficiency technologies. IZA Discuss Pap Ser 2014:1–36.
- [4] Global Temperature | Vital Signs – Climate Change: Vital Signs of the Planet n.d. doi: <https://climate.nasa.gov/vital-signs/global-temperature/>(accessed December 10, 2019).
- [5] Handbook FC. EG&G Technical Services, Inc. US Department of Energy, Office of Fossil Energy, National Energy Technology Laboratory-Morgantown, West Virginia. 2004 Nov.
- [6] Toor SY. High Temperature Co-Sintering for Metal Supported-Solid Oxide Fuel Cell Fabrication. 2019.
- [7] Wisniak J. Electrochemistry and fuel cells: the contribution of William Robert Grove. Indian Journal of History of Science. 2015;50:476-90. doi: 10.16943/ijhs/2015/v50i4/48318.
- [8] Möbius HH. On the history of solid electrolyte fuel cells. Journal of solid state electrochemistry. 1997 Jul 1;1(1):2-16. doi:10.1007/s100080050018.
- [9] Weppner W. Tetragonal zirconia polycrystals-a high performance solid oxygen ion conductor.[ZrO [sub 2]].Solid State Ionics. 1992;52(1-3):15–21.
- [10] Steele BC. Interfacial reactions associated with ceramic ion transport membranes. Solid State Ionics. 1995 Jan 1;75:157-65.
- [11] Arregui Buldain A. Stability studies of critical components in SOFC technologies (Doctoral dissertation, University of Trento).2013
- [12] Zhou Y. Study on Fabrication and Performance of Metal-Supported Solid Oxide Fuel Cells.

Springer; 2017 Oct 26. doi: <https://doi.org/10.1007/978-981-10-6617-7>

- [13] Chung KS. Fabrication and Characterization of Metal-support for Solid Oxide Fuel Cells (MSOFCs) (Master's thesis, University of Waterloo). 2016
- [14] Eveloy V, Rodgers P, Qiu L. Integration of an atmospheric solid oxide fuel cell-gas turbine system with reverse osmosis for distributed seawater desalination in a process facility. *Energy Conversion and Management*. 2016 Oct 15;126:944-59. doi: <https://doi.org/10.1016/j.enconman.2016.08.026>.
- [15] Ghirardo F, Santin M, Traverso A, Massardo A. Heat recovery options for onboard fuel cell systems. *International Journal of Hydrogen Energy*. 2011 Jul 1;36(13):8134-42. doi: <https://doi.org/10.1016/j.ijhydene.2011.01.111>.
- [16] Hosseini M, Dincer I, Ahmadi P, Avval HB, Ziaasharhagh M. Thermodynamic modelling of an integrated solid oxide fuel cell and micro gas turbine system for desalination purposes. *International Journal of Energy Research*. 2013 Apr;37(5):426-34. doi: <https://doi.org/10.1002/er.1945>
- [17] Najafi B, Shirazi A, Aminyavari M, Rinaldi F, Taylor RA. Exergetic, economic and environmental analyses and multi-objective optimization of an SOFC-gas turbine hybrid cycle coupled with an MSF desalination system. *Desalination*. 2014 Feb 3;334(1):46-59. doi: <https://doi.org/10.1016/j.desal.2013.11.039>
- [18] Meratizaman M, Monadizadeh S, Amidpour M. Simulation and economic evaluation of small-scale SOFC-GT-MED. *Desalination and Water Treatment*. 2016 Mar 2;57(11):4810-31. doi: <https://doi.org/10.1080/19443994.2014.1002432>.
- [19] Meratizaman M, Monadizadeh S, Ebrahimi A, Akbarpour H, Amidpour M. Scenario analysis of gasification process application in electrical energy-freshwater generation from heavy fuel oil, thermodynamic, economic and environmental assessment. *International Journal of Hydrogen Energy*. 2015 Feb 19;40(6):2578-600. doi: <https://doi.org/10.1016/j.ijhydene.2014.12.072>.
- [20] Reyhani HA, Meratizaman M, Ebrahimi A, Purali O, Amidpour M. Thermodynamic and economic optimization of SOFC-GT and its cogeneration opportunities using generated syngas from heavy fuel oil gasification. *Energy*. 2016 Jul 15;107:141-64. doi: <https://doi.org/10.1016/j.energy.2016.04.010>.
- [21] Al-Hallaj S, Alasfour F, Parekh S, Amiruddin S, Selman JR, Ghezal-Ayagh H. Conceptual design of a novel hybrid fuel cell/desalination system. *Desalination*. 2004 Mar 25;164(1):19-31. doi: <https://doi.org/10.1016/j.desal.2004.03.010>

[https://doi.org/10.1016/S0011-9164\(04\)00152-3](https://doi.org/10.1016/S0011-9164(04)00152-3)

- [22] Lisbona P, Uche J, Serra L. High-temperature fuel cells for fresh water production. *Desalination*. 2005 Nov 1;182(1-3):471-82. doi: <https://doi.org/10.1016/j.desal.2005.03.025>
- [23] Choudhury A, Chandra H, Arora A. Application of solid oxide fuel cell technology for power generation—A review. *Renewable and Sustainable Energy Reviews*. 2013 Apr 1;20:430-42. doi: <https://doi.org/10.1016/j.rser.2012.11.031>
- [24] Buonomano A, Calise F, d'Accadia MD, Palombo A, Vicidomini M. Hybrid solid oxide fuel cells–gas turbine systems for combined heat and power: a review. *Applied Energy*. 2015 Oct 15;156:32-85. doi: <https://doi.org/10.1016/j.apenergy.2015.06.027>
- [25] Zhao Y, Shah N, Brandon N. Comparison between two optimization strategies for solid oxide fuel cell–gas turbine hybrid cycles. *International Journal of Hydrogen Energy*. 2011 Aug 1;36(16):10235-46. doi: <https://doi.org/10.1016/j.ijhydene.2010.11.015>
- [26] Chinda P, Brault P. The hybrid solid oxide fuel cell (SOFC) and gas turbine (GT) systems steady state modeling. *International Journal of Hydrogen Energy*. 2012 Jun 1;37(11):9237-48. doi: <https://doi.org/10.1016/j.ijhydene.2012.03.005>
- [27] Tanasini P, Cannarozzo M, Costamagna P, Faes A, Van Herle J, Hessler-Wyser A, Cominellis C. Experimental and theoretical investigation of degradation mechanisms by particle coarsening in SOFC electrodes. *Fuel Cells*. 2009 Oct;9(5):740-52. doi: <https://doi.org/10.1002/fuce.200800192>
- [28] Lee JH, Moon H, Lee HW, Kim J, Kim JD, Yoon KH. Quantitative analysis of microstructure and its related electrical property of SOFC anode, Ni–YSZ cermet. *Solid State Ionics*. 2002 May 1;148(1-2):15-26. doi: [https://doi.org/10.1016/S0167-2738\(02\)00050-4](https://doi.org/10.1016/S0167-2738(02)00050-4)
- [29] Villarreal I, Jacobson C, Leming A, Matus Y, Visco S, De Jonghe L. Metal-supported solid oxide fuel cells. *Electrochemical and Solid State Letters*. 2003 Jun 25;6(9):A178. doi: 10.1149/1.1592372.
- [30] Kennouche D, Chen-Wiegart YC, Cronin JS, Wang J, Barnett SA. Three-dimensional microstructural evolution of Ni-yttria-stabilized zirconia solid oxide fuel cell anodes at elevated temperatures. *Journal of the Electrochemical Society*. 2013 Oct 10;160(11):F1293. doi: 10.1149/2.084311jes.

- [31] Brandon N. Solid oxide fuel cell lifetime and reliability: critical challenges in fuel cells. Academic Press; 2017 May 23.
- [32] Ren M. Development of porous metal-supported solid oxide fuel cells (Doctoral dissertation). 2013
- [33] Ahmed K, Foger K. Kinetics of internal steam reforming of methane on Ni/YSZ-based anodes for solid oxide fuel cells. *Catalysis today*. 2000 Dec 25;63(2-4):479-87. doi: [https://doi.org/10.1016/S0920-5861\(00\)00494-6](https://doi.org/10.1016/S0920-5861(00)00494-6)
- [34] Pihlatie M, Kaiser A, Mogensen M. Mechanical properties of NiO/Ni–YSZ composites depending on temperature, porosity and redox cycling. *Journal of the European Ceramic Society*. 2009 Jun 1;29(9):1657-64. doi: <https://doi.org/10.1016/j.jeurceramsoc.2008.10.017>
- [35] Cassidy M, Lindsay G, Kendall K. The reduction of nickel-zirconia cermet anodes and the effects on supported thin electrolytes. *Journal of Power Sources*. 1996 Jul 1;61(1-2):189-92. doi: [https://doi.org/10.1016/S0378-7753\(96\)02359-2](https://doi.org/10.1016/S0378-7753(96)02359-2)
- [36] Waldbillig D, Wood A, Ivey DG. Electrochemical and microstructural characterization of the redox tolerance of solid oxide fuel cell anodes. *Journal of Power Sources*. 2005 Aug 18;145(2):206-15. doi: <https://doi.org/10.1016/j.jpowsour.2004.12.071>
- [37] Tikekar NM, Armstrong TJ, Virkar AV. Reduction and reoxidation kinetics of nickel-based SOFC anodes. *Journal of the Electrochemical Society*. 2006 Feb 13;153(4):A654. doi: 10.1149/1.2167949.
- [38] Wood A, Pastula M, Waldbillig D, Ivey DG. Initial testing of solutions to redox problems with anode-supported SOFC. *Journal of the Electrochemical Society*. 2006 Aug 21;153(10):A1929. doi: 10.1149/1.2240085.
- [39] Faes A, Hessler-Wyser A, Zryd A. A review of RedOx cycling of solid oxide fuel cells anode. *Membranes*. 2012 Sep;2(3):585-664. doi: <https://doi.org/10.3390/membranes2030585>
- [40] Sun B, Rudkin RA, Atkinson A. Effect of Thermal Cycling on Residual Stress and Curvature of Anode-Supported SOFCs. *Fuel Cells*. 2009 Dec;9(6):805-13. doi: <https://doi.org/10.1002/fuce.200800133>.
- [41] Tucker MC. Progress in metal-supported solid oxide fuel cells: A review. *Journal of Power Sources*. 2010 Aug 1;195(15):4570-82. doi: <https://doi.org/10.1016/j.jpowsour.2010.02.035>

- [42] Williams KR, Smith JG, inventors; Shell Oil Co, assignee. Fuel cells with solid state electrolytes. United States patent US 3,464,861. 1969 Sep 2.
- [43] Szabo P, Arnold J, Franco T, Gindrat M, Refke A, Zagst A, Ansar A. Progress in the metal supported solid oxide fuel cells and stacks for APU. ECS transactions. 2009 Sep 25;25(2):175.
- [44] Gupta M, Weber A, Markocsan N, Gindrat M. Electrochemical Performance of Plasma Sprayed Metal Supported Planar Solid Oxide Fuel Cells. Journal of The Electrochemical Society. 2016 Jul 12;163(9):F1059. doi: : 10.1149/2.0791609jes.
- [45] Tucker MC, Jacobson CP, De Jonghe LC, Visco SJ. A braze system for sealing metal-supported solid oxide fuel cells. Journal of Power Sources. 2006 Oct 6;160(2):1049-57. doi: <https://doi.org/10.1016/j.jpowsour.2006.02.067>.
- [46] Tucker MC. Durability of symmetric-structured metal-supported solid oxide fuel cells. Journal of Power Sources. 2017 Nov 30;369:6-12. doi: <https://doi.org/10.1016/j.jpowsour.2017.09.075>.
- [47] Park YM, Kim JH, Kim H. In situ sinterable cathode with nanocrystalline La_{0.6}Sr_{0.4}Co_{0.2}Fe_{0.8}O_{3-δ} for solid oxide fuel cells. International journal of hydrogen energy. 2011 May 1;36(9):5617-23. doi: <https://doi.org/10.1016/j.ijhydene.2011.02.011>.
- [48] Nielsen J, Hjalmarsson P, Hansen MH, Blennow P. Effect of low temperature in-situ sintering on the impedance and the performance of intermediate temperature solid oxide fuel cell cathodes. Journal of Power Sources. 2014 Jan 1;245:418-28. doi: <https://doi.org/10.1016/j.jpowsour.2013.06.067>.
- [49] Zhou Y, Zhang Z, Yuan C, Li J, Xia C, Zhan Z, Wang S. Metal-supported solid oxide fuel cells with in-situ sintered (Bi₂O₃)_{0.7} (Er₂O₃)_{0.3}-Ag composite cathode. international journal of hydrogen energy. 2013 Dec 13;38(36):16579-83. doi: <https://doi.org/10.1016/j.ijhydene.2013.02.068>.
- [50] Zhou Y, Han D, Yuan C, Liu M, Chen T, Wang S, Zhan Z. Infiltrated SmBa_{0.5}Sr_{0.5}Co₂O_{5+δ} cathodes for metal-supported solid oxide fuel cells. Electrochimica Acta. 2014 Dec 10;149:231-6. doi: <https://doi.org/10.1016/j.electacta.2014.10.067>
- [51] Zhan Z, Zhou Y, Wang S, Liu X, Meng X, Wen T. Nanostructure electrodes for metal-supported solid oxide fuel cells. ECS transactions. 2013 Oct 6;57(1):925.

- [52] Jung HG, Sun YK, Jung HY, Park JS, Kim HR, Kim GH, Lee HW, Lee JH. Investigation of anode-supported SOFC with cobalt-containing cathode and GDC interlayer. *Solid State Ionics*. 2008 Sep 30;179(27-32):1535-9. doi: <https://doi.org/10.1016/j.ssi.2008.01.063>.
- [53] Ralph JM, Rossignol C, Kumar R. Cathode materials for reduced-temperature SOFCs. *Journal of Electrochemical Society*. 2003 Sep 22;150(11):A1518. doi: 10.1149/1.1617300.
- [54] Krishnan VV. Recent developments in metal-supported solid oxide fuel cells. *Wiley Interdisciplinary Reviews: Energy and Environment*. 2017 Sep;6(5):e246. doi: <https://doi.org/10.1002/wene.246>.
- [55] Leah RT, Bone A, Lankin M, Selcuk A, Rahman M, Clare A, Rees L, Phillip S, Mukerjee S, Selby M. Ceres power steel cell technology: rapid progress towards a truly commercially viable SOFC. *ECS Transactions*. 2015 Jun 2;68(1):95.
- [56] Li CJ, Li CX, Ning XJ. Performance of YSZ electrolyte layer deposited by atmospheric plasma spraying for cermet-supported tubular SOFC. *Vacuum*. 2004 Apr 19;73(3-4):699-703. doi: <https://doi.org/10.1016/j.vacuum.2003.12.096>.
- [57] Li CJ, Ohmori A. Relationships between the microstructure and properties of thermally sprayed deposits. *Journal of thermal spray technology*. 2002 Sep 1;11(3):365-74.
- [58] Choi JH, Lee T, Choi M, Yoo YS, Baek SW, Bae J. Long-term performance of anode-supported SOFC integrated with metal interconnect by joining process. *International journal of hydrogen energy*. 2010 May 1;35(9):4285-91. doi: <https://doi.org/10.1016/j.ijhydene.2010.02.062>
- [59] Blennow P, Hjelm J, Klemens/T, Persson A, Brodersen K, Srivastava A, Frandsen H, Lundberg M, Ramousse S, Mogensen M. Development of planar metal supported SOFC with novel cermet anode. *ECS Transactions*. 2009 Sep 25;25(2):701.
- [60] Franco T, Schibinger K, Ilhan Z, Schiller G, Venskutonis A. Ceramic diffusion barrier layers for metal supported SOFCs. *Ecs Transactions*. 2007 May 25;7(1):771.
- [61] Cho HJ, Park YM, Choi GM. A flexible solid oxide fuel cell supported on the thin porous metal. *ECS Transactions*. 2009 Sep 25;25(2):695.
- [62] Minh NQ, Takahashi T. *Science and technology of ceramic fuel cells*. Elsevier; 1995 Aug 15.
- [63] Connor P. *Solid oxide fuels cells: facts and figures*. Irvine JT, editor. London: Springer; 2013. doi: 10.1007/978-1-4471-4456-4.

- [64] Yang ZG, Paxton DM, Weil KS, Stevenson JW, Singh P. Materials properties database for selection of high-temperature alloys and concepts of alloy design for SOFC applications. Pacific Northwest National Lab.(PNNL), Richland, WA (United States); 2002 Nov 24. doi: 10.2172/15010553.
- [65] Liu Z, Liu B, Ding D, Jiang Z, Xia C. Development of three-layer intermediate temperature solid oxide fuel cells with direct stainless steel based anodes. *International journal of hydrogen energy*. 2012 Mar 1;37(5):4401-5. doi: <https://doi.org/10.1016/j.ijhydene.2011.11.115>
- [66] Bateni MR, Wei P, Kesler O, Petric A. Characterization of aluminum coatings formed on porous ferritic stainless steels by pack cementation. *Materials and manufacturing processes*. 2013 Dec 2;28(12):1314-21. doi: <https://doi.org/10.1080/10426914.2013.852205>.
- [67] Reisert M, Berova V, Aphale A, Singh P, Tucker MC. Oxidation of porous stainless steel supports for metal-supported solid oxide fuel cells. *International Journal of Hydrogen Energy*. 2020 Nov 6;45(55):30882-97. doi: <https://doi.org/10.1016/j.ijhydene.2020.08.015>
- [68] Molin S, Kusz B, Gazda M, Jasinski P. Evaluation of porous 430L stainless steel for SOFC operation at intermediate temperatures. *Journal of Power sources*. 2008 Jun 15;181(1):31-7. doi: <https://doi.org/10.1016/j.jpowsour.2007.10.009>.
- [69] Dogdibegovic E, Wang R, Lau GY, Karimaghloo A, Lee MH, Tucker MC. Progress in durability of metal-supported solid oxide fuel cells with infiltrated electrodes. *Journal of Power sources*. 2019 Oct 15;437:226935. doi: <https://doi.org/10.1016/j.jpowsour.2019.226935>.
- [70] Ebbinghaus BB. Thermodynamics of gas phase chromium species: the chromium oxides, the chromium oxyhydroxides, and volatility calculations in waste incineration processes. *Combustion and Flame*. 1993 Apr 1;93(1-2):119-37. doi: [https://doi.org/10.1016/0010-2180\(93\)90087-J](https://doi.org/10.1016/0010-2180(93)90087-J)
- [71] Hilpert K, Das D, Miller M, Peck DH, Weiss R. Chromium vapor species over solid oxide fuel cell interconnect materials and their potential for degradation processes. *Journal of the Electrochemical Society*. 1996 Nov 1;143(11):3642.
- [72] Jablonski PD, Sears JS. The impact of alloy chemistry on the formation of a silicon-rich subscale on two classes of ferritic steels. *Journal of power sources*. 2013 Apr 15;228:141-50. doi: <https://doi.org/10.1016/j.jpowsour.2012.11.107>.
- [73] Hwang CS, Tsai CH, Hwang TJ, Chang CL, Yang SF, Lin JK. Novel Metal Substrates for High

- Power Metal-supported Solid Oxide Fuel Cells. *Fuel Cells*. 2016 Apr;16(2):244-51.doi: <https://doi.org/10.1002/fuce.201500216>.
- [74] Yang SF, Shie ZY, Hwang CS, Tsai CH, Chang CL, Huang TJ, Lee RY. Ni-Mo porous alloy fabricated as supporting component for metal-supported solid oxide fuel cell and cell performance. *ECS Transactions*. 2015 Jun 2;68(1):1849.
- [75] Karczewski J, Dunst KJ, Jasinski P, Molin S. High temperature corrosion and corrosion protection of porous Ni₂₂Cr alloys. *Surface and Coatings Technology*. 2015 Jan 15;261:385-90.doi: <https://doi.org/10.1016/j.surfcoat.2014.10.051>.
- [76] Molin S, Gazda M, Jasinski P. Coatings for improvement of high temperature corrosion resistance of porous alloys. *Journal of the European Ceramic Society*. 2011 Nov 1;31(14):2707-10.doi: <https://doi.org/10.1016/j.jeurceramsoc.2011.02.007>
- [77] Antepará I, Villarreal I, Rodríguez-Martínez LM, Lecanda N, Castro U, Laresgoiti A. Evaluation of ferritic steels for use as interconnects and porous metal supports in IT-SOFCs. *Journal of Power Sources*. 2005 Oct 10;151:103-7.doi: <https://doi.org/10.1016/j.jpowsour.2005.02.084>.
- [78] Sarasketa-Zabala E, Otaegi L, Rodríguez-Martínez LM, Álvarez MA, Burgos N, Castro F, Villarreal I. High temperature stability of porous metal substrates under highly humidified hydrogen conditions for metal supported Solid Oxide Fuel Cells. *Solid State Ionics*. 2012 Aug 20;222:16-22.doi: <https://doi.org/10.1016/j.ssi.2012.06.014>.
- [79] Mogensen M, Sammes NM, Tompsett GA. Physical, chemical and electrochemical properties of pure and doped ceria. *Solid State Ionics*. 2000 Apr 1;129(1-4):63-94.doi: [https://doi.org/10.1016/S0167-2738\(99\)00318-5](https://doi.org/10.1016/S0167-2738(99)00318-5)
- [80] Sarantaridis D, Atkinson A. Redox cycling of Ni-based solid oxide fuel cell anodes: a review. *Fuel cells*. 2007 Jun;7(3):246-58.doi: <https://doi.org/10.1002/fuce.200600028>
- [81] Rasmussen JF, Hagen A. The effect of H₂S on the performance of Ni–YSZ anodes in solid oxide fuel cells. *Journal of Power Sources*. 2009 Jun 15;191(2):534-41.doi: <https://doi.org/10.1016/j.jpowsour.2009.02.001>.
- [82] Kim KJ, Kim SJ, Choi GM. Y_{0.08}Sr_{0.88}TiO₃–CeO₂ composite as a diffusion barrier layer for stainless-steel supported solid oxide fuel cell. *Journal of Power Sources*. 2016 Mar 1;307:385-90.doi: <https://doi.org/10.1016/j.jpowsour.2015.12.130>.

- [83] Villarreal I, Rivas M, Rodriguez-Martinez LM, Otaegi L, Zabala A, Gomez N, Alvarez M, Antepará I, Arizmendiarieta N, Manzanedo J, Olave M. Tubular metal supported SOFC development for domestic power generation. *ECS transactions*. 2009 Sep 25;25(2):689.
- [84] Franco T, Brandner M, Rüttinger M, Kunschert G, Venskutonis A, Sigl L. Recent development aspects of metal supported thin-film SOFC. *ECS Transactions*. 2009 Sep 25;25(2):681.
- [85] Cho HJ, Park YM, Choi GM. Enhanced power density of metal-supported solid oxide fuel cell with a two-step firing process. *Solid State Ionics*. 2011 Jun 16;192(1):519-22.doi: <https://doi.org/10.1016/j.ssi.2010.03.023>.
- [86] Tucker MC, Lau GY, Jacobson CP, DeJonghe LC, Visco SJ. Performance of metal-supported SOFCs with infiltrated electrodes. *Journal of Power Sources*. 2007 Sep 27;171(2):477-82.doi: <https://doi.org/10.1016/j.jpowsour.2007.06.076>.
- [87] Zhou Y, Zhan Z, Wang S. Metal-supported solid oxide fuel cells with impregnated electrodes. *ECS Transactions*. 2013 Oct 6;57(1):877.
- [88] Tucker MC. Development of High Power Density Metal-Supported Solid Oxide Fuel Cells. *Energy Technology*. 2017 Dec;5(12):2175-81.doi: <https://doi.org/10.1002/ente.201700242>
- [89] Fernández-González R, Hernández E, Savvin S, Núñez P, Makradi A, Sabaté N, Esquivel JP, Ruiz-Morales JC. A novel microstructured metal-supported solid oxide fuel cell. *Journal of Power Sources*. 2014 Dec 25;272:233-8.doi: <https://doi.org/10.1016/j.jpowsour.2014.08.081>.
- [90] Zhou Y, Yuan C, Chen T, Meng X, Ye X, Li J, Wang S, Zhan Z. Evaluation of Ni and Ni–Ce_{0.8}Sm_{0.2}O_{2–δ} (SDC) impregnated 430L anodes for metal-supported solid oxide fuel cells. *Journal of Power Sources*. 2014 Dec 1;267:117-22.doi: <https://doi.org/10.1016/j.jpowsour.2014.05.087>
- [91] Rojek-Wöckner VA, Opitz AK, Brandner M, Mathé J, Bram M. A novel Ni/ceria-based anode for metal-supported solid oxide fuel cells. *Journal of Power Sources*. 2016 Oct 1;328:65-74.doi: <https://doi.org/10.1016/j.jpowsour.2016.07.075>.
- [92] Lang M, Szabo P, Ilhan Z, Cinque S, Franco T, Schiller G. Development of solid oxide fuel cells and short stacks for mobile application. 2007 Nov, 4(4): 384-391.doi: <https://doi.org/10.1115/1.2756569>
- [93] Lee K, Kang J, Lee J, Lee S, Bae J. Evaluation of metal-supported solid oxide fuel cells (MS-SOFCs) fabricated at low temperature (~ 1,000° C) using wet chemical coating processes and a

catalyst wet impregnation method. *International Journal of Hydrogen Energy*. 2018 Feb 15;43(7):3786-96.doi: <https://doi.org/10.1016/j.ijhydene.2018.01.027>.

- [94] Nielsen J, Persson ÅH, Sudireddy BR, Irvine JT, Thydén K. Infiltrated La_{0.4}Sr_{0.4}Fe_{0.03}Ni_{0.03}Ti_{0.94}O₃ based anodes for all ceramic and metal supported solid oxide fuel cells. *Journal of Power Sources*. 2017 Dec 31;372:99-106.doi: <https://doi.org/10.1016/j.jpowsour.2017.10.066>.
- [95] Zhou Y, Xin X, Li J, Ye X, Xia C, Wang S, Zhan Z. Performance and degradation of metal-supported solid oxide fuel cells with impregnated electrodes. *international journal of hydrogen energy*. 2014 Feb 4;39(5):2279-85.doi: <https://doi.org/10.1016/j.ijhydene.2013.11.086>.
- [96] Zhou Y, Luo T, Du X, Wang J, Yang W, Sun C, Xia C, Wang S, Zhan Z. High Activity of Nanoporous-Sm_{0.2}Ce_{0.8}O_{2-δ}@ 430L Composites for Hydrogen Electro-Oxidation in Solid Oxide Fuel Cells. *Advanced Energy Materials*. 2014 Dec;4(17):1400883.doi: <https://doi.org/10.1002/aenm.201400883>.
- [97] Zhou Y, Ye X, Li J, Zhan Z, Wang S. Metal-supported solid oxide fuel cells with a simple structure. *Journal of The Electrochemical Society*. 2014 Jan 8;161(3):F332.doi: 10.1149/2.085403jes.
- [98] Zhou Y, Chen T, Li J, Yuan C, Xin X, Chen G, Miao G, Zhan W, Zhan Z, Wang S. Long-term stability of metal-supported solid oxide fuel cells employing infiltrated electrodes. *Journal of Power Sources*. 2015 Nov 1;295:67-73.doi: <https://doi.org/10.1016/j.jpowsour.2015.06.114>.
- [99] Liu X, Han D, Zhou Y, Meng X, Wu H, Li J, Zeng F, Zhan Z. Sc-substituted La_{0.6}Sr_{0.4}FeO_{3-δ} mixed conducting oxides as promising electrodes for symmetrical solid oxide fuel cells. *Journal of Power Sources*. 2014 Jan 15;246:457-63.doi: <https://doi.org/10.1016/j.jpowsour.2013.07.111>.
- [100] Zhou Y, Meng X, Yuan C, Luo T, Ye X, Li J, Wang S, Zhan Z. SrFe_{0.75}Mo_{0.25}O_{3-δ} impregnated 430L alloys for efficient fuel oxidation in metal supported solid oxide fuel cells. *Journal of Power Sources*. 2014 Dec 10;269:244-9.doi: <https://doi.org/10.1016/j.jpowsour.2014.06.092>.
- [101] Zhou Y, Liu X, Li J, Nie H, Ye X, Wang S, Zhan Z. Novel metal-supported solid oxide fuel cells with impregnated symmetric La_{0.6}Sr_{0.4}Fe_{0.9}Sc_{0.1}O_{3-δ} electrodes. *Journal of Power Sources*. 2014 Apr 15;252:164-8.doi: <https://doi.org/10.1016/j.jpowsour.2013.12.020>.
- [102] Sudireddy BR, Nielsen J, Thydén KT, Persson ÅH, Brodersen K. Investigation of Novel Electrocatalysts for Metal Supported Solid Oxide Fuel Cells-Ru: GDC. *ECS Transactions*. 2015 Jun 2;68(1):1417.

- [103] Bischof C, Nenning A, Malleier A, Martetschläger L, Gladbach A, Schafbauer W, Opitz AK, Bram M. Microstructure optimization of nickel/gadolinium-doped ceria anodes as key to significantly increasing power density of metal-supported solid oxide fuel cells. *International Journal of Hydrogen Energy*. 2019 Nov 29;44(59):31475-87.doi: <https://doi.org/10.1016/j.ijhydene.2019.10.010>.
- [104] Thaler F, Udomsilp D, Schafbauer W, Bischof C, Fukuyama Y, Miura Y, Kawabuchi M, Taniguchi S, Takemiya S, Nenning A, Opitz AK. Redox stability of metal-supported fuel cells with nickel/gadolinium-doped ceria anode. *Journal of Power Sources*. 2019 Sep 15;434:226751.doi: <https://doi.org/10.1016/j.jpowsour.2019.226751>.
- [105] Dogdibegovic E, Fukuyama Y, Tucker MC. Ethanol internal reforming in solid oxide fuel cells: A path toward high performance metal-supported cells for vehicular applications. *Journal of Power Sources*. 2020 Feb 15;449:227598.doi: <https://doi.org/10.1016/j.jpowsour.2019.227598>.
- [106] Hong YS, Kim SH, Kim WJ, Yoon HH. Fabrication and characterization GDC electrolyte thin films by e-beam technique for IT-SOFC. *Current Applied Physics*. 2011 Sep 1;11(5):S163-8.doi: <https://doi.org/10.1016/j.cap.2011.03.071>.
- [107] Fei X, Chuanming L, Zhentao W, Zhupeng Y, ZHANG Y, Yanwei Z. Preparation and characterization of SDC nanorods/LNC nanocomposite electrolyte. *Journal of Rare Earths*. 2016 Jul 1;34(7):711-6.doi: [https://doi.org/10.1016/S1002-0721\(16\)60083-2](https://doi.org/10.1016/S1002-0721(16)60083-2).
- [108] Zhou Y, Yuan C, Chen T, Liu M, Li J, Wang S, Zhan Z. Enhanced Performance and Stability of Metal-Supported Solid Oxide Fuel Cells with (Bi₂O₃)_{0.7} (Er₂O₃)_{0.3}-Ag Composite Cathode. *Journal of The Electrochemical Society*. 2014 Nov 1;162(1):F9.doi: 10.1149/2.0131501jes.
- [109] Zhou Y, Meng X, Liu X, Pan X, Li J, Ye X, Nie H, Xia C, Wang S, Zhan Z. Novel architected metal-supported solid oxide fuel cells with Mo-doped SrFeO_{3-δ} electrocatalysts. *Journal of Power Sources*. 2014 Dec 1;267:148-54.doi: <https://doi.org/10.1016/j.jpowsour.2014.04.157>.
- [110] Molin S, Tolczyk M, Gazda M, Jasinski P. Stainless steel/yttria stabilized zirconia composite supported solid oxide fuel cell. *Journal of fuel cell science and technology*. 2011 Oct 1;8(5).doi: <https://doi.org/10.1115/1.4003994>.
- [111] Rüttinger M, Mücke R, Franco T, Büchler O, Menzler NH, Venskutonis A. Metal-supported cells with comparable performance to anode-supported cells in short-term stack environment. *ECS Transactions*. 2011 Apr 25;35(1):259.

- [112] Haydn M, Ortner K, Franco T, Uhlenbruck S, Menzler NH, Stöver D, Bräuer G, Venskutonis A, Sigl LS, Buchkremer HP, Vaßen R. Multi-layer thin-film electrolytes for metal supported solid oxide fuel cells. *Journal of Power Sources*. 2014 Jun 15;256:52-60.doi: <https://doi.org/10.1016/j.jpowsour.2014.01.043>.
- [113] Toor SY, Croiset E. Reducing sintering temperature while maintaining high conductivity for SOFC electrolyte: copper as sintering aid for Samarium Doped Ceria. *Ceramics International*. 2020 Jan 1;46(1):1148-57.
- [114] Kleinlogel C, Gauckler LJ. Sintering and properties of nanosized ceria solid solutions. *Solid State Ionics*. 2000 Nov 1;135(1-4):567-73.doi: [https://doi.org/10.1016/S0167-2738\(00\)00437-9](https://doi.org/10.1016/S0167-2738(00)00437-9).
- [115] Lewis GS, Atkinson A, Steele BC, Drennan J. Effect of Co addition on the lattice parameter, electrical conductivity and sintering of gadolinia-doped ceria. *Solid State Ionics*. 2002 Dec 1;152:567-73.doi: [https://doi.org/10.1016/S0167-2738\(02\)00372-7](https://doi.org/10.1016/S0167-2738(02)00372-7).
- [116] Nicholas JD, De Jonghe LC. Prediction and evaluation of sintering aids for cerium gadolinium oxide. *Solid State Ionics*. 2007 Jul 15;178(19-20):1187-94.doi: <https://doi.org/10.1016/j.ssi.2007.05.019>.
- [117] Huang QA, Oberste-Berghaus J, Yang D, Yick S, Wang Z, Wang B, Hui R. Polarization analysis for metal-supported SOFCs from different fabrication processes. *Journal of power sources*. 2008 Mar 1;177(2):339-47.doi: <https://doi.org/10.1016/j.jpowsour.2007.11.092>.
- [118] Hui SR, Yang D, Wang Z, Yick S, Decès-Petit C, Qu W, Tuck A, Maric R, Ghosh D. Metal-supported solid oxide fuel cell operated at 400–600° C. *Journal of Power Sources*. 2007 May 15;167(2):336-9.doi: <https://doi.org/10.1016/j.jpowsour.2007.02.070>.
- [119] Tucker MC, Kurokawa H, Jacobson CP, De Jonghe LC, Visco SJ. A fundamental study of chromium deposition on solid oxide fuel cell cathode materials. *Journal of Power Sources*. 2006 Sep 29;160(1):130-8.doi: <https://doi.org/10.1016/j.jpowsour.2006.02.017>.
- [120] Hwang C, Tsai CH, Lo CH, Sun CH. Plasma sprayed metal supported YSZ/Ni–LSGM–LSCF ITSOFC with nanostructured anode. *Journal of Power Sources*. 2008 May 15;180(1):132-42.doi: <https://doi.org/10.1016/j.jpowsour.2008.01.075>.
- [121] Hwang CS, Tsai CH, Chang CL, Chuang CM, Shie ZY, Cheng SW, Wu SH. Plasma sprayed metal-supported solid oxide fuel cell and stack with nanostructured anodes and diffusion barrier layer.

Thin solid films. 2014 Nov 3;570:183-8.doi: <https://doi.org/10.1016/j.tsf.2014.02.034>.

- [122] Hwang CS, Hwang TJ, Tsai CH, Chang CL, Yang SF, Wu MH, Fu CY. Effect of plasma spraying power on LSGM electrolyte of metal-supported solid oxide fuel cells. *Ceramics International*. 2017 Aug 1;43:S591-7.doi: <https://doi.org/10.1016/j.ceramint.2017.05.192>.
- [123] Huang QA, Wang B, Qu W, Hui R. Impedance diagnosis of metal-supported SOFCs with SDC as electrolyte. *Journal of Power Sources*. 2009 Jun 15;191(2):297-303.doi: <https://doi.org/10.1016/j.jpowsour.2009.02.004>.
- [124] Klemensø T, Nielsen J, Blennow P, Persson ÅH, Stegk T, Christensen BH, Sønderby S. High performance metal-supported solid oxide fuel cells with Gd-doped ceria barrier layers. *Journal of Power Sources*. 2011 Nov 15;196(22):9459-66.doi: <https://doi.org/10.1016/j.jpowsour.2011.07.014>.
- [125] Stange M, Denonville C, Larring Y, Brevet A, Montani A, Sicardy O, Mougín J, Larsson PO. Improvement of corrosion properties of porous alloy supports for solid oxide fuel cells. *International Journal of Hydrogen Energy*. 2017 Apr 27;42(17):12485-95.doi: <https://doi.org/10.1016/j.ijhydene.2017.03.170>.
- [126] Wang YP, Gao JT, Chen W, Li CX, Zhang SL, Yang GJ, Li CJ. Development of ScSZ Electrolyte by Very Low Pressure Plasma Spraying for High-Performance Metal-Supported SOFCs. *Journal of Thermal Spray Technology*. 2020 Jan 1;29(1-2):223-31.doi: <https://doi.org/10.1007/s11666-019-00970-1>.
- [127] Mitterdorfer A, Gauckler LJ. La₂Zr₂O₇ formation and oxygen reduction kinetics of the La_{0.85}Sr_{0.15}Mn_{0.3}O₃ O₂ (g) | YSZ system. *Solid State Ionics*. 1998 Sep 1;111(3-4):185-218.doi: [https://doi.org/10.1016/S0167-2738\(98\)00195-7](https://doi.org/10.1016/S0167-2738(98)00195-7).
- [128] Huang K, Goodenough JB. *Solid oxide fuel cell technology: principles, performance and operations*. Elsevier; 2009 Jul 30.
- [129] Trebbels R, Markus T, Singheiser L. Reduction of chromium evaporation with manganese-based coatings. *ECS Transactions*. 2009 Sep 25;25(2):1417.
- [130] Oishi N, Yoo Y. Fabrication of cerium oxide based SOFC having a porous stainless steel support. *ECS Transactions*. 2009 Sep 25;25(2):739.
- [131] Orui H, Watanabe K, Chiba R, Arakawa M. Application of LaNi (Fe) O₃ as SOFC cathode. *Journal*

of The Electrochemical Society. 2004 Aug 11;151(9):A1412.doi: 10.1149/1.1779628.

- [132] Blennow P, Hjelm J, Klemensø T, Ramousse S, Kromp A, Leonide A, Weber A. Manufacturing and characterization of metal-supported solid oxide fuel cells. *Journal of Power Sources*. 2011 Sep 1;196(17):7117-25.doi: <https://doi.org/10.1016/j.jpowsour.2010.08.088>.
- [133] Klemensø T, Nielsen J, Blennow P, Persson A, Stegk T, Hjalmarsson P, Christensen B, Sønderby S, Hjelm J, Ramousse S. Development of long-term stable and high-performing metal-supported SOFCs. *ECS Transactions*. 2011 Apr 25;35(1):369.
- [134] Irvine JT, Bae J, Park JY, Choi WS, Kim JH. Electrochemical properties and durability of in-situ composite cathodes with SmBa_{0.5}Sr_{0.5}Co₂O_{5+δ} for metal supported solid oxide fuel cells. *International Journal of Hydrogen Energy*. 2017 Jan 12;42(2):1212-20.doi: <https://doi.org/10.1016/j.ijhydene.2016.10.158>.
- [135] Baek SW, Jeong J, Kim JH, Lee C, Bae J. Interconnect-integrated solid oxide fuel cell with high temperature sinter-joining process. *International journal of hydrogen energy*. 2010 Nov 1;35(21):11878-89.doi: <https://doi.org/10.1016/j.ijhydene.2010.07.108>.
- [136] Baek SW, Jeong J, Kim YM, Kim JH, Shin S, Bae J. Metal-supported solid oxide fuel cells with barium-containing in-situ cathodes. *Solid State Ionics*. 2011 Jun 16;192(1):387-93.doi: <https://doi.org/10.1016/j.ssi.2010.09.047>.
- [137] Lee C, Bae J. Fabrication and characterization of metal-supported solid oxide fuel cells. *Journal of Power Sources*. 2008 Jan 21;176(1):62-9.doi: <https://doi.org/10.1016/j.jpowsour.2007.10.067>.
- [138] Lee C, Bae J, Kim JH, Baek SW. La_{0.8}Sr_{0.2}Co_{1-x}Mn_xO₃ Cathode and Its Application to Metal-Supported Solid Oxide Fuel Cells. *Journal of Fuel Cell Science and Technology*. 2010 Apr 1;7(2).doi: <https://doi.org/10.1115/1.3182738>.
- [139] Baek SW, Jeong J, Lee S, Bae J. Electrochemical property of Cr-containing cathode materials for metal-supported solid oxide fuel cell. *ECS Transactions*. 2009 Sep 25;25(2):2909.
- [140] Udomsilp D, Roehrens D, Menzler NH, Bischof C, de Haart LG, Opitz AK, Guillon O, Bram M. High-performance metal-supported solid oxide fuel cells by advanced cathode processing. *Journal of The Electrochemical Society*. 2017 Oct 5;164(13):F1375.doi:10.1149/2.0571713jes.
- [141] Bram M, Udomsilp D, Roehrens D, Menzler NH, Opitz AK, de Haart LG, Guillon O. High Performance (La, Sr)(Co, Fe) O₃ Cathodes with Improved Adherence for Metal-Supported Fuel

Cells. ECS transactions. 2017 May 30;78(1):709.

- [142] Udomsilp D, Roehrens D, Menzler NH, Opitz AK, Guillon O, Bram M. Novel processing of La_{0.58}Sr_{0.4}Co_{0.2}Fe_{0.8}O_{3-δ} cathodes for metal-supported fuel cells. *Materials Letters*. 2017 Apr 1;192:173-6.doi: <https://doi.org/10.1016/j.matlet.2016.12.027>.
- [143] Udomsilp D, Thaler F, Menzler NH, Bischof C, de Haart LG, Opitz AK, Guillon O, Bram M. Dual-Phase Cathodes for Metal-Supported Solid Oxide Fuel Cells: Processing, Performance, Durability. *Journal of The Electrochemical Society*. 2019 Apr 30;166(8):F506.doi: 10.1149/2.0561908jes.
- [144] Sholklafter TZ, Lu C, Jacobson CP, Visco SJ, De Jonghe LC. LSM-infiltrated solid oxide fuel cell cathodes. *Electrochemical and Solid State Letters*. 2006 May 24;9(8):A376.
- [145] Zhan W, Zhou Y, Chen T, Miao G, Ye X, Li J, Zhan Z, Wang S, Deng Z. Long-term stability of infiltrated La_{0.8}Sr_{0.2}CoO_{3-δ}, La_{0.58}Sr_{0.4}Co_{0.2}Fe_{0.8}O_{3-δ} and SmBa_{0.5}Sr_{0.5}Co₂O_{5+δ} cathodes for low temperature solid oxide fuel cells. *International Journal of Hydrogen Energy*. 2015 Dec 14;40(46):16532-9.doi: <https://doi.org/10.1016/j.ijhydene.2015.08.073>.
- [146] Fukunaga H, Koyama M, Takahashi N, Wen C, Yamada K. Reaction model of dense Sm_{0.5}Sr_{0.5}CoO₃ as SOFC cathode. *Solid State Ionics*. 2000 Jul 2;132(3-4):279-85.doi: [https://doi.org/10.1016/S0167-2738\(00\)00642-1](https://doi.org/10.1016/S0167-2738(00)00642-1).
- [147] Ullmann H, Trofimenko N, Tietz F, Stöver D, Ahmad-Khanlou A. Correlation between thermal expansion and oxide ion transport in mixed conducting perovskite-type oxides for SOFC cathodes. *Solid state ionics*. 2000 Dec 1;138(1-2):79-90.doi: [https://doi.org/10.1016/S0167-2738\(00\)00770-0](https://doi.org/10.1016/S0167-2738(00)00770-0).
- [148] Zhou Y, Han D, Yuan C, Liu M, Chen T, Wang S, Zhan Z. Infiltrated SmBa_{0.5}Sr_{0.5}Co₂O_{5+δ} cathodes for metal-supported solid oxide fuel cells. *Electrochimica Acta*. 2014 Dec 10;149:231-6.doi: <https://doi.org/10.1016/j.electacta.2014.10.067>.
- [149] Zhou Y, Meng X, Ye X, Li J, Wang S, Zhan Z. Metal-supported solid oxide fuel cells with impregnated SrFe_{0.75}Mo_{0.25}O₃ cathodes. *Journal of Power Sources*. 2014 Feb 1;247:556-61.doi: <https://doi.org/10.1016/j.jpowsour.2013.08.134>.
- [150] Han D, Wu H, Li J, Wang S, Zhan Z. Nanostructuring of SmBa_{0.5}Sr_{0.5}Co₂O_{5+δ} cathodes for reduced-temperature solid oxide fuel cells. *Journal of Power Sources*. 2014 Jan 15;246:409-16.doi: <https://doi.org/10.1016/j.jpowsour.2013.07.113>.

- [151] Dogdibegovic E, Wang R, Lau GY, Tucker MC. High performance metal-supported solid oxide fuel cells with infiltrated electrodes. *Journal of Power Sources*. 2019 Jan 15;410:91-8.doi: <https://doi.org/10.1016/j.jpowsour.2018.11.004>.
- [152] Dogdibegovic E, Wang R, Lau GY, Karimaghaloo A, Lee MH, Tucker MC. Progress in durability of metal-supported solid oxide fuel cells with infiltrated electrodes. *Journal of Power sources*. 2019 Oct 15;437:226935.doi: <https://doi.org/10.1016/j.jpowsour.2019.226935>.
- [153] Tucker MC. Personal power using metal-supported solid oxide fuel cells operated in a camping stove flame. *International Journal of Hydrogen Energy*. 2018 May 3;43(18):8991-8.doi: <https://doi.org/10.1016/j.ijhydene.2018.03.161>.
- [154] Yamaguchi Y, Sumi H, Takahashi H, Mori R, Shimizu H. Development of Metal-Supported Planar SOFCs Fabricated by All Wet Process on Metallurgical Porous Substrates. *ECS Transactions*. 2019 Jul 10;91(1):909.
- [155] Ideris A. Carbon Formation Inhibition in Solid Oxide Fuel Cells (SOFCs) Using H₂S. 2014.
- [156] Minic D, editor. *Hydrogen Energy: Challenges and Perspectives*. BoD–Books on Demand; 2012 Oct 17.

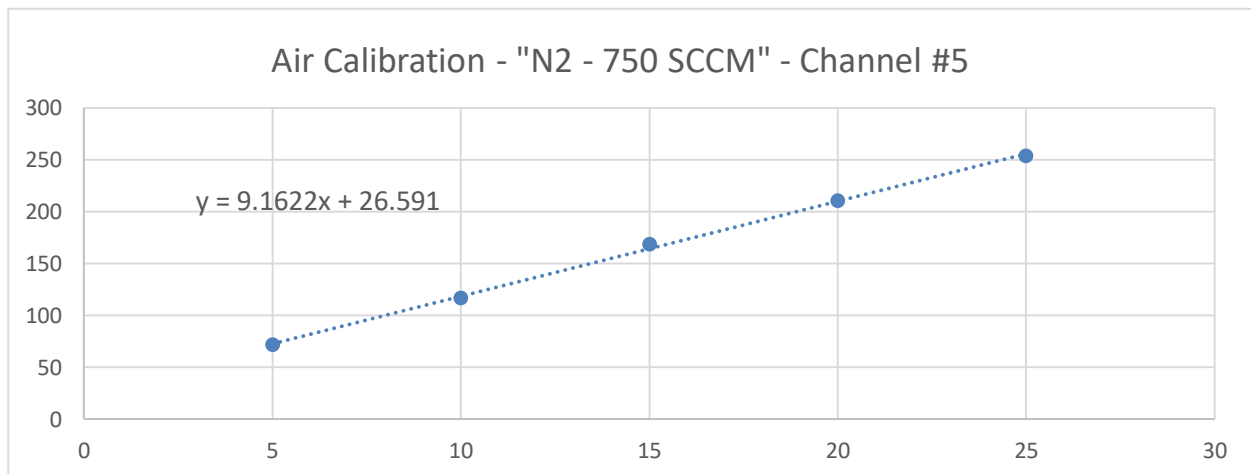
APPENDIX

Air, Argon and Hydrogen Calibration used in this study

1. Air calibration

% full scale	volume (mL)	time (s)	Flowrate (SCCM)	Column1
5	15	12.64	71	
5	15	12.56	72	
5	15	12.59	71	71
10	15	7.75	116	
10	15	7.77	116	
10	15	7.69	117	116
15	15	5.2	173	
15	15	5.35	168	
15	15	5.47	165	169
20	10	2.87	209	
20	10	2.91	206	
20	10	2.79	215	
20	10	2.86	210	
20	10	2.85	211	210
25	10	2.35	255	
25	10	2.35	255	
25	10	2.36	254	
25	10	2.4	250	
25	10	2.37	253	254

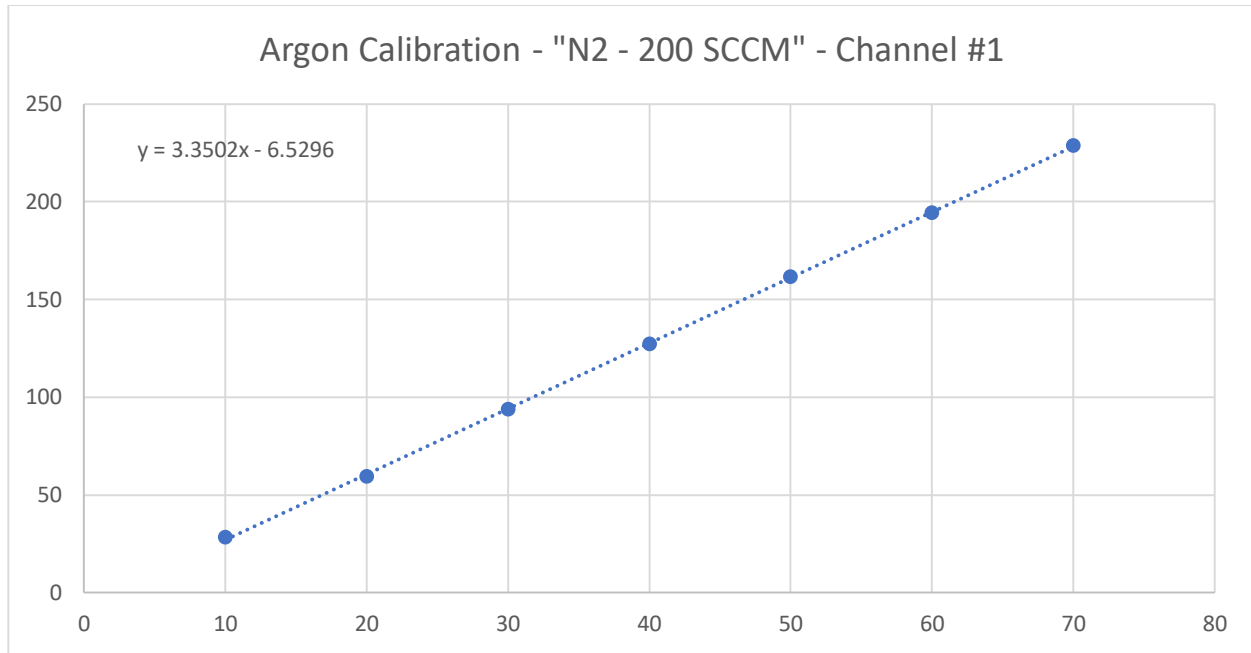
Chart % full scale - flow rate	Column1
flowrate (SCCM)	% full scale
50	3
100	8
150	13
200	19
250	24
300	30
350	35
400	41
500	52
600	63



2. Argon calibration

% full scale	volume (mL)	time (s)	Flowrate (SCCM)	Column1
10	15	32.25	28	
10	15	32.63	28	
10	15	31.06	29	28
20	15	15.85	57	
20	15	14.89	60	
20	15	14.77	61	59
30	15	9.67	93	
30	15	9.55	94	
30	15	9.58	94	94
40	15	7.02	128	
40	15	7.08	127	
40	15	7.16	126	127
50	15	5.57	162	
50	15	5.58	161	
50	15	5.57	162	161
60	15	4.65	194	
60	15	4.63	194	
60	15	4.63	194	194
70	10	2.62	229	
70	10	2.6	231	
70	10	2.66	226	228

Chart % full scale - flow rate flowrate (SCCM)	Column1 % full scale
10	5
20	8
30	11
40	14
50	17
60	20
70	23
80	26
90	29
100	32
110	35
120	38
130	41
140	44
150	47
160	50
170	53
180	56
190	59
200	62
210	65
220	68
230	71
240	74
250	77



3. Hydrogen calibration

% full scale	volume (mL)	time (s)	Flowrate (SCCM)	Column1
20	15	23.01	39	
20	15	22.77	40	
20	15	22.76	40	39
30	15	15.93	56	
30	15	16.19	56	
30	15	16.21	56	56
40	15	12.72	71	
40	15	12.61	71	
40	15	12.52	72	71
50	15	10.37	87	
50	15	10.42	86	
50	15	10.3	87	87
60	15	8.78	103	
60	15	8.85	102	
60	15	8.77	103	102
70	15	7.65	118	
70	15	7.7	117	
70	15	7.65	118	117
80	15	6.84	132	
80	15	6.9	130	

Chart % full scale - flow rate	Column1
flowrate (SCCM)	% full scale
20	6
30	12
40	19
50	26
60	33
70	39
80	46
90	53
100	60
110	66
120	73
130	80
140	86
150	93
160	100

80	15	6.9	130	131
90	15	6.22	145	
90	15	6.28	143	
90	15	6.27	144	144
99.7	15	5.72	157	
99.7	15	5.65	159	
99.7	15	5.71	158	158

